ANALYSIS OF FATIGUE BEHAVIOR, FATIGUE DAMAGE AND FATIGUE FRACTURE SURFACES OF TWO HIGH STRENGTH STEELS

A Thesis Presented to the Academic Faculty

By

Charles G. Lester IV

In Partial Fulfillment of the Requirements for the Degree of Master of Science in the School Materials Science and Engineering

Georgia Institute of Technology

December 2011

ANALYSIS OF FATIGUE BEHAVIOR, FATIGUE DAMAGE AND FATIGUE FRACTURE SURFACES OF TWO HIGH STRENGTH STEELS

Dr. Arun M. Gokhale
School of Materials Science and Engineering
Georgia Institute of Technology

Dr. Preet Singh
School of Materials Science and Engineering
Georgia Institute of Technology

Dr. Shrikant P. Bhat
Principal Research Engineer
Automotive Product Applications
ArcelorMittal Global R&D – East Chicago

Date Approved: 9/15/2011

Engineering is a great profession. There is the satisfaction of watching a figment of the imagination emerge through the aid of science to a plan on paper. Then it moves to realization in stone or metal or energy. Then it brings homes to men or women. Then it elevates the standard of living and adds to the comforts of life. This is the engineer's high privilege. - Herbert Hoover

Acknowledgements

Completion of this thesis proved to be a difficult endeavor, however the journey was made more meaningful by key people that provided support throughout my study. Dr. Arun Gokhale acted as my thesis advisor and provided me with key resources necessary for completion. Without the aid of Dr. Gokhale this thesis may have never existed. Dr. Shrikant Bhat also provided advisement on my thesis on behalf of ArcelorMittal Global R&D. The input I received from Dr. Bhat encouraged me to critically analyze the problems that I encountered during my research and focus my thesis, thereby improving the overall quality of the document. Both Dr. Gokhale and Dr. Bhat have an incredibly thorough understanding of metallurgy and I am privileged to be in the company of such esteemed and knowledgeable metallurgists. To each of them I am in a debt of gratitude and will always recognize that they provided me with the opportunity to prove myself as an engineer. Although, the realization is that I still have much to learn.

Additional thanks goes to Dr. Preet Singh, Mr. Rick Brown and Dr. Gautam Patel. Dr. Singh was part of the thesis committee and provided me with valuable feedback, which helped me gain a more thorough understanding of the research. Mr. Brown spent many hours working with me at the Georgia Tech Materials Properties Research Laboratory to make certain that the experiments were running smoothly and maintained the highest possible level of accuracy. Dr. Patel works at Georgia Tech Research Institute and helped with many of the high-quality images that are included in this thesis.

A deep acknowledgment goes to my parents, Charles and Christine Lester, who have made many sacrifices for me over the years and continue to make certain that I have the resources I need to be successful. Many of the sacrifices went un-recognized for a long time and now I better understand how those sacrifices contributed to the

completion of this thesis. Their parenting has developed the attitude, which has allowed me to overcome many of the obstacles that I have faced. Without their guidance, I certainly would not have come this far.

Perhaps the one person most responsible for allowing me to go back to school and pursue a thesis is my wife, Chelsey. At any point she could have asked me to stop pursuing my educational goals. This would have allowed both of us to live much more comfortably over the last couple of years. Instead she has encouraged me to continue and explore the limitations of what I am capable of both personally and professionally. Being married to such an outstanding individual who cares so deeply about me has truly made the experience meaningful, despite the difficulties that I have encountered. All I can say is, “Chels you’re something else”

Lastly the generous financial support of ArcelorMittal and Georgia Tech is acknowledged. This project would not of been possible without both ArcelorMittal and Georgia Tech investing their time, money and trust in me.

Table of Contents

Page

List of Tables

List of Figures

Summary

Building fuel efficient automobiles is increasingly important due to the rising cost of energy. One way to improve fuel efficiency is to reduce the overall automobile weight. Weight reductions using steel components are desirable because of easy integration into existing manufacturing systems. Designing components with Advanced High Strength Steels (AHSS) has allowed for material reductions, while maintaining strength requirements. Two Advanced High Strength steel microstructures investigated in this research utilize different strengthening mechanisms to obtain a desired tensile strength grade of 590MPa. One steel, HR590, utilizes precipitation strengthening to refine the grain size and harden the steel. The other steel, HR590DP, utilizes a dual phase microstructure consisting of hardened martensite constituents in a ferrite matrix. The steels are processed to have the same tensile strength grade, but exhibit different fatigue behavior. The central objective of this research is to characterize and compare the fatigue behavior of these two steels. The results show the dual phase steel work hardens at a low fatigue life. The precipitation strengthened microstructure shows hardening at low strain amplitudes, softening at intermediate strain amplitudes and little to no effect at high strain amplitudes. These different fatigue responses are characterized and quantified in this research. Additionally, observations showing the fracture surfaces and the bulk microstructure are analyzed.

Chapter 1: Rationale, Objectives and Research Tasks

1.1 Rationale

Steel continues to be the most extensively used and arguably the most important material used in automobiles. Steel is the material chosen in most automotive applications due to the ease of manufacturing and the favorable mechanical properties inherent in the material. Consequently, in order to decrease the energy consumption it has become essential to make automotive steel components lighter. Advanced High-Strength Steels (AHSS) are being researched and developed for use in lighter components to increase fuel efficiency[1] because they facilitate substantial weight reduction, while maintaining the strength and integrity of the parts. The improved properties of AHSS allow efficient and cost-effective fabrication of complex shaped components that have become a mainstay of modern automobiles. Automotive wheels[2] are a structural component where excellent formability, strength and fatigue properties are important. As a result, AHSS are the materials of choice for the majority of automotive wheels due to low cost, ease of manufacturing and favorable monotonic/cyclic mechanical properties compared to non-ferrous materials. Utilizing different processing routes that involve heat treatments, mechanical treatments and alloying, parts having the required strength can be designed and fabricated using numerous AHSS steels, which can facilitate weight reduction. However, such steels having comparable strengths do not necessarily have a similar fatigue response. For example, Bhat[3] has shown that the fatigue properties of High-Strength Low-Alloy steels (HSLA) vary within a grade. Therefore, it is of interest to quantify and understand differences in the fatigue behavior and fatigue mechanisms of AHSS steels having different microstructures (resulting from different processing routes) and chemical compositions, but comparable strength levels. In this context, it is important to point out

the mechanisms by which fatigue occurs in AHSS. Consequently, better understanding of the fatigue mechanism can lead to a further reduction in component weight, thereby increasing the fuel efficiency of modern automobiles.

High strength low alloy (HSLA) steels and dual phase (DP) steels are two important types of modern AHSS steels that are attractive for structural automotive applications, such as automotive wheels. Although many varieties of HSLA steels exist, ductile ferrite is the major microstructural phase in all HSLA steels, which is desirable because of good formability and weldability. Microalloying is common in AHSS to achieve the required strength levels with a minimum loss of ductility. Commonly used microalloying elements are Vanadium (V), Titanium (Ti) and Niobium (Nb).[4] The development of processing techniques, such as ladle injection, has allowed precise addition of alloying elements in very small quantities to achieve the target alloy chemistry.[4] Dual Phase is another type of high-strength steel, which possesses microstructural elements of both a hard martensite microstructure and more ductile ferrite microstructure. This microstructure derives its strength from secondary martensite/bainite phases, which are high in strength. The dual phase microstructure is intended to provide mechanical properties such that formability can be maintained while increasing strength. Both HSLA and DP steels provide good ratio of ductility-to-strength with only a small quantity of carbon and other alloying elements, therefore both of these steels are attractive for automotive structural applications, such as automotive wheels, where fatigue life is of substantial importance. It is possible to commercially produce both HSLA and DP micro-alloyed steels having the same strength level (grade). Therefore, it is of interest to quantitatively characterize the differences in the fatigue behavior and fatigue mechanisms of DP and HSLA micro-alloyed of the same grade (strength). Consequently, the focus of this research is a comparative study of the fatigue behavior of a commercial micro-alloyed HSLA steel, HR590, and a commercial DP steel,

HR590DP, that are of 590 MPa strength grade (i.e. minimum ultimate tensile strength is 590 MPa). In these steel designations, HR implies that these steels are hot-rolled. The following section describes the central objectives and major tasks of this research.

1.2 Objectives and Research Tasks

The central objective of this research is to quantitatively characterize and understand the differences in fatigue behavior of two types of AHSS (namely HR590 and HR590DP) of the same grade (590 MPa) and correlate the differences in fatigue behavior with the differences in microstructure and chemistry. The steel microstructure is dependent on the processing parameters and techniques, therefore fatigue data will ultimately help in improving the processing of these high-strength steels. The research involves the following major research tasks:

1. Strain-controlled fatigue tests on a series of specimens of HR590 and HR590DP. The number of cycles to failure is determined for a series of strain amplitudes and their corresponding stress amplitudes. The strain amplitudes used for this investigation are 0.2%, 0.25%, 0.30%, 0.35%, 0.5%, 0.8%, 1.1%, 1.4%, 1.7% and 2.0% with expected life levels from a few hundreds to a half-million cycles.
2. A detailed analysis of the experimental data obtained from the fatigue tests. This involves characterization of the stress-strain response, the strain-life response, and the cyclic stress for strain resistance of the steel under cyclic loading conditions. This analysis will lead to quantitative information on how the material is changing within a constant strain regime. Material changes may include softening or hardening and the rate of such changes.
3. Characterization of the microstructure of each type of steel, by using optical and SEM (Scanning Electron Microscope) metallography. This will provide important

baseline information on the morphology and what possible characteristics may induce fatigue crack initiation.

4. Characterization of cyclically loaded specimens using SEM fractography. Information of interest is the tortuosity of the fracture surfaces, crack initiation and crack propagation leading to failure.
5. Compare the microstructural characteristics and morphology of HR590 and HR590DP. This will provide information on what variations in the microstructure have an influence on fatigue life.

The results of this research will provide information for selection of AHSS in areas that require a combination of high strength and good fatigue life thus enabling potential reductions in gauge thickness and consequent reduction in the weight of the steel components. Furthermore, the results give insight to the attributes of the microstructure that will provide the best combination of properties for use in future applications.

Chapter 2: Background and Literature Review

Variations in chemical composition and processing produce steel microstructures exhibiting different mechanical behavior during cyclic loading. Quantifying and characterizing the microstructure-fatigue relationships is important in identifying the mechanisms leading to fatigue failure. It is the objective of this chapter to examine the fatigue response and the microstructure fatigue relationships by evaluating past and current research in the field. This chapter covers the effects of variations in chemistry, processing and strengthening mechanisms on the fatigue behavior of the two steels of interest. Variations in alloying and processing affect microstructural properties such as grain size, size distributions, precipitates and phase distributions present in the final microstructure. These microstructural attributes affect the changes that occur as a function of fatigue cycling. Application of cyclic loading is expected to change the flow properties such as hardness, elasticity and strength. Therefore, to characterize the fatigue response, it is important to recognize the changes in flow properties and the rates at which those properties are changing. Consequently, this chapter also presents fatigue research relevant to low-carbon steels; covering stress-strain, stress-life and strain-life relationships.

2.1 Chemistry of HSLA and DP Steels

Alteration of the chemical composition by alloying additions such as C, V, Ti, Nb, Mn and Cr affects the mechanical properties of the steel, and consequently, the fatigue response. Addition of alloying elements changes the mechanical properties by solid solution hardening, precipitation hardening and/or grain-refinement. The strengthening mechanism that is most prevalent is often determined by the solubility of the alloying elements. Since steel is allotropic, further consideration needs to be given to the

microstructural constituents and their effects on solubility. The austenite phase has higher solubility of carbon and some other alloying elements than ferrite and therefore is more likely to form a solid solution. The solubility decreases as the austenite transforms to ferrite leading to the formation of a multi-phase microstructure. Therefore the specific changes to fatigue life with the addition of alloying elements will be examined. The microstructural transformations in turn affect material properties and fatigue response. It is important to point out that it is possible to produce different microstructures (having different compositions) that have the same strength level, but not necessarily the same fatigue response. Therefore, effects of chemical composition and microstructure are examined in the following sub-sections.

Carbon

Commercial HSLA and DP steels are low carbon steels: these steels typically contain less than 0.2wt% C. Carbon has extremely low solubility in ferrite, therefore C is rejected from the grains promoting formation of pearlite and carbides in HSLA steels. Increasing the carbon content of the hot-rolled micro-alloyed HSLA steel affects the strength and ductility of the steel. In the DP steels, the carbon is mostly present in the martensite/bainite constituents. Since the strength of DP steel is dependent on martensite/bainite volume fraction and its carbon content, an increase in the overall carbon content of DP steel leads to an increase in monotonic strength, but not necessarily cyclic or fatigue strength. Therefore, carbon affects the strength of HSLA and DP steels through its distinctly different effects on microstructure. However, due to different microstructures HSLA and DP steels may not necessarily have the same fatigue response.

Micro-alloying Elements: Vanadium, Titanium, Niobum

Micro-alloyed steels (such as hot-rolled HSLA steels) contain precisely controlled small quantities of strong carbide/nitride forming elements such as V, Ti and Nb in the amounts ranging from 0.01 to 0.1wt%. These elements form carbides/nitrides that are stable at high temperatures. At temperatures where the steel is austenitic, these carbides/nitrides are present on the austenite grain boundaries as well as in the grain interiors. The grain boundary carbides/nitrides retard the grain growth of austenite at high temperatures during processing, so that the finer austenite grain size leads to a finer ferrite grain size in the final hot-rolled microstructure. The finer ferrite grain size in turn leads to an increase in the strength of the hot-rolled HSLA steels via the Hall-Petch effect. Further, as carbides of micro-alloying elements are fine in size (typically, less than 0.1µm), they also increase the strength of the steel via dispersion hardening and precipitation hardening mechanisms.

In HSLA steels, the micro-alloying additions are seldom used individually; typically, several micro-alloying elements are added in different quantities. This is due to different solubility of the micro-alloying elements in austenite (see Figure 1). For example, titanium nitride is stable up to temperatures in excess of 1200°C, whereas vanadium carbide dissolves in austenite at a substantially lower temperature. Therefore, during the thermo-mechanical processing of micro-alloyed steel, different types of carbides/nitrides precipitate over different temperature regimes, which is useful for retarding austenite grain size as it undergoes recrystallisation and growth.

It is important to point out that the micro-alloying elements are not added in large quantities (<0.1wt%) because 1) they are expensive, 2) it can lead to formation of a continuous network of carbides and/or 3) coarser carbide particle size, which

deleteriously affect the mechanical properties of steel. The mechanical properties of HSLA steels with small additions of individual micro-alloying elements was examined by Sherman[5] showing better fatigue life compared to a similar steel without micro-alloying elements.

In comparison with micro-alloyed HSLA steels, the DP steels have negligible amounts of micro-alloying additions. Therefore, DP steels are not designated micro-alloyed steels. The absence of micro-alloying additions in the DP steels is dictated by the fact that DP steels derive their strength primarily from the presence of martensite/bainite constituents rather than dispersion/precipitation hardening effects. This important difference in the microstructure and chemistry of the micro-alloyed HSLA steels and DP steels affects the fatigue behavior of the two steels of interest.

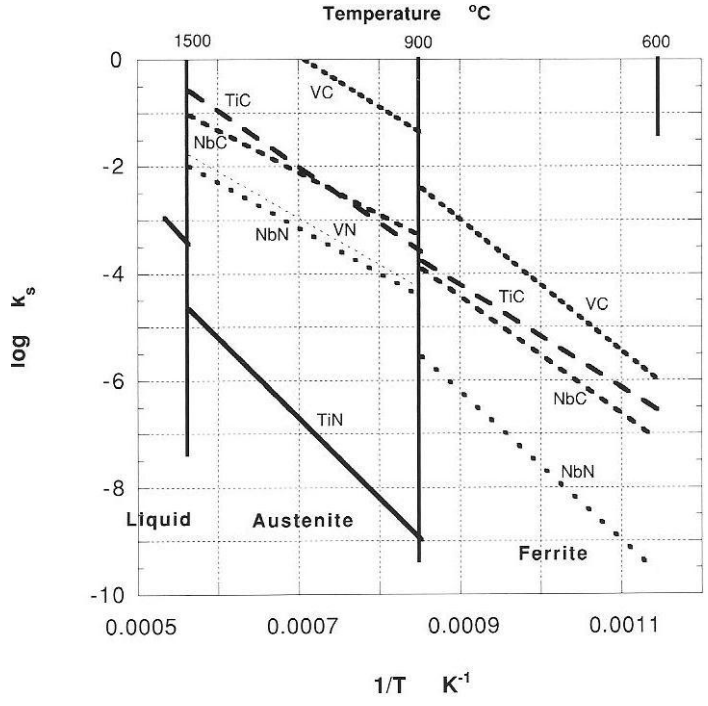

Figure 1: Solubility product as a function of temperature for various carbides and nitrides important to micro-alloyed steels[6]

Chromium

Cr is added to DP steel to enhance its hardenability.[7] Higher hardenability is required in the DP steel, (but not in the hot-rolled HSLA steels) as martensite/bainite constituents must form (rather than pearlite) when the DP steel is cooled after the inter-critical temperature treatment. The hardenability increase due to Cr is particularly important in low carbon steels (such as DP steels) because the lower carbon content reduces the hardenability substantially. On the other hand, the micro-alloyed HSLA steels contain substantially lower amounts of Cr because high hardenability is not necessary in these steels. Additionally, Cr is a strong carbide former and forms chromium carbide precipitates when present in the amount beyond its solubility limit. The chromium carbide precipitates retard grain growth (when present on the grain boundaries) and impede the dislocation motion and thereby they can influence the response of the steel to monotonic and cyclic stresses. Therefore, Cr content is another important difference in the composition of the micro-alloyed HSLA and DP steels that can influence fatigue behavior.

Manganese

Most commercial steels contain at least 0.5% Mn, to eliminate hot-shortness and increase the hardenability of steel. Therefore, Mn plays a key role in the formation of martensite/bainite constituents in the DP steels after the inter-critical temperature treatment. A higher amount (~1.5%) of Mn is added to DP steels to compensate for the loss in hardenability from having lower carbon content . Nonetheless, higher amounts of Mn also lead to segregation resulting in the formation of Mn-rich and Mn-poor bands in the microstructure.[8] In general, such microstructural spatial non-uniformities are not desirable as they are deleterious to the mechanical properties of steels.

2.2 Processing of HSLA and DP Steels

2.2.1 Casting and Solidification

The process of casting involves the solidification of liquid and is critical is critical to the evolution of the final microstructure. Prior to solidification, alloying elements are uniformly distributed in the liquid steel. Alloying is commonly done through ladle injection, allowing small and precise quantities to be added to the liquid steel. The final shape of the cast steel can be in the form of ingots or continuously cast in billets. To meet productivity demands the continuously cast method is commonly employed in commercial manufacturing.

The cross-section of an ingot or billet can be divided into three zones: 1) a fine chill zone of equiaxed crystals near the mold wall, 2) a columnar zone resulting from the growth of dendrites way from the chill zone and 3) a central equiaxed zone with coarse crystals. The smaller the columnar growth zone the better the mechanical properties of the cast material. During dendritic growth in a peritectic reaction (such as steel solidification), solute is rejected to the interdendritic channels creating segregated solute-rich regions. Manganese is an example of a solute that tends to segregate into interdendritic regions, leading to the formation of bands.[8] The extent of this segregation is controlled by the interdendritic arm spacing and cast grain size. Interdendritic arm spacing is a function of cooling rate,[8][9][10] therefore cooling rate dictates the size and spacing of the bands. The smallest possible interdendritic arm spacing is the most desirable for enhancing mechanical properties. Since manganese is an austenite stabilizer, Mn bands are the last to undergo transformation of the austenite. In ferrite/pearlite steels, banding will lead to alternating layers of ferrite and pearlite.[9] In dual phase steels banding leads to alternating layer of ferrite and martensite/bainite constituents.[7] This type of segregation is known as microsegregration and can be

mitigated by thermo-mechanical treatment during final processing. If the effects of banding resulting from microsegregation are not fully reversed, the steel shows anisostropic mechanical properties. Therefore in such a case, fatigue behavior depends on the direction of loading.[11]

In contrast, if the segregation is happening over a much larger scale it is referred to as macrosegregation. Due to the scale, macrosegregation usually cannot be mitigated by subsequent thermo mechanical processing. Macrosegregation can be due to numerous reasons including:[12]

1) Shrinkage due to solidification and thermal contraction
2) Density differences in the inter-dendritic liquid
3) Density differences between the solid and liquid
4) Convection currents driven by temperature-induced density differences in the liquid

Combinations of the micro and macrosegregation may generate complex patterns in the cast ingot or billet. Generally, shrinkage effects are seen near the mold wall as solute move deeper into the inter-dendritic channels. On the other hand, density differences cause the heavier material to move in the direction of gravity. In the case of continuously cast billets, macrosegregation due to density differences is seen in the center of the billet. Center-segregation forms as a result of initial casting in the vertical position, as shown in Figure 2. As the continuous casting process proceeds, solid first forms at the mold wall and rejects solute into the liquid. The solute-rich liquid moves down and towards the center of the billet, which is last to solidify. Macrosegregation during the initial casting stage is present throughout the processing route, as the steel is unlikely to homogenize during subsequent treatments. Compositional changes resulting from

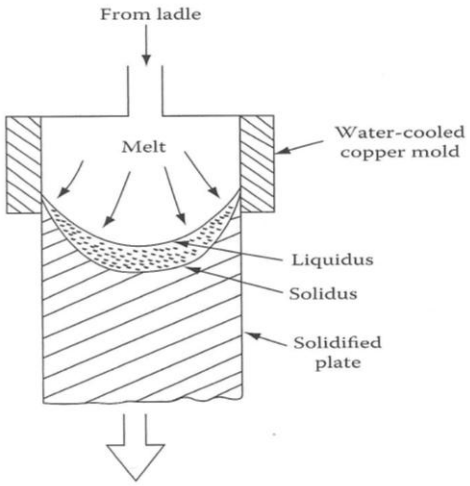

Figure 2: Solidification cross-section of a continuously cast mold, showing the profiles of liquid, liquid+solid and solid regions[12]

macrosegregation are detrimental to the fatigue behavior of steel, but may be unavoidable during processing.

2.2.2 Thermo-mechanical Processing

The steels of interest (HR590 and HR590DP) were prepared using a hot-rolling process. These steels are allotropic and as such the properties are able to be significantly altered by the application of thermo-mechanical treatments during hot-rolling. The temperature and duration of treatments changes the microstructure and alters the fatigue behavior. For example, the initial annealing treatment is critical in refining the grain size.[13] Initial annealing is necessary for mechanical rolling in the austenite phase. The mechanical rolling elongates the austenite grains, providing more surface area for nucleation of ferrite and assisting in the nucleation of grain-refining precipitates. The finishing process is intended to homogenize the steel and refine the microstructure. The hot-rolling parameters depend on the steel's chemical composition and the desired final microstructure.

Fatigue behavior can exhibit anisotropy, based on the rolling direction and heat treatments.[11] This can be used as a crack-arrest mechanism if the loading direction is parallel to this weaker plane; however, fatigue-life may be drastically reduced in a different loading direction. This results from fatigue cracks originating at inhomogeneities caused by hot-rolling. Furthermore, the fatigue life of high-strength steels is more dependent on crack initiation rather than crack propagation. Dual phase steels have different phases that do not deform equally with applied stress. The interface between phases can be crack initiation site. Additionally the textured surface caused by rolling can be a source of crack initiation. [14] Therefore, fatigue life is a function of many variables that can result from thermo-mechanical treatment.

Cooling after rolling is often done quickly to promote high nucleation and low growth rates. Development of cooling media delivery methods, notably a process called compact cooling,[15] can increase the cooling rate. Compact cooling increases the rate of heat transfer by using a high flow rate manifold combined with shorter distances from nozzle to material in lieu of the more conventional laminar flow system. Sarwar et. al.[16] studied the effect of martensite content on fatigue life by using different quenching mediums to cool dual phase specimens from the two-phase field. Mediums linked with faster cooling rates promoted higher martensite contents and lead to longer fatigue lives. However, if temperature gradients from rapid cooling results in microstructural non-homogeneities lower fatigue life is expected.

2.3 Microstructure and Strengthening of HSLA and DP Steels

HSLA and DP steels have complex microstructures consisting of many constituents. Refinement of the steel microstructure has resulted in stronger steels with lower carbon content. Traditional high-strength non-AHSS derive strength from high carbon concentrations. The strength increase is a result of solid solution hardening;

however the high carbon content also results in poor weldability, toughness and formability. Low-carbon AHSS achieve strengths that are comparable to traditional high-strength non-AHSS via utilizing a combination of strengthening mechanisms. In the case of the two steels of interest, the HR590 steel uses precipitation hardening and grain-refinement as strengthening mechanisms. The HR590DP steel strengthens the ferrite matrix by formation of secondary martensite/bainite phases, as well as grain-refinement.

2.3.1 Microstructural Attributes of HSLA and DP Steels

Ferrite is the primary microstructural phase in both HSLA and DP steels. Ferrite is identified by one of two morphologies in micro-alloyed steels 1) polygonal and 2) acicular. [4] The polygonal microstructure consists of equiaxed grains, where the acicular forms a lath-like morphology similar to that of bainite. Acicular ferrite is formed through a diffusion controlled shear transformation. This transformation is favored at high finish rolling temperatures, to create coarse austenite grains.[17] The coarse austenite grains allow the acicular ferrite to nucleate intragranularly. The transformation generates dislocations in the highly ductile ferrite phase, which results in favorable fatigue behavior. However, the high finishing temperature generally means longer cooling times resulting in grain coarsening. Grain coarsening is mitigated in polygonal ferrite, which is processed at lower finishing temperatures with smaller austenite grains and shorter cooling times. Smaller polygonal ferrite grains, are advantageous, but lack the dislocation density of acicular ferrite.

The interface between different constituents is generally semi-coherent, generating strain fields and compensating dislocations. High dislocation densities are critical to the mechanical behavior of HSLA and DP steels. Studies[18][19] have shown that the dislocation densities in low-carbon steels are greatest at the grain boundaries and decrease away from the boundary, creating microstructural regions varying in

resistance to plastic deformation. The variation in dislocation density varies across the grains and leads to non-uniform stress distribution. In particular, DP steels have high dislocation density at the martensite-ferrite interface, as opposed to the grain boundaries. The non-uniform stress distribution in the microstructure will manifest itself in the form of hardening and softening as the dislocation substructure changes to distribute the stress more uniformly. The stress eventually stabilizes as the microstructure becomes saturated with dislocations. Although the exact mechanism by which changes occur is not always clear,[3] the dislocation substructure has been shown to reveal a uniform pattern with decreasing density away from the boundary or interface at saturated levels.[19]

2.3.2 Strengthening Micro-alloyed Steels by Precipitation Strengthening

Precipitation is the strengthening mechanism used in the HSLA steel, HR590, to harden the ferrite matrix and refine the grain size. The precipitation process in either case depends on low solid-solubility combined with a sufficiently slow cooling rate to allow diffusion. The precipitates are carbides/nitrides of micro-alloying elements such as V, Ti and Nb. These precipitates form at one of three stages of hot-rolling: 1) When the steel is austenitic, 2) During the austenite-to-ferrite transition and 3) after the eutectoid transformation. In the austenitic state, the solubility of C and alloying elements is high, however diffusion of alloying elements is sluggish, therefore without an additional driving force precipitation happens slowly even if it is thermodynamically favorable. Carbide/nitride precipitation in the austenite phase requires strain energy from mechanical rolling to produce precipitates in a time frame that is conducive to large scale manufacturing. The carbide/nitride precipitates produced during this stage are responsible for controlling grain growth. Precipitates create pinning force energy[6] that creates a barrier to grain growth. If the pinning energy is sufficiently high, either by

quantity or size of precipitates, the grain size will remain fine. When the grain-refined austenite is cooled below the eutectoid temperature, the solubility of the carbon and other alloying elements decreases thereby nucleating additional carbides. Since this is an effect of the eutectoid temperature, the size and spacing of the carbides can be changed by phase stabilizing alloying elements, such as manganese and chromium. However, if the transformation temperature falls below a critical level where diffusion is not active, no precipitation occurs. This is the condition for precipitation from the ferrite phase. Precipitation from the ferrite phase can occur if ferrite is formed using a sufficiently fast cooling rate, preventing diffusion. The steel is then re-heated, so diffusion can occur. The carbides may alter fatigue life by dictating crack path morphology or arresting the crack propagations. These precipitates increase the strength of the material at the expense of ductility and may be detrimental to fatigue behavior in large concentrations, especially if they form a continuous network.

2.3.3 Strengthening of Steels by the Formation of Martensite

If the cooling rate is sufficiently high, diffusion does not have sufficient time to take place and at a critical cooling rate a meta-stable martensite phase forms from the austenite. Within a two phase field the ferrite and austenite co-exist, so upon cooling at the limited volume fraction of austenite can be transformed into martensite and a dual phase microstructure results. The martensite provides microstructural strength, while the ferrite provides ductility. The strength of the dual phase microstructure increases with increasing martensite,[13] but the fatigue life and behavior is not as easily determined by martensite volume fraction. Tayanc et.al. [20] showed that increasing the carbon content in dual phase steels generally leads to better fatigue life, except in cases where the martensite volume fraction exceeded approximately 30%. Therefore, the fatigue-life relationship is not proportional to the martensite content or the strength. Improvements

in fatigue life by increasing the volume fraction of martensite are limited by low ductility, as well as high-energy strain fields between the martensite and ferrite constituents. The fatigue-life relationship is complicated by the carbon content of the martensite phase, which is dependent on the initial concentration, the inter-critical transformation temperature and transformation time. If the initial concentration of carbon is kept constant and the inter-critical temperature is increased, the volume fraction of martensite increases and the carbon content of individual martensite platelets/laths decreases. Decreasing the carbon content of individual grains creates a martensite phase that is more compatible with the ferrite matrix. It has been shown that disregistry between the phases can provide a site for crack initiation during cyclic loading.[11]

The distribution and morphology of the martensite/bainite phases may also affect the fatigue behavior of dual-phase steel. The distribution and morphology is a result of the final processing, discussed in Section 2.1.3. With regards to the dual phase microstructure, the changes in fatigue characteristics during rolling may be attributed to 1) change in the shape of martensite and ferrite leading to improved stress transfer, 2) work hardening, 3) deformation of ferrite grains 4) strain-induced interphase precipitation.[21] The magnitude of these changes will depend on the heat input and time of rolling. Continued rolling at elevated temperatures allows the microstructure to evolve, thereby changing the mechanical properties. In a study performed by Sun and Pugh, [21] rolling of a dual phase steel elongated the grains and increased the volume fraction of the martensite, as expected. However, after continued rolling the martensite volume fraction continued to increase, but the grains became less elongated. The results of the study showed different modes of fracture during impact testing, as a result of the variation in thermo-mechanical treatment.

2.2 Fatigue Response of Micro-Alloyed Steels

Low cycle fatigue tests[22] are performed to determine the relationship between component life and plastic deformation. At high enough strain amplitudes plastic deformation becomes the dominant mechanism leading to crack propagation and ultimately failure.[11] It is expected that components, such as the automotive wheel,[2] experience variations of strains (and stresses) throughout the component life. Some of these strains are expected to be in the plastic regime, therefore it is important to study the fatigue phenomena and how it relates to the microstructure of the steel. It is well established that within the low cycle regime, controlling strain is preferable to controlling stress.[23] Controlling strain prevents large changes in plastic deformation. This is preferable to a stress controlled test in which plastic strain continually changes as the material cyclically softens or hardens and consequently the cumulative effects cannot be measured. Typically a hard material tends to soften, while a soft material tends to harden[22], while some materials such as HSLA and DP exhibit mixed behavior.[24]

The desired primary microstructural phase of low carbon steels, such as HR590 and HR590DP is ferrite. The ferrite is soft and ductile, which has been shown to contribute to better fatigue performance, particularly at high strain amplitudes. However, tensile strength also contributes to fatigue life, particularly at low strain amplitudes. Ideally, the maximum contribution of both strength and ductility would give the best fatigue performance, however one is usually developed at the expense of the other. The combination of strength and ductility is referred to as toughness, so the goal in developing a microstructure with good fatigue characteristics is to optimize the toughness for a constant strength level. For fatigue performance, it is also important to develop a microstructure which minimizes the crack initiation. During a fatigue test, a crack normally nucleates at some discontinuity, such as a notch, slip band, grain

boundary, second phase particle or inclusion[18]. Once the crack is initiated it continues to propagate through the structure creating highly stressed and deformed regions. The crack tip generates large plastic strains, localized to the tip, allowing it to easily propagate throughout the structure. Materials with high hardness tend to resist crack initiation, but offer little resistance to crack propagation. By optimizing the toughness at the required strength level both crack initiation and propagation can be controlled.

2.2.1 Cyclic Stress Strain Properties for Fatigue Analysis

The cyclic stress-strain response for a material is typically different from the monontonic-unidirectional (tension or compression) stress-strain response and quantification of these differences provides useful information on the fatigue behavior. The cyclic response of a metal can quickly change until a saturation level is reached. Therefore, the cyclic stress-strain response is typically quantified at half of the total fatigue life to provide a representative response in the stress-strain behavior. The stress-strain response at half-life is then compared with the monotonic stress-strain response to understand the differences in monotonic and cyclic aspects of the plastic deformation. The monotonic stress-strain response can be modeled using a Holloman power law relationship, as follows:

$$\boldsymbol{\sigma = K(\varepsilon_p)^n} \qquad \textbf{Eq. 1}$$

Where σ is the stress response, K is the strength coefficient, ε_p is the plastic strain and n is the strain-hardening exponent. The strength coefficient, K, is a theoretical number that represents the amount of stress when the plastic strain is equal to one. As the plastic deformation increases the slope of the stress-strain curve decreases. This decrease in slope is determined by the strain hardening coefficient, n. Therefore, a high n-value will have a stress response that is more sensitive to plastic strain and the physical

consequence is the material resists strain at a non-proportional rate. The non-proportionality in the stress-strain responses is due to changes in the material flow properties.

Similarly, it can be shown that the cyclic response can be modeled as:

$$\frac{\Delta\sigma}{2} = \boldsymbol{K'}\left(\Delta\boldsymbol{\varepsilon_p}\right)^{\boldsymbol{n'}} \qquad \textbf{Eq. 2}$$

Where K' is the cyclic strength coefficient and n' is the cyclic strain-hardening exponent. During repeated loading and unloading, plastic deformation is accumulated on the specimen and creates a more complex relationship between plastic strain and stress, resulting from the change in flow properties. The value of the cyclic strength coefficient, K', can be very different from the monotonic value indicating a change in the theoretical value of stress when $\varepsilon_p = 1$. Similiarly, the value of n' can change as well indicating a change in the rate of the stress response. A higher value generally means a higher rate of work-hardening with accumulated strain. The magnitude of the coefficients and exponent between monotonic and cyclic tests is one way to determine if the material is hardening or softening. Therefore, differences between monotonic properties and cyclic properties can be quantified using this relationship.

HSLA steels, such as HR590, have mixed fatigue behavior even with differences in composition.[3] The mixed behavior is shown by a stress-strain curve that crosses the monotonic stress-strain curve at some critical level of plastic deformation. The mixed behavior is attributed to dislocation motion and interaction within the grains. Gupta et.al.[18] made this observation in HSLA steels, showing that the dislocation density was higher at grain boundaries, a function of grain size and partially responsible for increased fatigue life. Sherman[5] also performed fatigue experiments with HSLA steels and comparatively the HSLA had longer fatigue lives when compared to hot-rolled low

carbon steels that did not benefit from micro-alloying additions. However, because of better processing technology, it is possible to produce steels with lower carbon contents than the steels tested by Sherman. In HSLA steels, micro-alloying elements can also be better controlled using current technology, which has provided the basis for strengthening by grain refinement. The current grain refinement methods have allowed for less dependence on carbon and more on strengthening mechanisms the minimize ductility losses.

Changing the carbon content affects the volume fraction of martensite that can be formed in a dual phase structure[20] and consequently fatigue life.[16] Dual phase steels with favorable fatigue properties initially harden then soften with increasing fatigue cycles. Depending on the rate of hardening, this behavior may produce a cyclic stress-strain curve showing softening when the data is taken at half-life, as hardening would occur at the earlier cycles. Sherman et. al.[25] examined the unique stress-strain response in dual phase steels showing that the initial high degree of work hardening prevents the onset of softening and contributes to longer fatigue life. Studies on dislocation density have revealed that there is a non-homogeneous distribution of dislocations, with the martensite boundaries being the preferred sites for dislocation generation.[16] This non-homogenous distribution of dislocations results in a non-uniform stress distribution until compatibility requirements are fulfilled between grains. The phase lag to fulfill compatibility requirements is associated with the initial high work hardening rate.

2.2.2 Cyclic Strain-Life Properties for Fatigue Analysis

During the fatigue life a material will typically go through three stages:[23]

Stage 1 – Initiation of one or more microcracks due to plastic deformation

Stage 2 – Progression to macrocracks with plateau like surfaces, normal to the direction of stress, separated by longitudinal ridges

Stage 3 – The crack has propagated to where the material can no longer support the loads and fractures

For strain controlled fatigue tests, the fatigue life data is usually presented in the format of strain-life plots. For comparison purposes it is of interest to fit the strain life data to an appropriate model/equation. Fatigue life models are also useful in determining the service life of a particular material. Steels are unique in that they exhibit an endurance limit (also known as the fatigue limit) in which the material will support a minimal load for an infinite number of cycles. Beyond this minimum load the life of the material is finite. The finite region can be modeled by the following equation:[24]

$$\frac{\Delta\varepsilon}{2} = \frac{\sigma_f'}{E}\left(2N_f\right)^b + \varepsilon_f'\left(2N_f\right)^c \qquad \textbf{Eq. 3}$$

The left hand side of the equation represents the strain amplitude. The strain amplitude is put in the form shown, to provide a uniform model for testing that may not have fully reversed loading histories. The first part of the right hand side of the equation represents the elastic component of the strain, where σ_f' is the fatigue-strength coefficient, $2N_f$ is the number of reversals to failure and b is the fatigue-strength exponent. The second part of the right hand side of the equation represents the plastic component of the strain, where ε_f' is the fatigue-ductility coefficient, $2N_f$ is the number of reversals to failure and c is the fatigue ductility exponent. During testing at high strain amplitudes the life is expected to be relatively short and therefore the plastic term dominates the equation and the opposite would be true at smaller strain amplitudes. This equation proves to be a good fit for a large variety of materials, although has found been found insufficient for some dual phase steels.[26]

Chapter 3: Experimental Work

The central objective this research is quantitative characterization of the differences in the fatigue behavior of HR590 micro-alloyed HSLA steel and HR590DP dual phase steel of the same tensile strength grade. For this purpose, experiments have been performed to characterize the fatigue behavior, microstructures and fracture surfaces of the steels of interest. This chapter describes the experimental procedures used for preparing the steels, fatigue testing the steels, analyzing the fatigue data and the microscopy techniques involved in the characterization of the microstructure and fracture surfaces. The data gathered from these experiments are analyzed in the next chapter to understand the fatigue behavior of the steels of interest.

3.1 Materials and Processing

3.1.1 Material Chemistry

The nominal chemical compositions of the HR590 and HR590DP steels are shown in Table 1. The carbon content of these steels is generally low with relatively higher carbon content in the HR590. The higher carbon content of the HR590, HSLA steel, facilitates the required strengthening by precipitating carbides of the micro-alloying elements Ti and Nb. These carbides not only strengthen the steel by precipitation hardening, but also restrict the grain growth of austenite as carbides pin the grain boundaries. Manganese stabilizes the austenite phase, increases hardenability

Table 1: Chemical Composition by wt.% of HR590 and HR590DP

	C	Mn	Si	Cr	Nb	V	Ti	Al	P	S	N
HR 590	0.0855	1.36	0.12	0.043	0.042	0.005	0.034	0.017	0.012	0.006	0.0041
HR 590DP	0.0599	1.194	0.122	0.497	0.002	0.006	0.003	0.032	0.014	0.001	0.0056

and combines with sulfur impurities to form Mn-rich inclusions. The formation of Mn-rich inclusions has been shown to improve fatigue life in bearing steels by creating compressive stresses in the surrounding matrix.[27] The relatively higher Cr content of the HR590DP, dual phase steel, stabilizes the ferrite phase and is partly responsible for its high hardenability. All other elements appear to be standard concentrations and assist in the strengthening or deoxidization of the steel.

3.1.2 Specimens for Characterization of Fatigue Behavior

The steels of interest, HR590 and HR590DP, were provided by ArcelorMittal Global R&D in East Chicago, IN. The processing of the steels of interest is proprietary and therefore not reported here. The steel specimen-blanks were drawn from HR590 and HR590DP, 3.2mm thick commercial coils. The specimens were marked, outside the test section, with the last three alphanumeric digits of coil identification (See Table 2). Fatigue test specimens of “dog-bone” geometry were machined at ArcelorMittal Global R&D from the specimen-blanks. The specimen geometry and dimensions are shown in Figure 3. The specimen faces were not machined or modified and have the same surface finish as the coils from which they were drawn. The width of these fatigue specimens is along the rolling direction of the coil, whereas the length (loading direction) is transverse of the rolling direction. The final specimen dimensions deviate from those found in ASTM E606-04 *Standard Practice for Strain Controlled Fatigue Testing*[28] by using a square (3.2mm x 3.2mm) gage dimension in lieu of the rectangular cross section; this simplifies the relationship between the axial deformation and cross-sectional deformation. The simplified relationship allows the conversion of engineering strain to true strain by using Poisson’s ratio (ν). Visual inspection of the specimens showed exposed areas where the machining process had removed material along the edges.

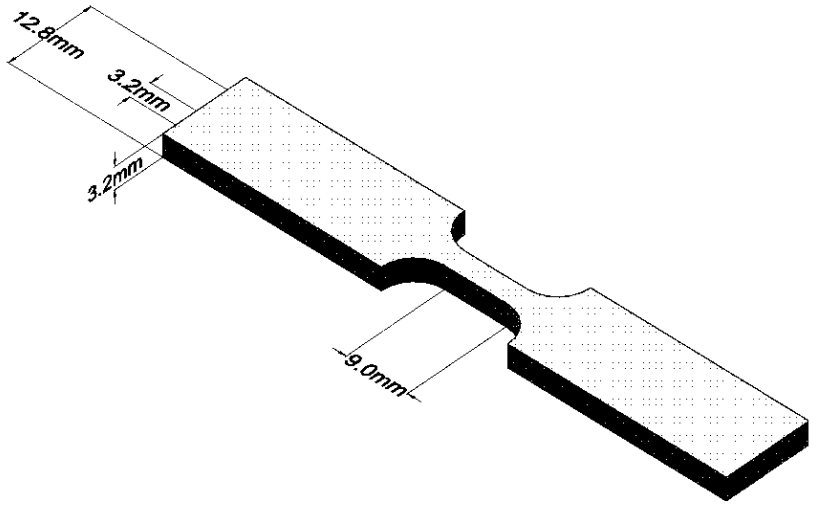

Figure 3 - Dimensioned specimen used for low-cycle fatigue testing

Table 2: Specimen type, coil and rolling direction

	Specimen ID	Coil No.	Rolling Direction w.r.t. Gauge Length
HR 590	59B	39459B	Transverse
HR 590DP	385	797385	Transverse

A surface coating on the planar section of the specimens, which presumably provided corrosion resistance, was also present. Specimens were carefully inspected for any visible surface defects, including but not limited to scratches due to handling, corrosion due to environmental exposure and metal shavings or burrs resulting from the machining process. Any metal shavings or burrs resulting from machining were removed prior to testing using a small fine-coarse file. Likewise, the surface coating was removed from the rolled surface for the following reasons 1) to provide accurate measurement of the gage dimensions prior to testing 2) to remove metal shavings or burrs that remained

close to the rolled surface 3) to remove any surface defects as a result of handling 4) to provide a standard surface for all specimens free of surface defects, metal shavings and burrs. All filing was done in the direction longitudinal to the gauge section to limit the influence on fatigue life. Preparations were completed directly prior to testing to limit environmental degradation. After the surfaces were prepared and prior to testing, the gage dimensions were measured using a Vernier Caliper accurate to +/- 0.0005in (0.0127mm). Gage measurements were used to calculate stress from the loading data.

3.2 Monotonic Mechanical Properties Data

The monotonic mechanical properties of each specimen, shown in Table 3, were provided by ArcelorMittal Global R&D for test setup and comparative analysis. Based on the values provided, a model using the Holloman power-law relationship (Eq. 1)[24] was constructed to predict the stress-strain relationship in the plastic deformation regime. The model was used to determine the failure load of the individual specimens, which is discussed in Section 3.2. In order to construct this model, assumptions were made about the plastic strain behavior. Plastic deformation at the yield strength should be negligible; however power-law behavior does permit a zero plastic strain value. A standard method for determining yield strength[29] is to use a 0.2% strain offset. Therefore, 0.2% plastic strain at the yield strength was assumed. Since micro-plasticity exists, even at the yield strength of the material, this assumption was determined to be a reasonable. Another assumption is that only one mode of plastic deformation exists. Some steels may show

Table 3 - Monotonic Mechanical Properties of Tested Specimens

	Yield Stress (MPa)	Ultimate Tensile Stress (MPa)	Work Hardening Coefficient	Total Elongation (%)
HR 590	570	650	0.12	22
HR 590DP	420	640	0.15	26

more than one plastic deformation mode and would require multiple work hardening coefficients to accurately model the stress-plastic strain relationship. Nonetheless, for initial setup only, one work hardening coefficient is sufficient.

3.3 Fatigue Experiments

Axial strain controlled fatigue experiments were performed on HR590 and HR590DP fatigue specimens at the strain rate of 0.005mm/mm per second. Experiments were performed at different strain amplitudes ranging from 0.02 to 0.002 to obtain the fatigue life data in the range of 100 to 200,000 cycles. Multiple specimens were tested at each strain amplitude in accordance with ASTM STP 588[30] to account for variability in fatigue life behavior. The details of the fatigue experiment parameters are given in Table 4. The experiments were performed at Georgia Institute of Technology on a servo-hydraulic machine of 20,000lb load capacity with a load accuracy of +/- 20 lbs. The specimen extension was monitored using an 8 mm extensometer having an accuracy of +/-0.001mm/mm. All fatigue experiments were performed at room temperature. The fatigue experiments were performed in accordance with ASTM E606-04.[28] The hysteresis loops of the specimens were recorded at logarithmic intervals for detailed analysis of the fatigue behavior.

Specimen alignment is particularly important issue in fatigue experiments on the specimens of small cross-sections such as those in the present work. Specimen alignment in the testing fixture was performed using a representative sample. The representative sample was centered to within +/- 0.0005in (0.0127mm) (i.e. the accuracy of the Vernier Caliper). All test specimens were subjected to the same alignment as the representative specimen. Alignment was monitored during testing for loading eccentricities, which cause buckling and invalidate the experiment. Grip measurements

Table 4 - Low Cycle Fatigue Test Parameters

Control Mode	Axial Strain
Strain Rate	0.005/second
Strain Amplitude **(Amplitude Identification No.)**	0.0200(7), 0.0170(6), 0.0140(5), 0.0110(4), 0.0080(3), 0.0050(2), 0.0035(1_5), 0.0029(1_3), 0.0023(1_1), 0.0020(1)
R-Ratio	1.0 (Fully Reversed)
Waveform	Triangular
Failure Criteria	50% of Estimated Max. Load

were performed prior to testing, in the event buckling occurred. The grip width was measured using a digital micrometer accurate to +/- 0.0005in (0.0127mm). No loading eccentricities were visible at any point during the experiments. Once measurements were performed and recorded, double-faced tape was applied to the surface on which the extensometer was affixed. Double-faced tape was used to prevent the extensometer knife edges from drifting during cyclic loading. The tape also provided a barrier to mitigate preferential crack initiation at the knife edge.

3.4 Metallographic Specimen Preparation and Digital Imaging

To view the microstructure and characterize the features that influence fatigue life, the specimens required metallographic preparation for optimal viewing in the optical and electron microscope. To facilitate the viewing of the unstressed, bulk microstructure in three-dimensions, cuts were made parallel to the rolling direction(longitudinal), perpendicular to the rolling direction, (transverse) and planar of the rolled surface. The cuts relative to the specimen grip section are shown in Figure 4. The specimens were cold-mounted using an epoxy mold exposing each of the three sections. The mounted specimens were grinded using SiC metallographic papers ranging from 400-grit to 1200-grit. Constant application of water on the metallographic papers prevented specimen

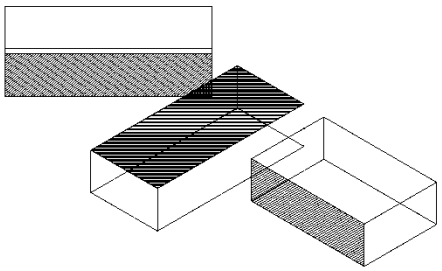

Figure 4: Section cuts and planes taken from the gauge section of the test specimens

heating and kept the surface clean. The specimen was rotated 90-degrees between grinding steps to prevent re-deposition of grinding byproduct. Polishing was performed by rotating lapping cloth with a colloidal diamond abrasive solution, ranging from 15µm to 1µm diamond size. The specimen was under constant rotation during polishing to prevent uni-directional polishing and "smearing" of debris across the surface of the specimen. Final polishing was performed in the same manner, using 0.05µm alumina as the polishing media. After final polishing the specimen was cleaned with ethyl alcohol and dried.

In order to expose the grain boundaries of the HR590 (HSLA) specimen, an acid etch was used to preferentially attack the grain boundaries. The acid etch solution consisted of ~2% nitric acid (HNO_3) in ethyl alcohol. Etching was done in 5-second increments and checked for contrast in the optical microscope to determine if further

etching was needed. Total etching time was approximately 20-seconds. In order to expose the grain boundaries of the HR590DP (Dual Phase) specimen, an acid etch solution of ~4% nitric acid (HNO_3) in ethyl alcohol was used. A secondary acid etch of sodium meta-bisulfite was used to expose the marensite phase of the dual phase steel. Etching was done in 5-second increments and checked for contrast in the optical microscope to determine if further etching was needed. Total etching time was approximately 20-seconds.

Optical microscopy was performed on the etched specimens using a Zeiss AXIOVISION with digital imaging software. The microscope resolves 0.1253µm at 80x magnification. The imaging software stitched large numbers of individual images together to create a montage. The montage ensured that the microstructure could be evaluated on a small scale over a large area free from bias. Additional high-resolution single images were also taken of various areas of the microstructure.

3.5 Fractography of the Fatigue Surface

A fatigue fracture surface is typically tortuous due to repeated deflection of a propagating crack tip. This tortuosity prevents the optical microscope from resolving clear images at high magnifications and necessitates the need for the scanning electron microscope. For this purpose a Hitachi S-4000 scanning electron microscope was used to acquire images ranging from 150x to 3000x magnification. For lower magnification images a stereomicroscope was used to acquire images up to 50x magnification.

When possible the fractured fatigue specimen was left intact to preserve the profiles. By keeping the surfaces intact, handling damage and environmental contamination was limited. To further limit environmental contamination, fatigue specimens were maintained in a desiccator until microscopy work was ready to be

performed. Prior to microscopy, specimens were separated by applying a tensile load that opened the fatigue crack. Subsequent closure of the fatigue crack was prevented, so that no extraneous effects would be observed in the microscope. The surfaces were cleaned by submersion in an acetone bath while ultrasonically cleaning. Cleaning was performed until all debris was removed, usually about 10mins. After cleaning, the specimens were rinsed with ethyl alcohol and immediately dried to inhibit the formation of oxides on the surface. Once dry the specimens were viewed in the SEM at Georgia Tech Research Institute.

The stereomicroscope provided good depth resolution at low magnifications for qualitative analysis. The advantage of this method is quick observation of the fracture without the setup involved with the SEM. The stereomicroscope allowed the analysis of a large number of samples to detect trends in crack initiation and propagation. The stereomicroscope also provided images of the specimen surfaces and any discontinuities that may have contributed to fatigue failure.

Chapter 4: Results and Discussion

The main thrust of this research is the quantitative characterization of the low-cycle fatigue behavior of micro-alloyed HR590, HSLA steel, and HR590DP, dual-phase steel. The experimental work is reported in the previous chapter. The experimental data and the results of the experiments are presented and analyzed in this chapter. This experimental data includes qualitative microstructural observations, monotonic loading behavior, cyclic loading behavior and qualitative observations of the fracture surfaces. The conclusions drawn from the analysis of experimental data are summarized in the next chapter.

4.1 Microstructural Observations of HR590 and HR590DP Steel.

4.1.1 Bulk Microstructure

The bulk microstructure is characterized in the three major axes relative to the rolling direction of the test specimen. Together, planes from each of the axes provide a three-dimensional representation of major microstructural constituents. The three-dimensional images are shown in Figure 5. The three-dimensional images are intended for reference only to highlight the qualitative differences between the microstructures and are not intended for quantitative analysis.

The three planes are etched to expose the grain boundaries and microstructural constituents. These etched microstructures are shown in Figure 5 and Figure 6 representing the magnification indicated on the scale bar and not necessarily derived from the previous three-dimensional images. The etched bulk microstructure of HR590, depicted in Figure 6, shows lighter ferrite grains with darkened grain boundaries. The ferrite grains have a polygonal grain shape with carbides/nitrides along the grain boundaries. The transverse and longitudinal sections show “pancaked” grains, as a

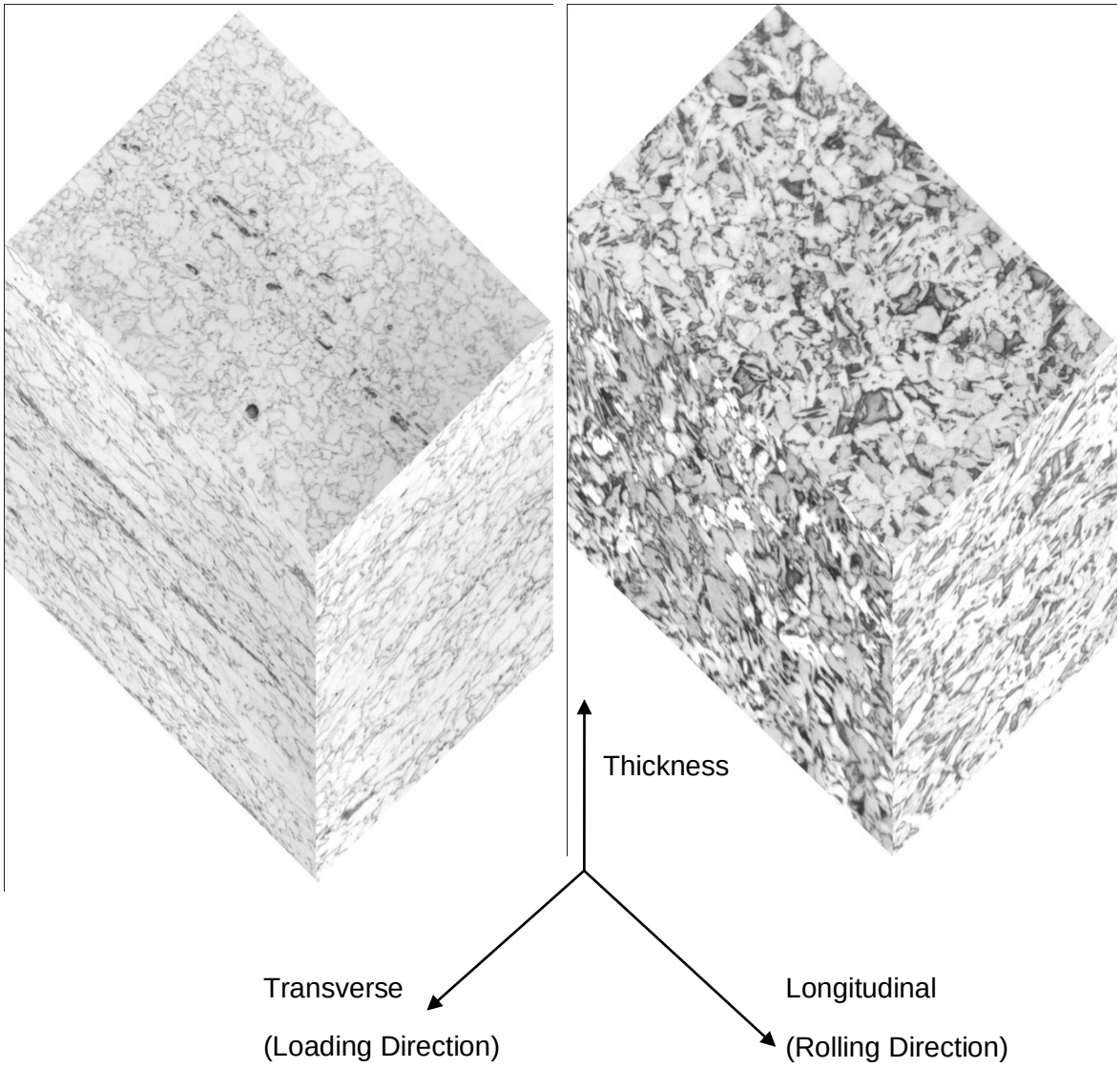

Figure 5: Three-dimensional representation of HR590 and HR590DP using section cuts from the transverse, thickness and longitudinal planes a) HR590 b) HR590DP

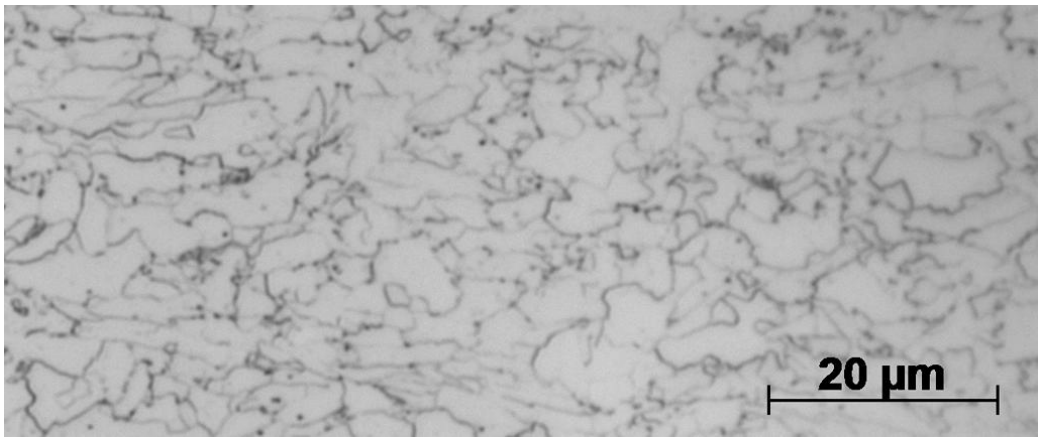

Longitudinal (Rolling) Direction

(a)

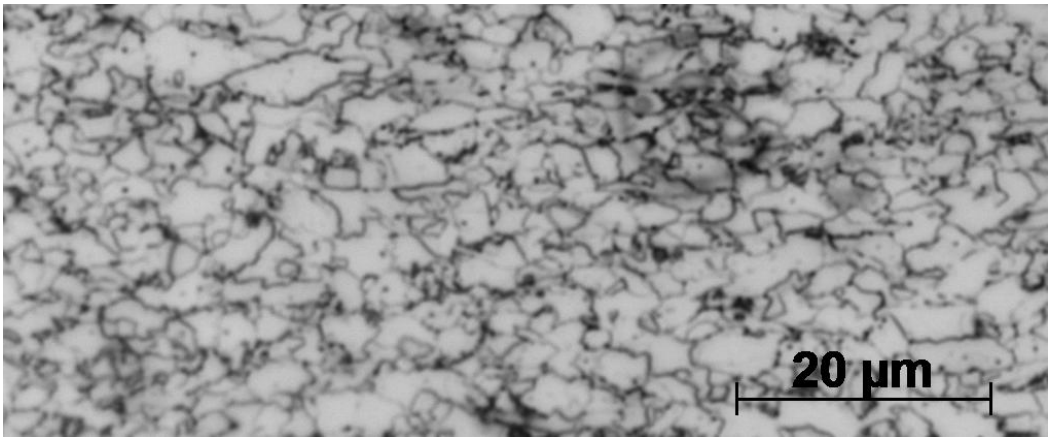

Transverse (Loading) Direction

(b)

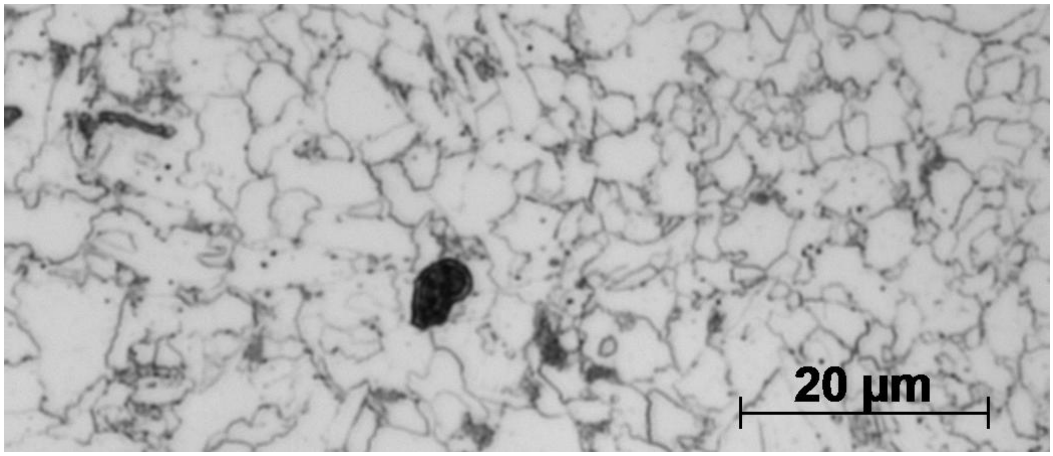

Longitudinal (Rolling) Direction

(c)

Figure 6: HR590 steel microstructure a) transverse plane b) longitudinal plane c) thickness plane

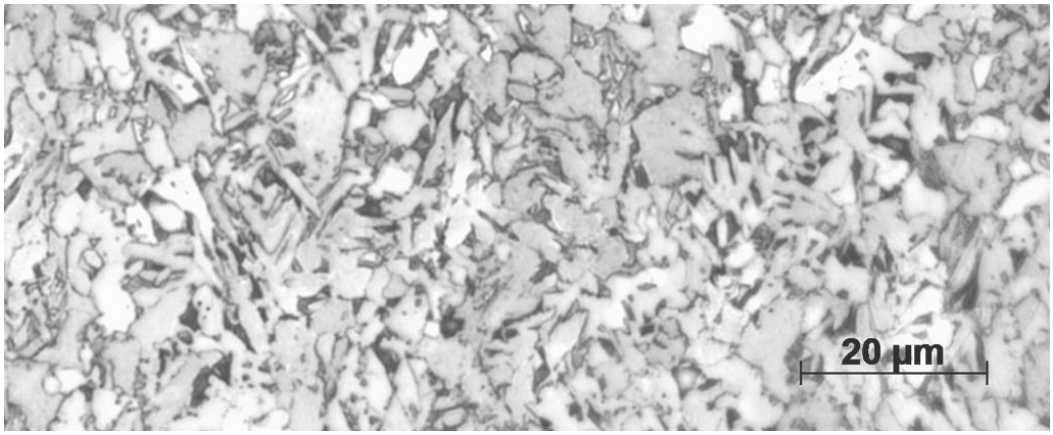

Longitudinal (Rolling) Direction

(a)

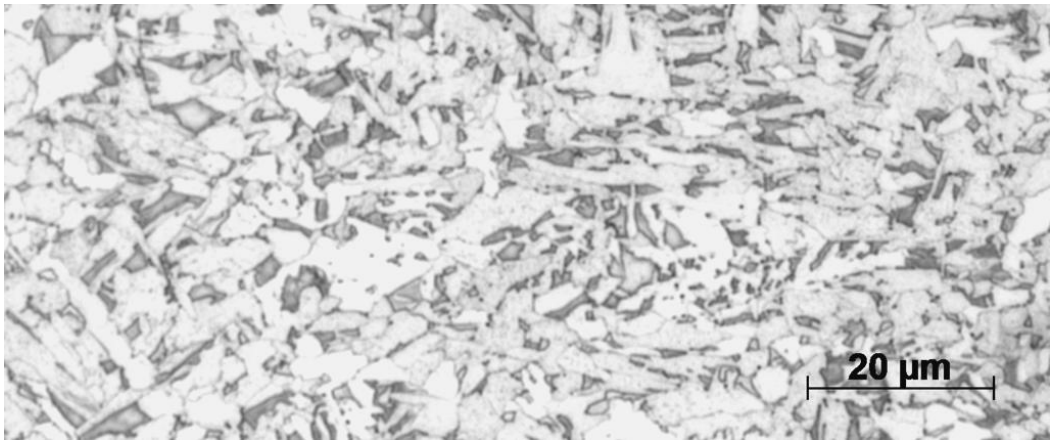

Transverse (Loading) Direction

(b)

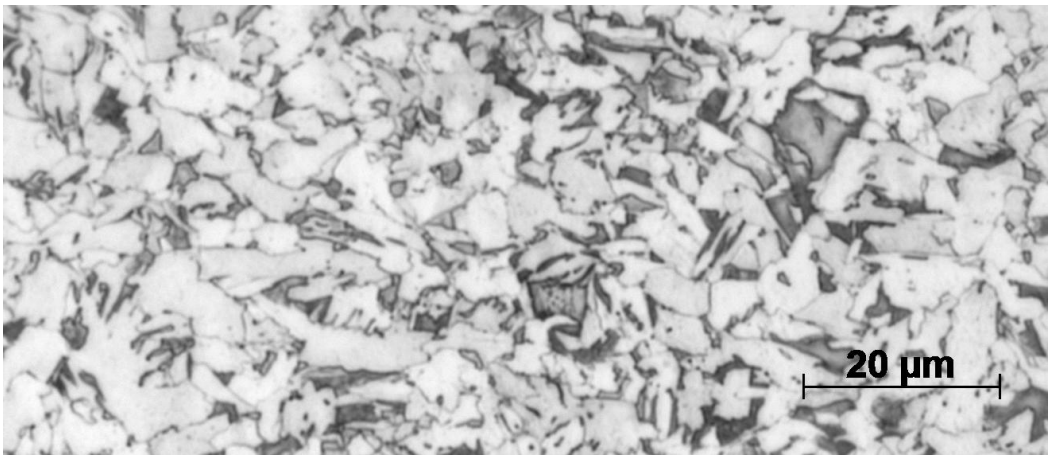

Longitudinal (Rolling) Direction

(c)

Figure 7: HR590DP steel microstructure a) transverse plane b) longitudinal plane c) thickness plane

consequence of hot-rolling. The bulk microstructure of HR590DP, shown in Figure 7, shows the ferrite grains as light colored and the secondary martensite/bainite regions tinted resulting from a secondary sodium meta-bisulfite etchant. The etchant used depicts intermediate tint for bainite that is lighter than martensite and darker than ferrite. For ferrite grains that are particularly susceptible to etchants, from grain orientation, etc., the ferrite may be mistaken for bainite if over-etched. Both HR590 and HR590DP steels have comparable grain sizes with an average caliper diameter of ~10µm.

4.1.3 Inclusions

Inclusions generally form from non-metallic impurities and provide an interface that may affect mechanical properties. The extent to which inclusions affect fatigue of hot rolled steel is dependent on a variety of factors, including the loading direction, distribution, and the chemical composition of the inclusions. Efforts to completely eliminate inclusions are commercially prohibitive due to the additional cost and processing time. Therefore, inclusions are unavoidable in commercial processing and present in HR590 and HR590DP. The two most notable projected shapes of inclusions, in HR590 and HR590DP, are round (Figure 8, Figure 9a) and elongated “stringers” (Figure 9b). The elongated morphology is a characteristic of sulfide inclusions, which are deformed by the hot-rolling process. The round morphology has a variety of chemical compositions that include calcium based compounds. Calcium is generally added for inclusion shape control to mitigate the effect on mechanical properties.[(31)] Hot-rolled steels exhibit anisotropic mechanical behavior as a result of processing. Recently, Ma et.al.[(32)]investigated the effects of inclusions on fatigue crack initiation for loading directions at 0, 45, 90-degrees to the rolling direction. The results of the research show that crack initiation resulting from inclusions becomes more probable as the projected

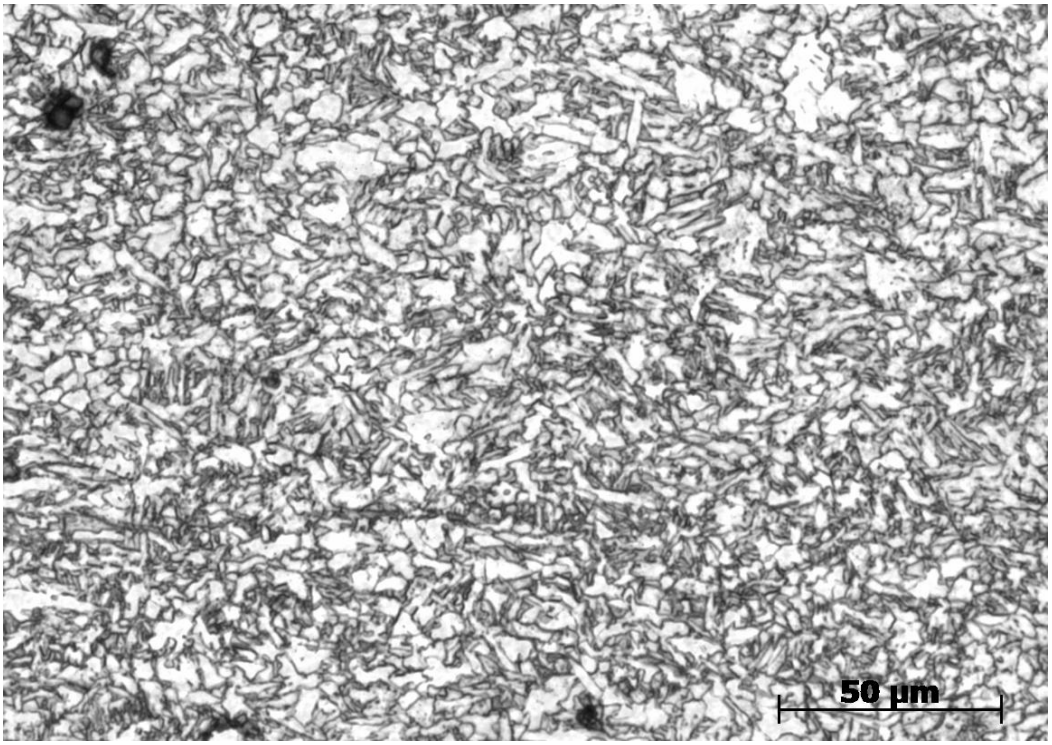

Figure 8: Microstructural inclusions observed in HR590DP

area of the inclusions becomes greater and the inclusions become closer to the surface. However, it should be emphasized that the projected area and distribution of inclusions alone may not explain crack initiation.

Comparison of the inclusions in both HR590 and HR590DP reveal that both round and elongated projected shapes are distributed throughout the microstructure; however the inclusions in HR590DP are both smaller in size and lesser in extent. The largest inclusions in HR590 are in excess of 20µm, while the inclusions in HR590DP are typically less than 20µm.

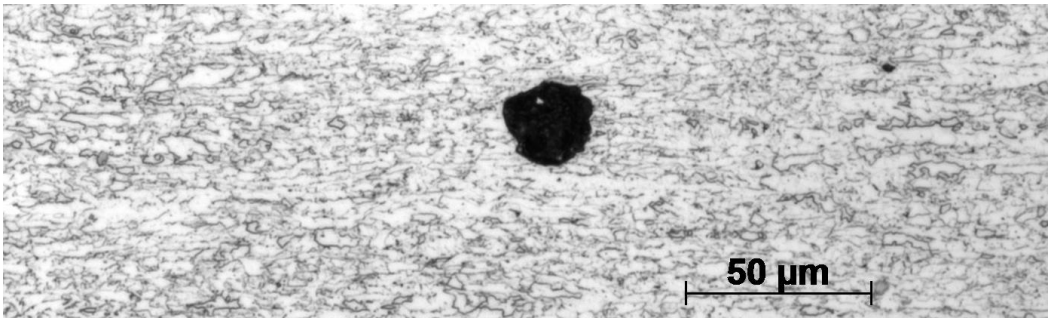

Longitudinal (Rolling) Direction

(a)

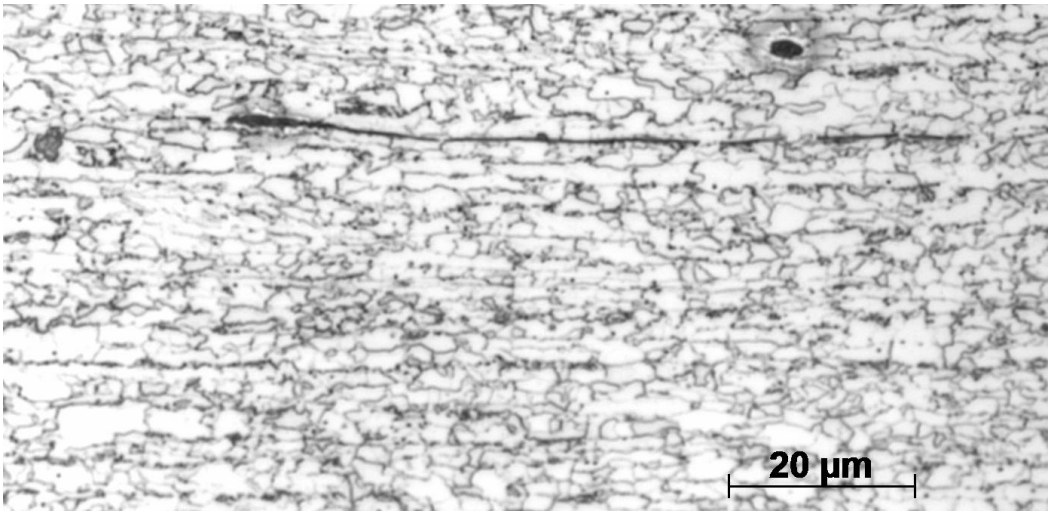

Longitudinal (Rolling) Direction

(b)

Figure 9: Microstructural inclusions observed in HR590 a) Round b) Elongated

4.1.4 Segregation of Microstructural Features

Segregation resulting from solidification is projected as bands in the microstructure. Segregation of microstructural phases in HR590 and HR590DP was observed in the optical microscope at the grip section of the test specimen. SEM imaging of HR590 revealed the segregated region as a distribution of lamellar and non- and longitudinal test sections. An energy dispersive spectroscopy (EDS) analysis was done to determine the chemical composition in the pearlite regions. The pearlite showed ~3.44wt% +/- 0.29 Mn as opposed to the reported average value of 1.36wt% for the coil.

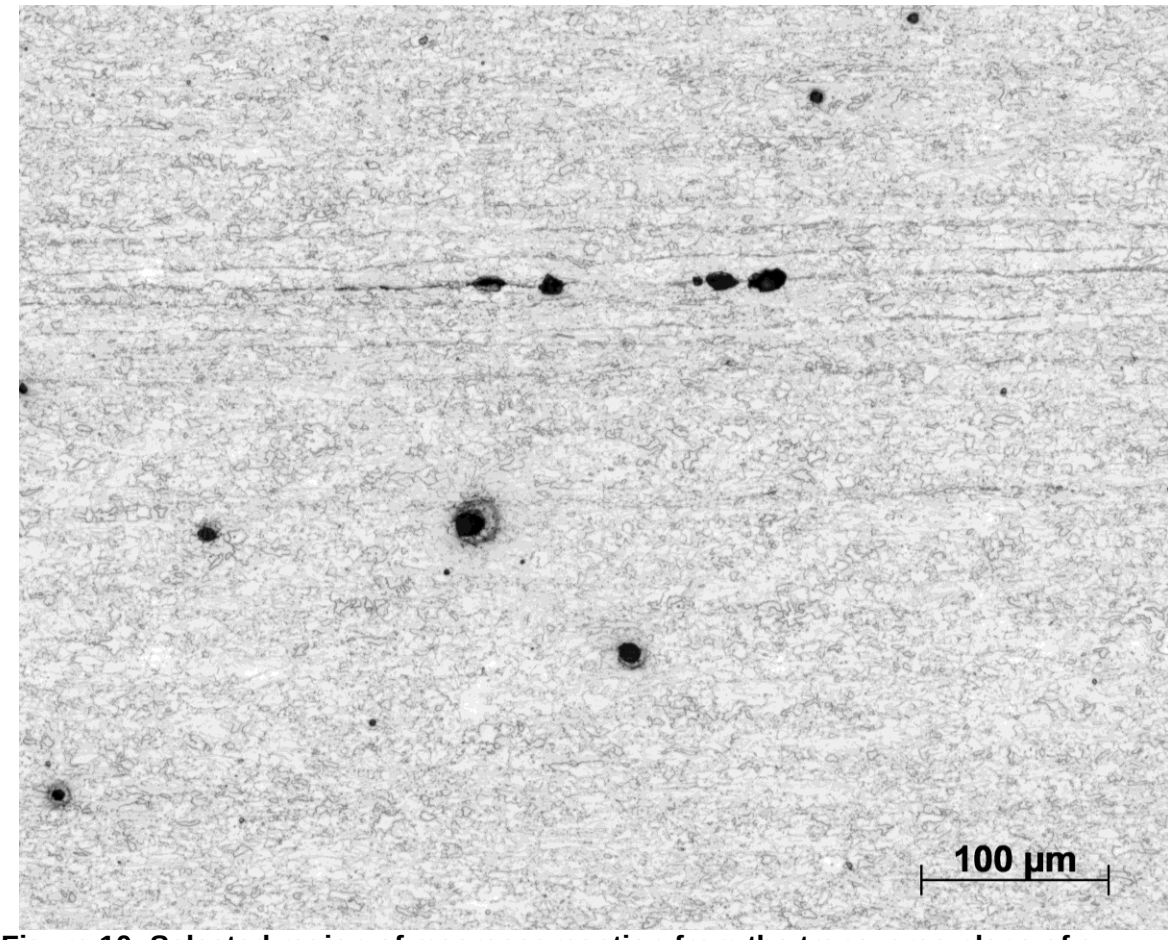

Figure 10: Selected region of macrosegregation from the transverse plane of a HR590 specimen

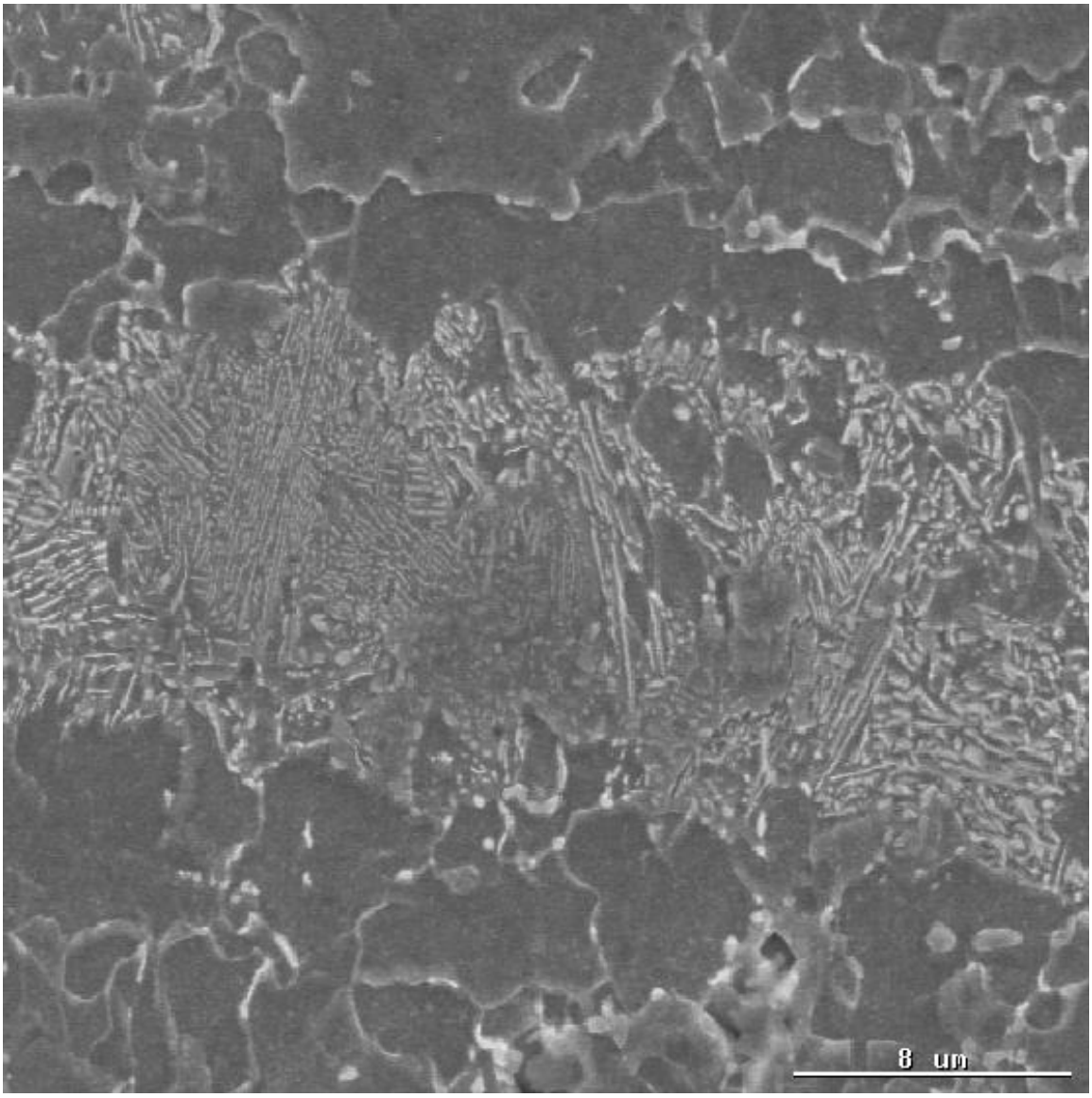

Figure 11: SEM image of segregated region in HR590

An area free of pearlite and next to the segregated region showed ~1.64wt% +/-0.19, indicating the bands were Mn-rich. Additionally, the pearlite structure indicates that these regions were also C-rich. lamellar constituents (Figure 11). The lamellar constituent is pearlite, while the non-lamellar constituent is ferrite. The pearlite was localized to the center of the transverse

Similarly, optical microscope observations of HR590DP show macrosegregation. SEM imaging revealed that the segregated region consisted of a high volume fraction of martensite near the center. The EDS showed a Mn concentration of ~2.45wt% +/-0.21 in the center region with high volume fraction of martensite and a Mn concentration of 1.48wt% +/-0.19 slightly away from the center region. The average Mn concentration for the coil was reported as 1.19wt%, indicating Mn-rich bands. Similar to HR590 the Mn-rich bands of martensite are C-rich, although due to processing differences the microstructures are different. Further observation of HR590DP shows hot-cracking

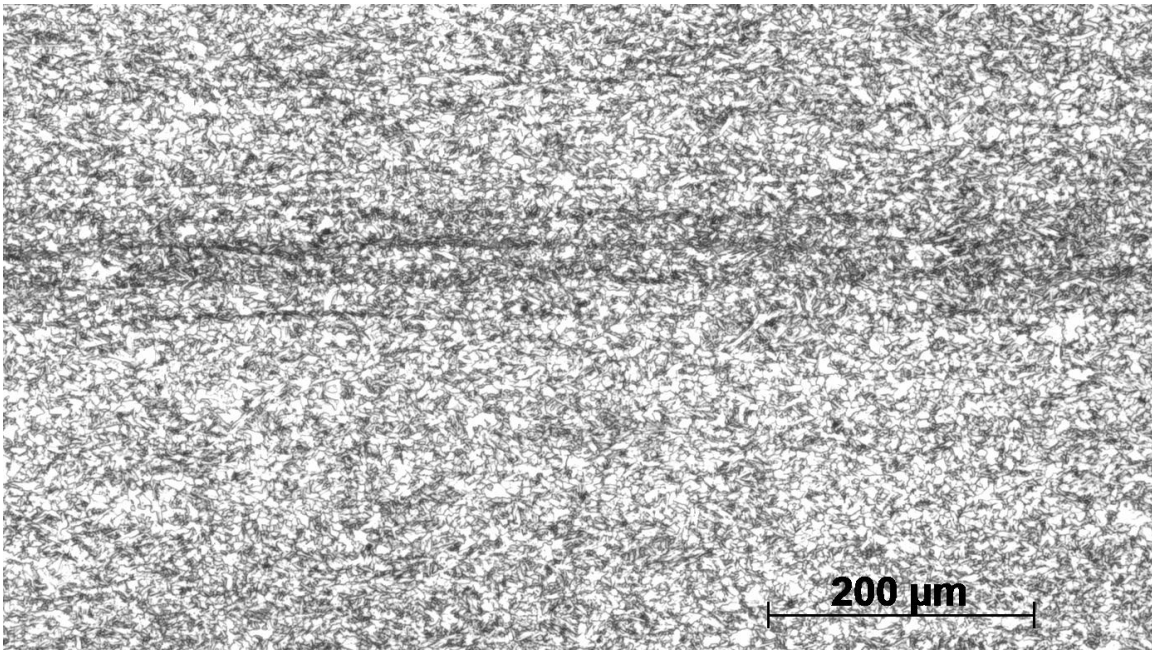

Figure 12: Selected region of macrosegregation from the transverse plane of a HR590DP specimen

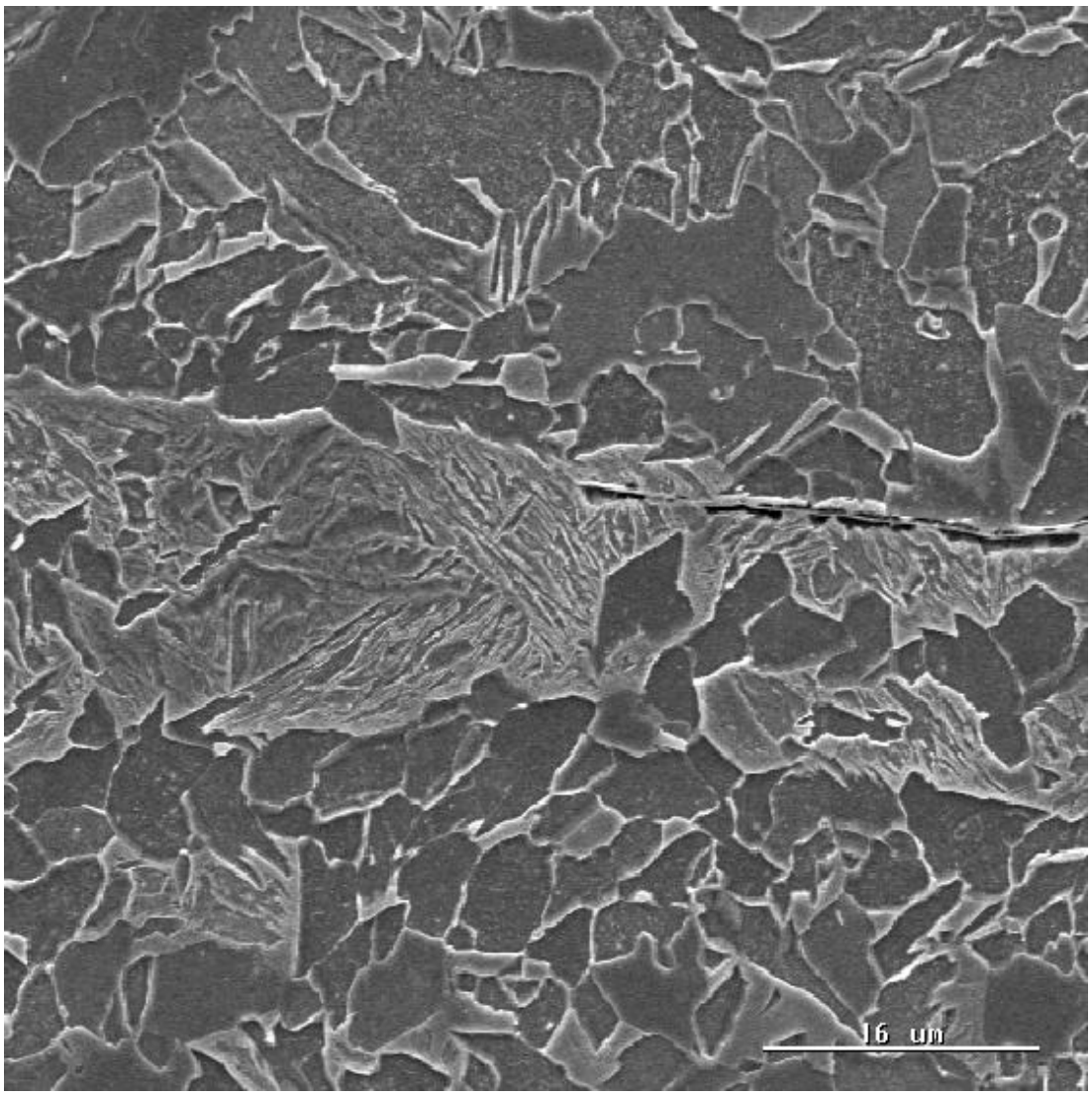

Figure 13: SEM image of segregated region in HR590DP

(Figure 14)**.** Hot-cracking occurs in steels with high Mn concentrations as a result of variations in temperature gradients across the microstructure resulting from the austenite stabilized Mn-rich regions.[8] The loading direction for this series of fatigue tests is parallel to the hot crack direction; therefore effect on fatigue life is minimized.

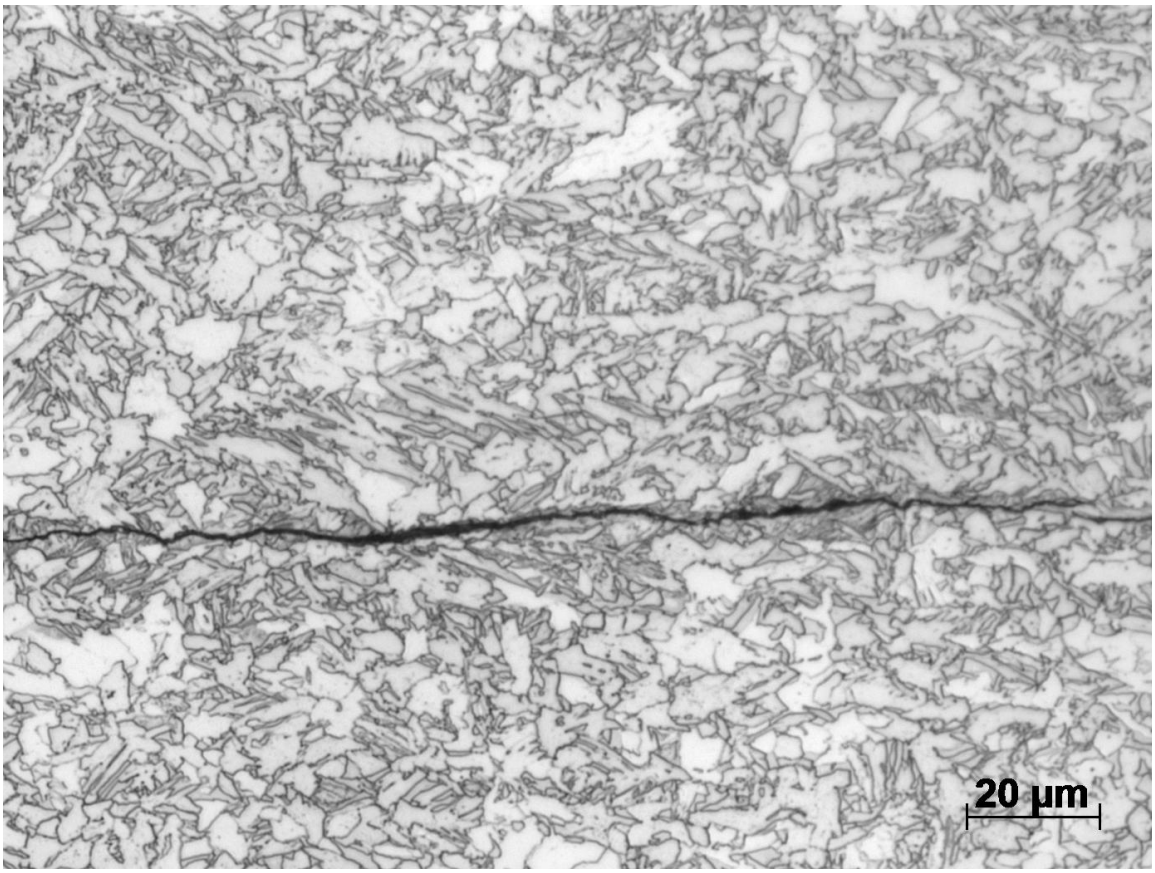

Figure 14: Selected region of hot-cracking from the transverse section of a HR590DP specimen

4.2 Monotonic Mechanical Properties

The monotonic tensile response of HR590 and HR590DP is shown in Figure 15. The yield point of HR590 is muted with yield point elongation immediately following. Two possible causes of the muted yield point in HR590 are 1) the addition of strong carbide/nitride formers, which pull interstitial atoms from the dislocations or 2) pre-straining of the specimen, which un-pins the dislocations from the precipitates.[33] The yield point elongation is characterized by the plateau in the stress-strain curve and results from a critical strain energy that allows the unpinning of dislocations. The strain range of this plateau is dictated by the rate at which plastic deformation spreads through the specimen gage section. The mobility of dislocation in HR590 provide discontinuous

stress-strain response in lieu of the more continuous stress-strain response exhibited in HR590DP, which is nearly free of dislocation pinning precipitates. The more continuous stress-strain behavior of HR590DP provides a greater rate of work hardening, which can be quantified by the work hardening exponents (i.e. n-value) and strength coefficients (i.e. K-value). HR590 has a work hardening exponent of 0.1055, as opposed to 0.1198 for HR590DP. The strength coefficient is 927MPa for HR590 versus 934MPa for HR590DP. Differences in work hardening have been partially attributed to grain size and pinning of dislocations by interstitial content and precipitates;[18] however the grain sizes of the two steels of interest are relatively similar. Therefore, the mobility of dislocations within the grains is of particular importance to the work hardening of the two steels. HSLA steels, such as HR590, show an increase in dislocation density at the grain boundaries.[18] In dual phase steels, such as HR590DP where there are few if any precipitates, the dislocation density is greater at those grain boundaries where there is a martensite-ferrite interface.[16][19][20] Due to the differences in dislocation distribution, HR590 provides a more uniform distribution of stress in the microstructure when a load is applied, whereas HR590DP tends to concentrate stress at the martensite-ferrite interface. The more uniform stress distribution allows strain to be accommodated over a larger volume and requires a larger stress to unpin dislocations, which is made more difficult by the presence of precipitates. The concentrated stress along with the lack of precipitates in HR590DP causes deformation to be accommodated by the creation of fresh mobile dislocations in ferrite to accommodate strain at the interface. The generation of mobile dislocations and the subsequent pinning promotes work hardening in the ferrite, which is evident by the higher work hardening exponent. The dislocation

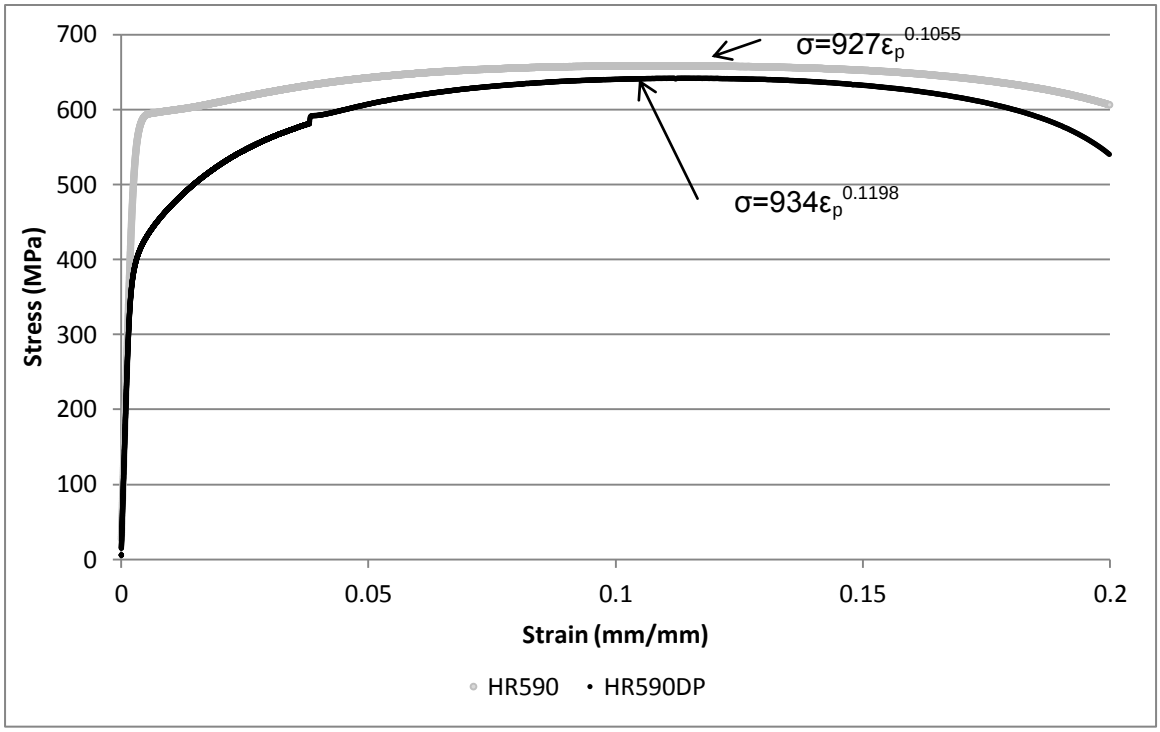

Figure 15: Monotonic stress-strain response for HR590 and HR590DP with parameters from Eq.1 (Holloman Eq.) included for reference

behavior in the dual phase steel provides more ductility, but a lower yield point. Comparatively the total uniform elongation of HR590 is 22% with and yield point of 570MPa versus 26% for HR590DP with a yield point of 420MPa. The implications on the fatigue behavior are discussed in Section 4.2.

4.3 Cyclic Properties of HR590 and HR590DP Steel

Low cycle testing[(34)] is performed to assess the fatigue behavior of a material in the plastic strain regime. This section provides results from low cycle fatigue experiments performed on HR590 and HR590DP and analyzes the response to cyclic loading in the plastic deformation regime.

4.3.1 Hysteresis Loops

Steel subjected to cyclic loading in the plastic deformation regime has a non-linear stress-strain response. When stress and strain are plotted together, the non-linear response forms a hysteresis loop for each loading cycle. Representative hysteresis loops for specimen HR590 at 0.2%, 1.1% and 2.0% strain amplitude are shown in Figure 16**,** Figure 17 and Figure 18, respectively. The hysteresis loops for specimen HR590DP at 0.2%, 1.1% and 2.0% strain amplitude are shown in Figure 19, Figure 20 and Figure 21, respectively. Hysteresis loops for all specimens are shown in Appendix A.

The experimental specimens were initially loaded in tension and as such there is a monotonic portion that extends from the origin to the upper right corner of the hysteresis loop. The elastic portion was assumed to be in the range of 0-70 MPa. Some plasticity is expected near the yield strength of both steels, therefore using a lower range to calculate the modulus of elasticity minimizes the effect of any plasticity. The average initial modulus of elasticity for HR590 is 210GPa. The average initial modulus of elasticity for HR590DP is 208GPa. After the initial tensile load, changes in modulus of elasticity were calculated using the unloading portion after the full tensile strain was applied. These changes are shown alongside the hysteresis loops in Appendix A. HR590 showed a decrease in modulus of elasticity at high strain amplitudes and an increase at lower strain amplitudes. HR590DP showed an initial increase in modulus of elasticity at all strain amplitudes followed by a decrease at longer life. The mechanism for this change in modulus is discussed in Section 4.3.2, in respect to the hardening/softening behavior.

For analyzing fatigue data at a specific fatigue life, the hysteresis loops are required to be relatively stable, although small changes are expected to occur. It is expected that the flow stress will change to account for variations in plastic deformation.

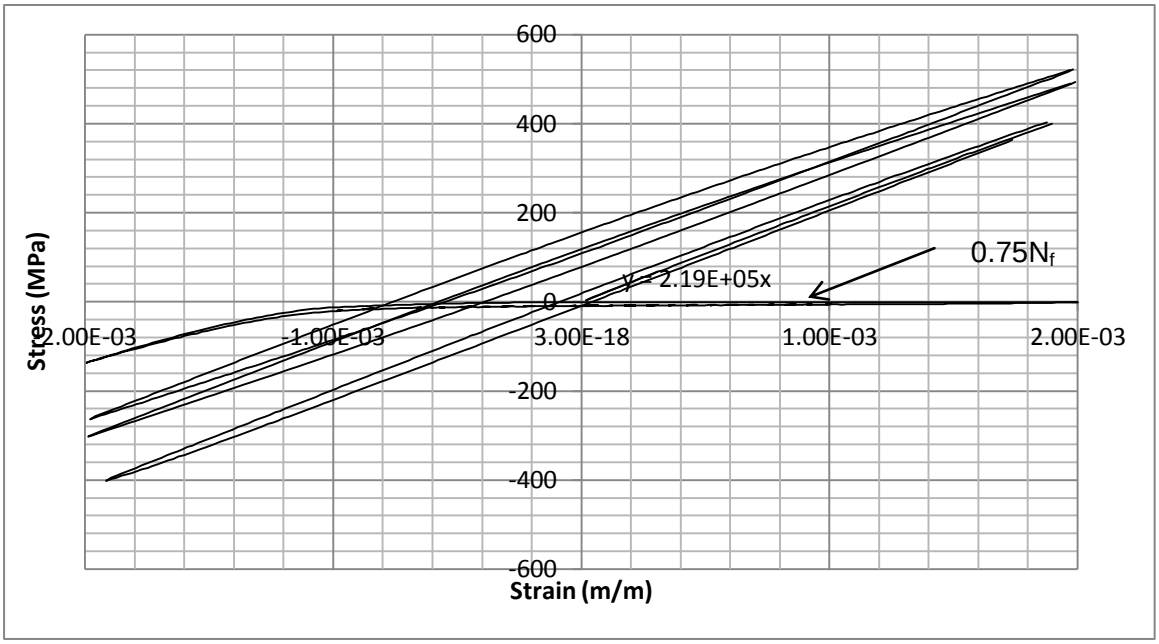

Figure 16: HR590 hysteresis loops for $0N_f$, $0.25N_f$, $0.5N_f$, $0.75N_f$ fatigue life cycles evaluated at 0.2% strain amplitude. Fatigue life (N_f) for this specimen is 102048 cycles

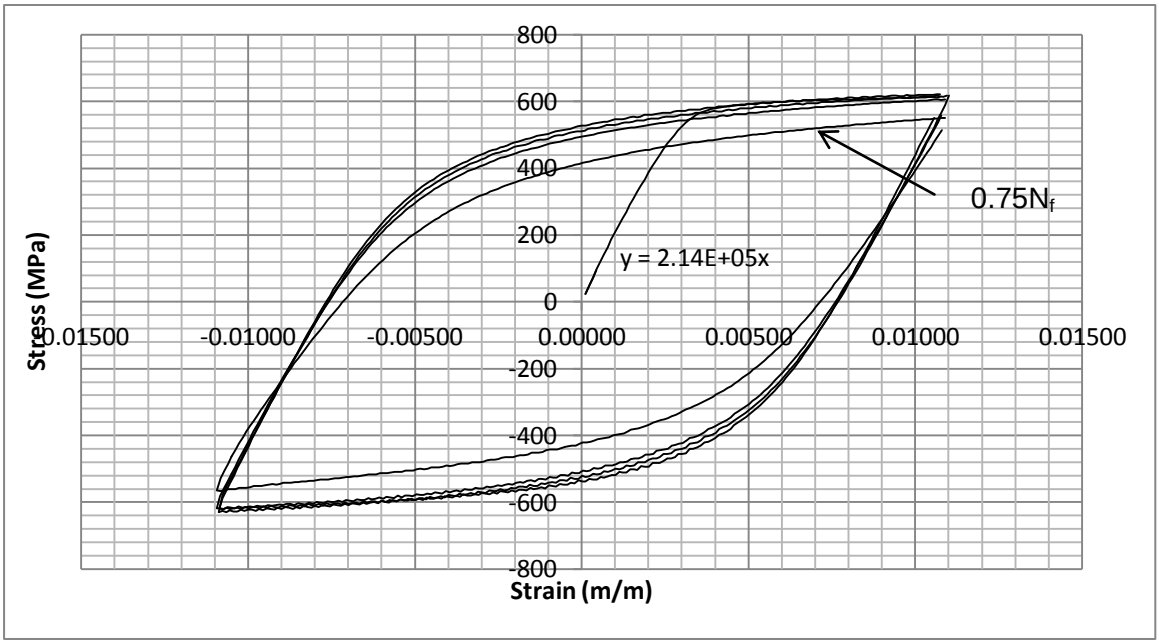

Figure 17: HR590 hysteresis loops for $0N_f$, $0.25N_f$, $0.5N_f$, $0.75N_f$ fatigue life cycles evaluated at 1.1% strain amplitude. Fatigue life (N_f) for this specimen is 474 cycles

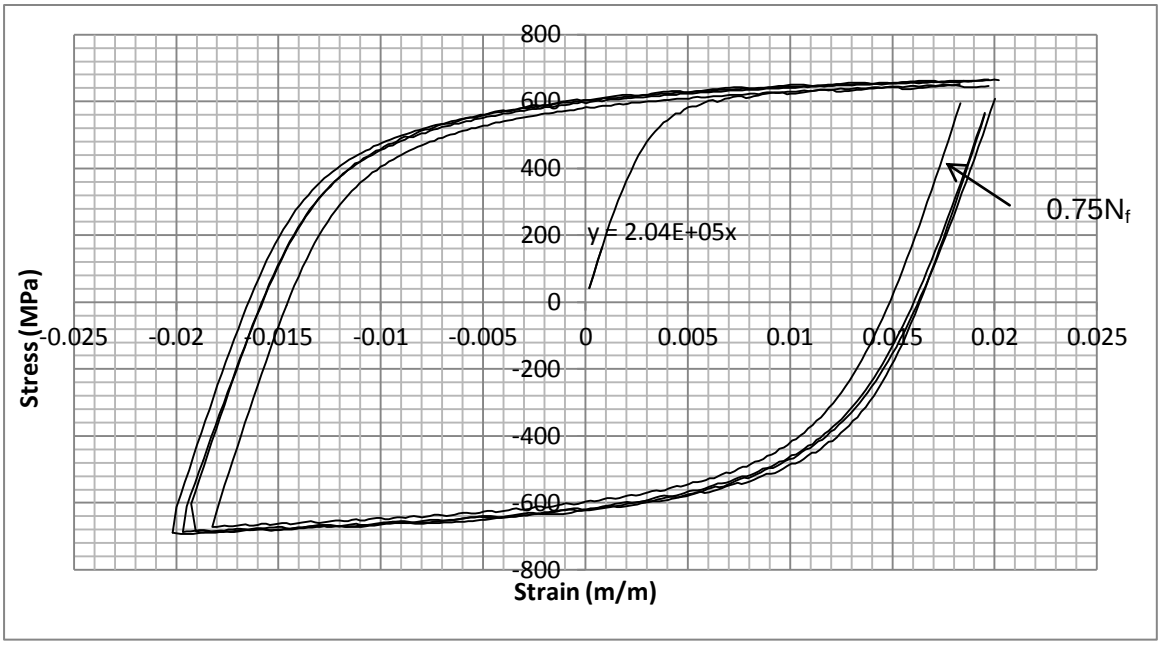

Figure 18: HR590 hysteresis loops for $0N_f$, $0.25N_f$, $0.5N_f$, $0.75N_f$ fatigue life cycles evaluated at 2.0% strain amplitude. Fatigue life (N_f) for this specimen is 100 cycles

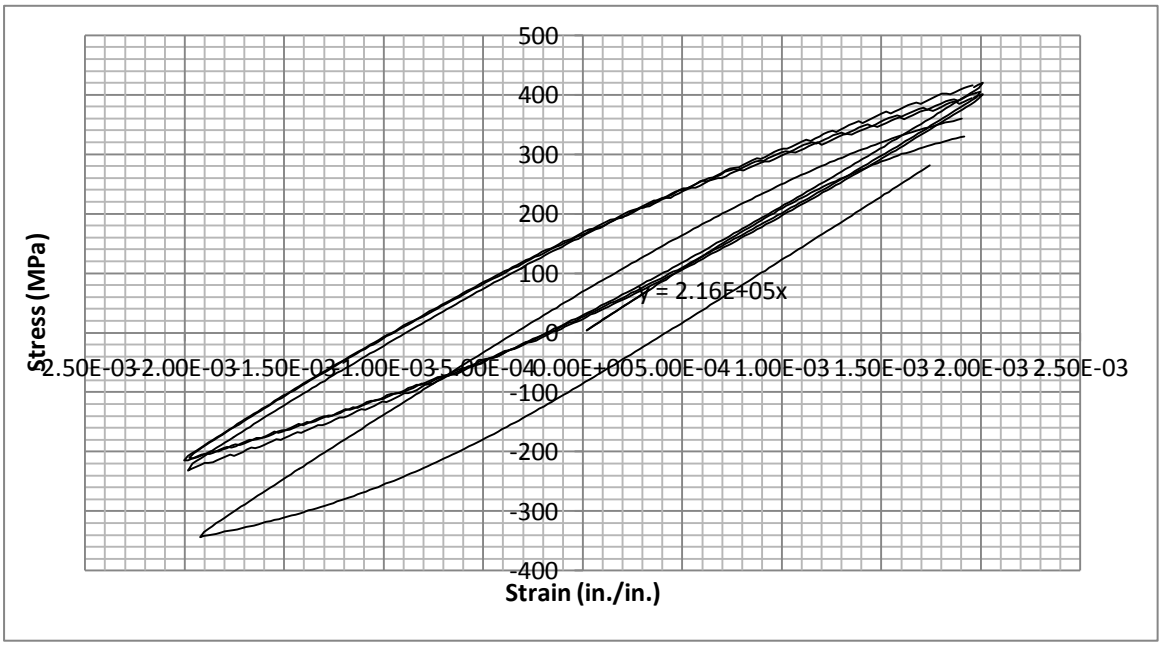

Figure 19: HR590DP hysteresis loops for $0N_f$, $0.25N_f$, $0.5N_f$, $0.75N_f$ fatigue life cycles evaluated at 0.2% strain amplitude. Fatigue life (N_f) for this specimen is 58546 cycles

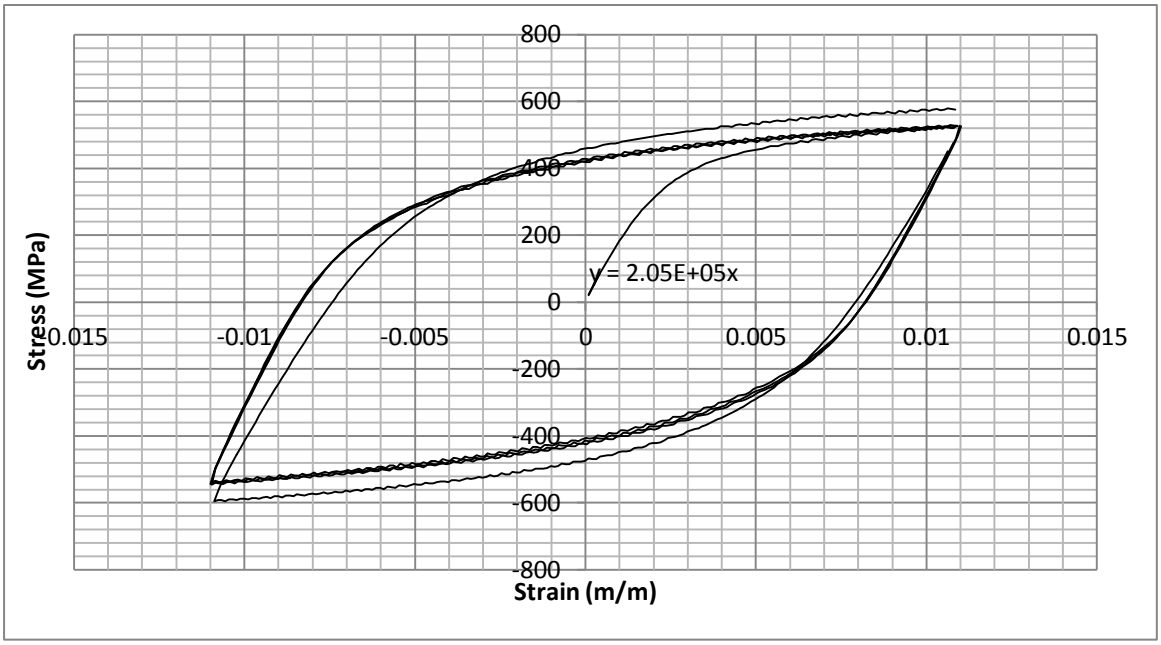

Figure 20: HR590DP hysteresis loops for $0N_f$, $0.25N_f$, $0.5N_f$, $0.75N_f$ fatigue life cycles evaluated at 1.1% strain amplitude. Fatigue life (N_f) for this specimen is 656 cycles

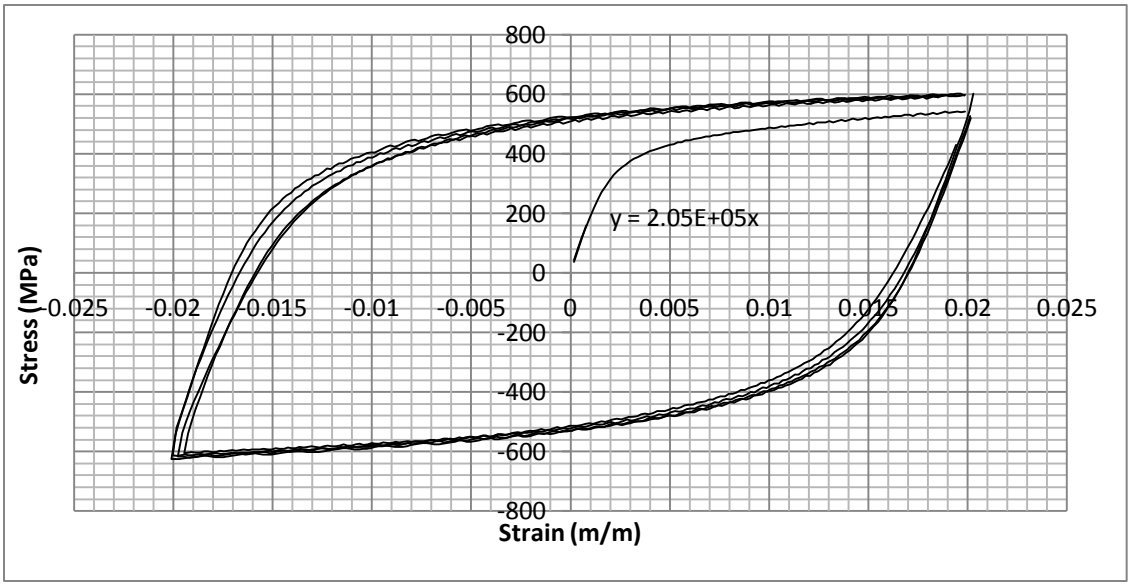

Figure 21: HR590DP hysteresis loops for 0, 0.25, 0.5, 0.75 fatigue life cycles evaluated at 2.0% strain amplitude. Fatigue life (N_f) for this specimen is 116 cycles

The hysteresis loops for both steels stabilize near $0.25N_f$ (¼ of the fatigue life). The loops remain relatively stable through $0.75N_f$. This is comparable to most materials, which show fatigue stability at half-life. The half life data for all specimens is shown in Appendix B. A notable instability exists at the lowest strain amplitudes resulting in higher tensile flow stress (i.e. the hysteresis loop moves up), caused by relaxation of a residual tensile stress during cyclic loading. The rate at which the relaxation occurs is dependent on the strain amplitude; therefore at smaller strain amplitudes the relaxation effects are more gradual. The residual stresses may be present from transformation kinetics, thermal gradients during cooling, mechanical treatments, etc. During the fatigue tests, the load was offset to account for this behavior near 20,000 cycles and 100,000 cycles, only if the load did not stabilize. This behavior was only observed at 0.2% strain amplitude. At all other strain amplitudes the residual stresses were eliminated within the first few cycles, so that the hysteresis loops are minimally affected.

4.3.2 Cyclic Stress Response

The mean stress amplitude vs. accumulated strain is shown in Figure 22 and Figure 23, for HR590 and HR590DP respectively. Mean stress amplitude is defined as

$$\frac{\sigma_{max}-\sigma_{min}}{2} \qquad \textbf{Eq. 4}$$

while accumulated strain is a function of the number of cycles and the strain amplitude. Near the end of the fatigue life a crack initiates and propagates through the microstructure and thereby alters the mean stress amplitude. During a strain controlled test, the crack changes the cross-sectional area and causes a load drop leading to the sudden decrease in slope observed near the end of the fatigue life. The data of interest is prior to the sharp decrease in slope and shows mean stress values unaffected by fracture allowing the quantification of hardening/softening behavior.

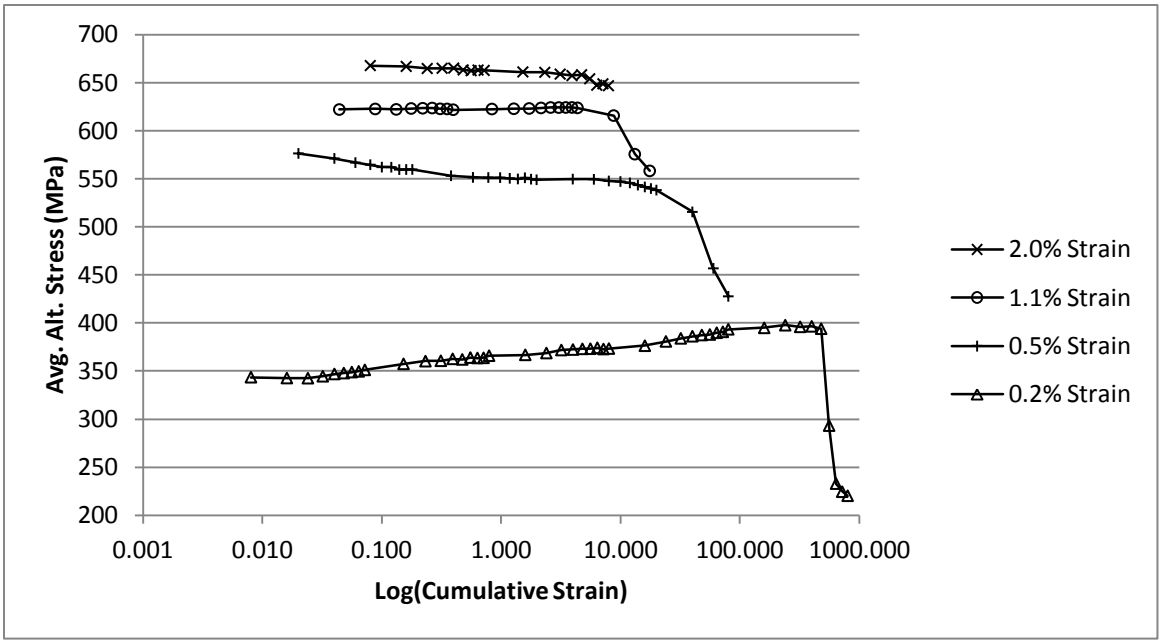

Figure 22: Average alternating stress as a function of the total accumulated strain on the HR 590 specimen taken at four representative strain levels

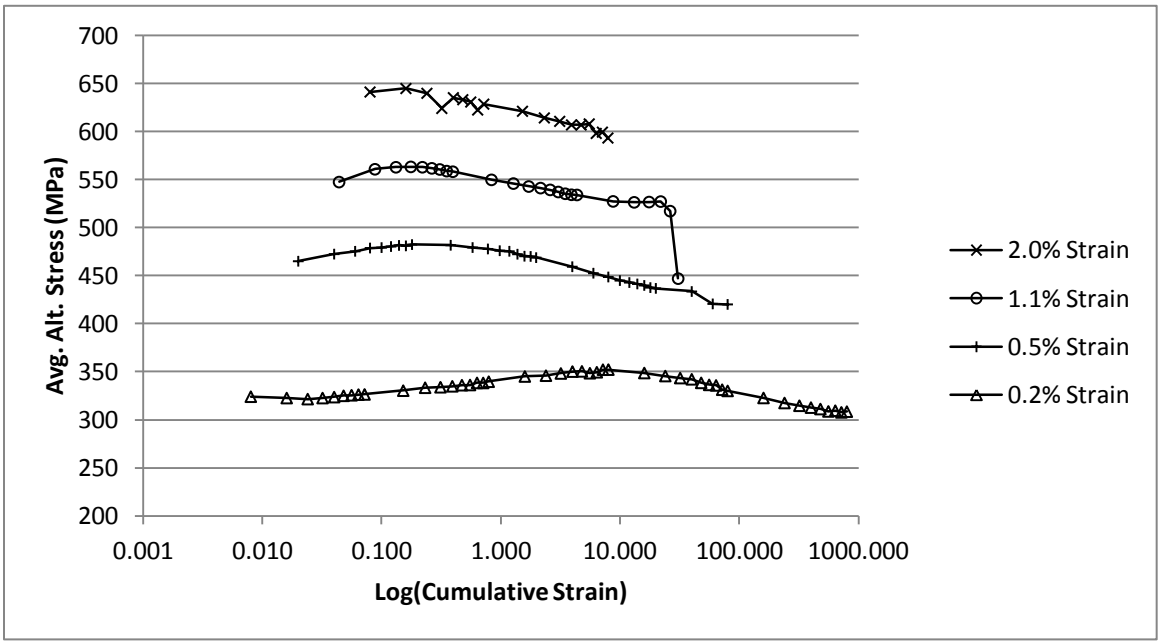

Figure 23: Average alternating stress as a function of the total accumulated strain on the HR590DP specimen taken at four representative strain levels

HR590 specimens showed little to no change in the stress response at high strain amplitudes, but both hardening and softening was observed at lower strain amplitudes. Hardening was observed at 0.2% strain amplitude and softening was observed at the next experimental strain amplitude, 0.5%. This trend is observed in other HSLA steels and attributed the dislocation mobility within the grains and expansion of plastic deformation throughout the gauge section.[18] [35] At the lowest strain amplitude tested, 0.2%, the cyclic mean stress amplitude is below the reported yield stress (Reported as σ_y=570 MPa for HR590); however microyielding is occurring due to localized plastic deformation in grains having a favorable crystallographic orientation with the loading direction. To accommodate deformation caused by microyielding, dislocation motion is occurring in these localized regions. This dislocation motion differs from that associated with the monotonic response because the stresses are both tensile and compressive during fatigue testing. Therefore, the dislocations move back and forth allowing for dislocation reactions that lower the overall energy of the grain structure. These reactions result in an ordered dislocation substructure that hardens the ferrite grains. As the first few grains harden, more of the strain is accommodated by softer adjacent ferrite grains. As is evident by the mean stress response, some of these adjacent grains are plastically deformed leading to the continued hardening, at 0.2% strain amplitude, until failure. Within the grains that dislocation motion is occurring, precipitates, such as those found in HR590, provide resistance to dislocation motion and pin dislocations until enough strain energy is provided by the applied load to move the dislocation past the precipitate. This strain energy is typically associated with the yield strength of the material. As shown by the stress response of HR590 at 0.5% strain amplitude the mean stress amplitude is near the yield strength of the material, allowing dislocations to be unpinned from precipitates. Additionally, because the stress is higher more grains are plastically deformed during testing. The softening behavior observed in

HR590 at 0.5% strain amplitude is attributed to the increase in dislocation mobility facilitated by the generation of new dislocations over a larger volume and the unpinning of dislocations from precipitates. Therefore, at strain amplitudes slight below the yield strength of the material softening was observed due to the lack of dislocation substructures. As the strain amplitude is increased, deformation continues to spread throughout the gauge section of the specimen. This allows the formation of the dislocation substructure in many of the grains, however the effects at high strain amplitudes in HR590 are offset by the grains in which the substructure is not formed. The cumulative effect of the applied strain shows little to no hardening/softening response at strain amplitudes of 1.1% and 2.0%. Therefore, fatigue behavior is dependent on strain amplitude leading to the mixed response observed in HR590.

HR590DP specimens exhibited varying degrees of work hardening followed by softening leading to failure. The work hardening behavior occurs at all strain amplitudes, with a more gradual work hardening occurring over a greater range at 0.2% strain amplitude. The work-hardening is the result of an increase in dislocation density resulting from plastic deformation. For dual phase steels, plastic deformation in the ferrite phase occurs at a different rate than the harder martensite phase. The difference in deformation concentrates stress at the interface resulting in the generation of dislocations to accommodate slip. HR590DP has a negligible addition of alloying elements that form precipitates; therefore dislocation mobility in ferrite is only restricted by the orientation of the slip planes with the loading direction. This allows the dislocations to form a dense substructure at the interface that becomes less dense away from the interface. This substructure hardens the ferrite during cyclic loading and forces the martensite to accommodate more strain. As more strain is accommodated by martensite the matrix will soften. This can be attributed to the unpinning of dislocations

and the formation of lower energy dislocation configurations. Therefore, the rate of hardening is attributed to the hardening of the ferrite and softening is attributed to the softening of the martensite. The cumulative effect is shown by the mean stress amplitude response of the steel.

Compared to HR590, there is little or no change in the HR590DP steel behavior near or beyond the yield stress (Reported as σ_y= 420MPa), except for a different rate of hardening due to changes in strain amplitude. Therefore, although both steels have the same tensile strength grade (590 MPa), the effect of accumulated strain is different. The HR590 exhibits a mixed behavior that is dependent upon the strain amplitude, while the HR590DP exhibits a mixed behavior that is independent of strain amplitude.

For dual phase steels, Zhongguang et. al.[19] showed that the cyclic response is dependent on the martensite content. For axially loaded, plastic strain controlled fatigue tests, specimens with 0.05wt.%C and 19% martensite volume fraction showed a dependence on strain amplitude, similar to HR590. This dependence was manifested in the form of hardening at low strain amplitudes, between 0.075% and 0.35%, but with variations in the rate. The same steel chemistry with 50% martensite volume fraction showed a smaller dependence on strain amplitude, similar to HR590DP. The difference in fatigue behavior was attributed to the strain compatibility between the martensite and ferrite phases. The lower martensite volume fraction dual phase steel accommodates nearly all strain in the ferrite grains. The higher martensite dual phase steel shows an increased amount of strain accommodated by martensite. This was shown by the dislocation substructure, prior to and after cyclic loading, which started as non-uniform “tangles” that became ordered substructures with accumulated strain.

4.3.3 Fatigue Stress-Strain Response

The monotonic stress vs. plastic strain curve with the cyclic stress vs. plastic strain curve is shown in Figure 24 and Figure 25, for HR590 and HR590DP respectively. The cyclic data is taken at half-life, representing the life where flow stress is relatively stable. The values for stress are the maximum (tension) stress values observed at half-life and the values for strain correspond to those maximum stress values. The values are corrected for plastic strain by using the modulus of elasticity at half-life (i.e. $\varepsilon_p = \varepsilon_T - \sigma/E$).

The cyclic response of HR590 shows softening at low strain amplitudes with a transition to hardening around 0.8% strain amplitude. The cyclic response of HR590DP is similar except that the transition happens at 0.3% strain amplitude. Comparison with data provided by other investigators shows that the stress-strain response is dependent on a variety of microstructural parameters. Mixed behavior has been shown to occur in many HSLA steels, due to the precipitation hardened ferrite microstructure that shows a stress response dependent on strain amplitude.[24] Keeping in mind that at half-life the ferrite microstructure of HR590 has accumulated more damage at high strain amplitudes and less at lower strain amplitudes, therefore any hardening resulting from increases in dislocation density are not realized at half life below 0.8% strain amplitude. The plastic deformation has generated fresh unpinned dislocations in the ferrite leading to softening. As the accumulated damage becomes greater, dislocation interactions may begin to harden the ferrite. However as shown in Section 4.3.2, substantial softening leads to failure around ~0.5% strain amplitude.

The morphology has been shown to impact the stress response of steels, particularly dual phase.[36] The volume fraction of martensite increases the yield strength of the dual phase microstructure, therefore preventing the onset of plastic deformation and improving the fatigue performance at low strain amplitudes. However, the increase

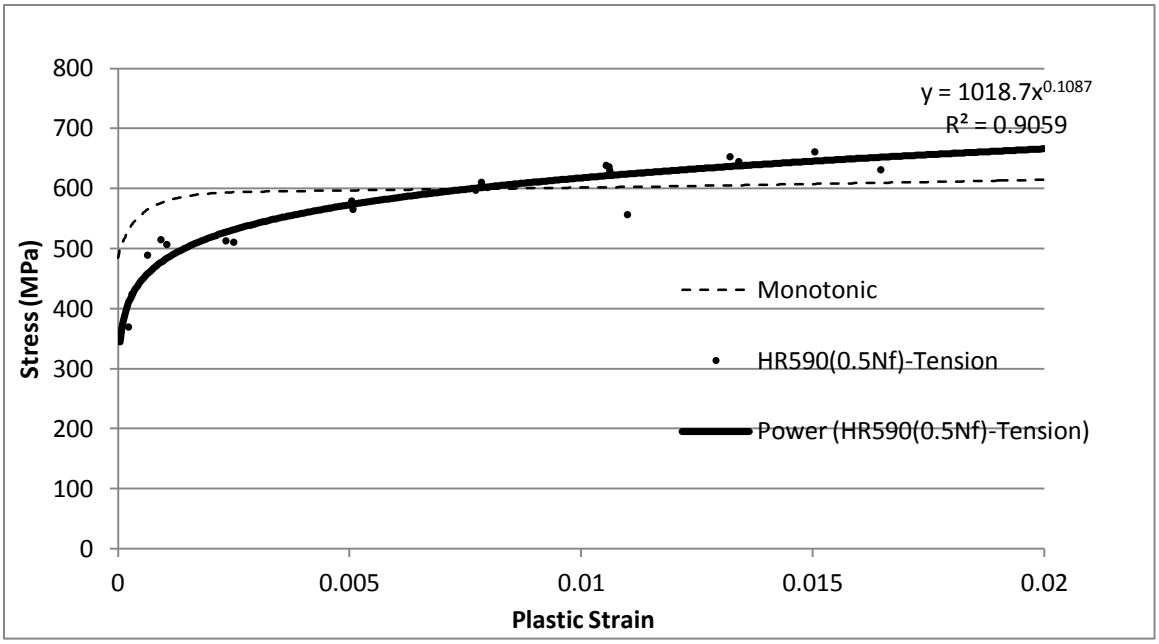

Figure 24: Cyclic and monotonic stress-plastic strain data for HR590 at half-life

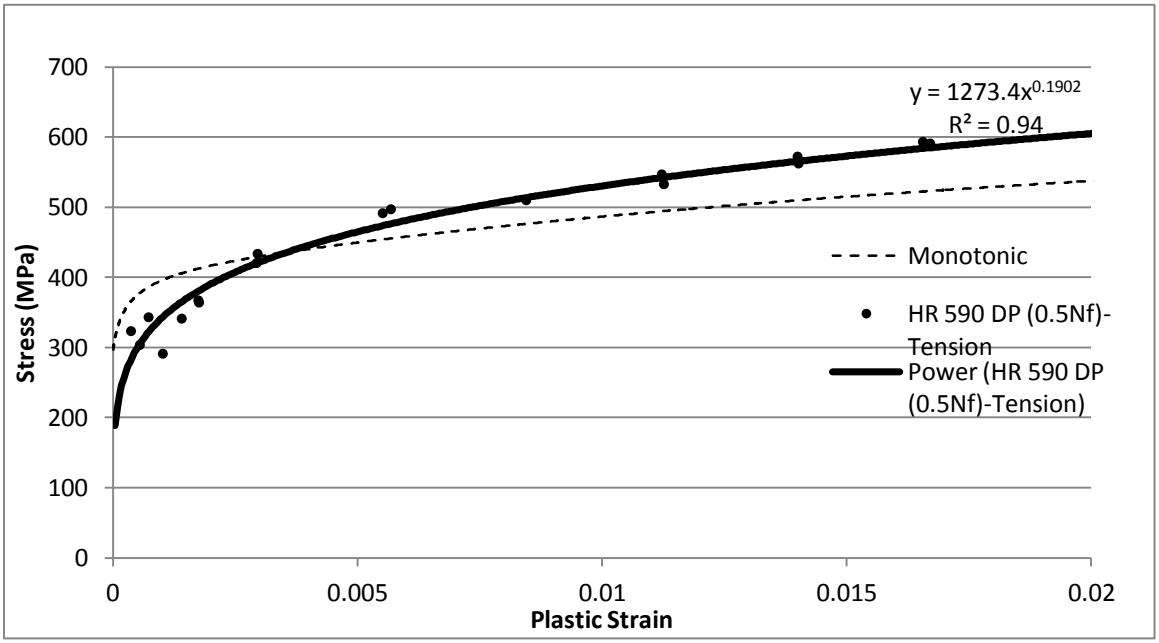

Figure 25: Cyclic and monotonic stress-plastic strain data for HR590DP at half-life

in martensite volume fraction lowers the ductility and is deleterious to the fatigue performance at high strain amplitudes.

Certain heat treatments that increase martensite volume fraction can lead to a more connectivity between adjacent martensite grains. Hu et. al. investigated the fatigue properties of a dual phase steel that showed a morphology with a more connected martensite phase that cyclically softened. Similar results were obtained by Mediratta et.al.[36] The connectivity allows the martensite to accommodate most of the strain, relative to ferrite, leading to a lower rate of work hardening.[37] The initially hard martensite phase tends to soften with increasing number of cycles.[22] Dual phase steels have also been shown to soften if most of the strain is accommodated by ferrite.[36] Softening may occur in dual phase steels where the ferrite grain size is large. Plastic deformation is highest at the martensite interface and gradually decreases away from the interface; therefore a larger ferrite grain allows deformation within the grain to happen over a larger length scale thus preventing the formation of a dislocation substructure. Mixed behavior, such as that found in HR590DP, has been observed in steels with heat treatments that produced fine, uniformly distributed martensite islands in a ferrite matrix[36] allowing for more uniform distribution of stresses in the microstructure. This allows a larger volume of the microstructure to accommodate the strain and more interfaces at which applied stress is concentrated. The fine ferrite in the dual phase microstructure reacts to accumulated damage similar to HR590, however the addition of martensite facilitates the hardening.

4.3.4 Fatigue-Life Response

It is useful for engineering design to try and predict the life of a component exposed to cyclical loading. In order to represent the life response it is necessary to divide the strain into an elastic component and a plastic component. For HR590 and

HR590DP the separated components are shown in Figure 26 and Figure 27 on a log-log plot. The associated 95% confidence intervals are also shown, as calculated in accordance with *ASTM E739-10 Standard Practice for Statistical Analysis of Linear or Linearized Stress-Life (S-N) and Strain-Life (ε-N) Fatigue Data.*[38] For long fatigue life, the elastic contribution will dominate the deformation mechanism. As fatigue life decreases the plastic contribution increases. The values for transition strain and transition life are shown in the Figures.

From the linearized best fit lines, a fatigue life curve can be constructed by summing the elastic and plastic components together in the form of Eq. 3. The graphical result of the equation is shown in Figure 30 and the parameters are quantified in Table 5. The HR590 and HR590DP steels are plotted together to highlight the differences in the fatigue properties over a range of several strain amplitudes. The fitted curves show that the response of HR590DP has a longer fatigue life for the strain amplitudes under consideration, but the actual data suggest that this is an artifact of the analysis model and in fact any differences between the two steels are negligible. This is further emphasized by establishing confidence intervals, as shown in Figure 29 and Figure 28. The lower confidence interval is nearly the same for both steels; therefore the fatigue life of the two steels is statistically similar. Although the upper limit of the confidence interval can be computed, it is of little consequence when designing a part from these materials. Similar low-cycle fatigue studies on dual phase and HSLA steels have been carried out showing the same behavior.[3][5][25]

The values in Table 5 show the parameters that define the fatigue behavior of the test specimens. Using the relationships outlined in Chapter 2 and expected life values the maximum plastic strain amplitude, elastic strain amplitude and stress amplitude can be calculated. Of particular interest in engineering design is the maximum stress

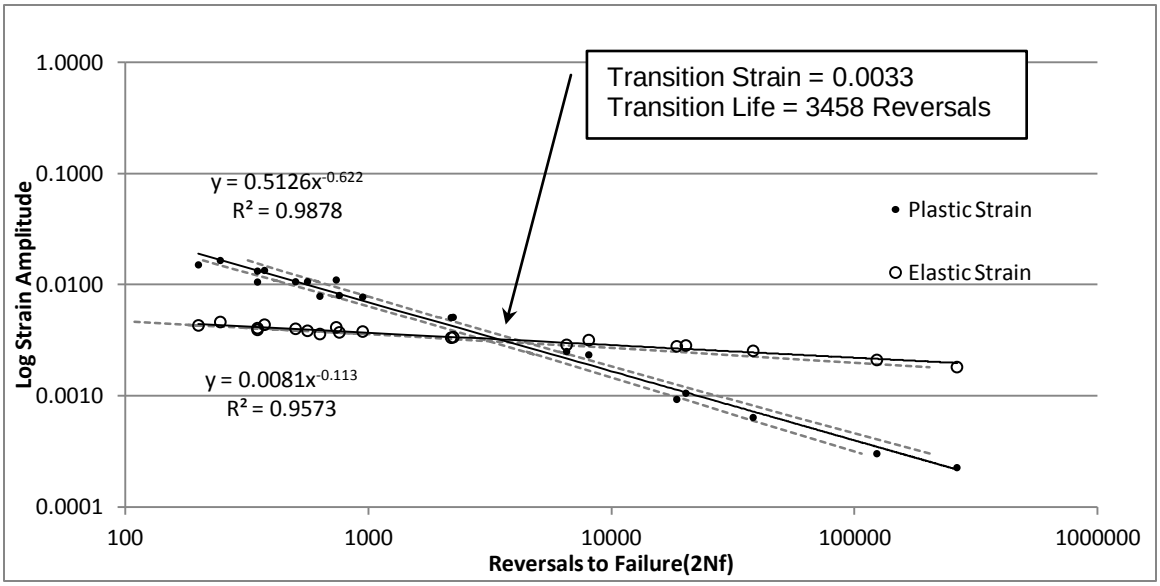

Figure 26: Elastic and plastic strain as a function of the number of reversals to failure for HR590. 95% confidence intervals are included as a dashed line for the elastic and plastic component individually.

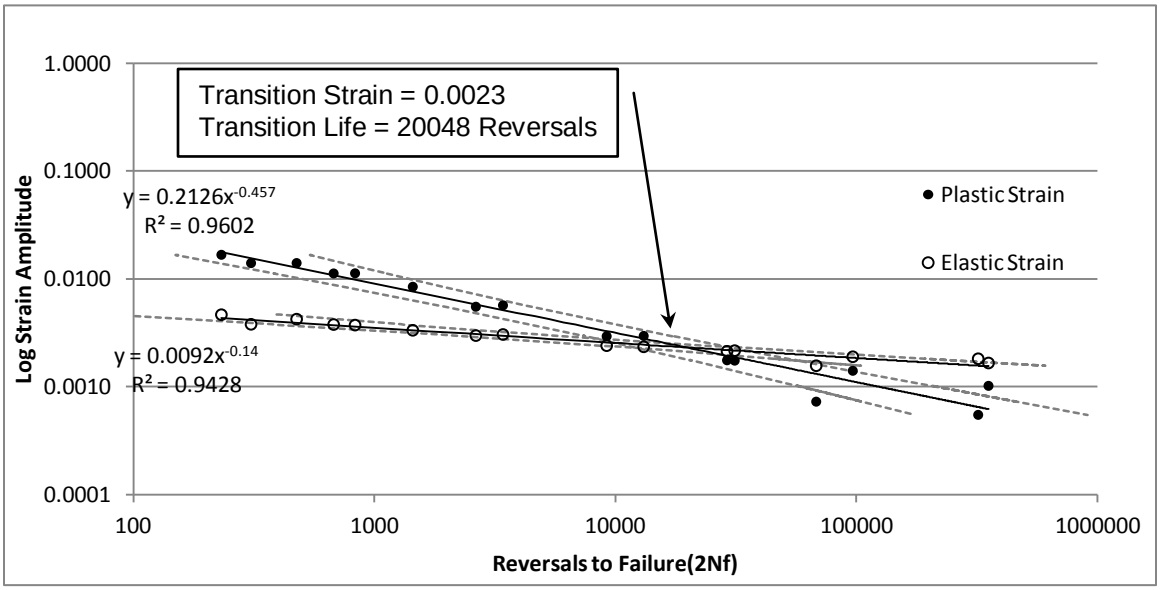

Figure 27: Elastic and plastic strain as a function of the number of reversals to failure for HR590DP. 95% confidence intervals are included as a dashed line for the elastic and plastic component individually.

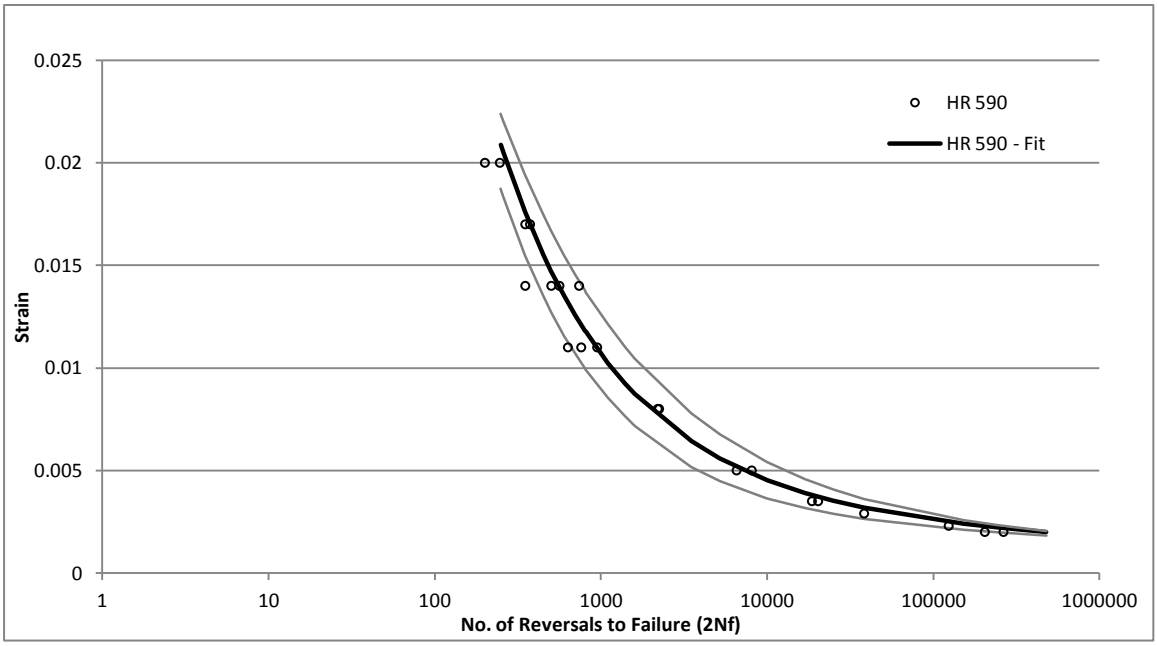

Figure 28: Strain-Life (ε-N) curve for HR590 with associated 95% confidence intervals

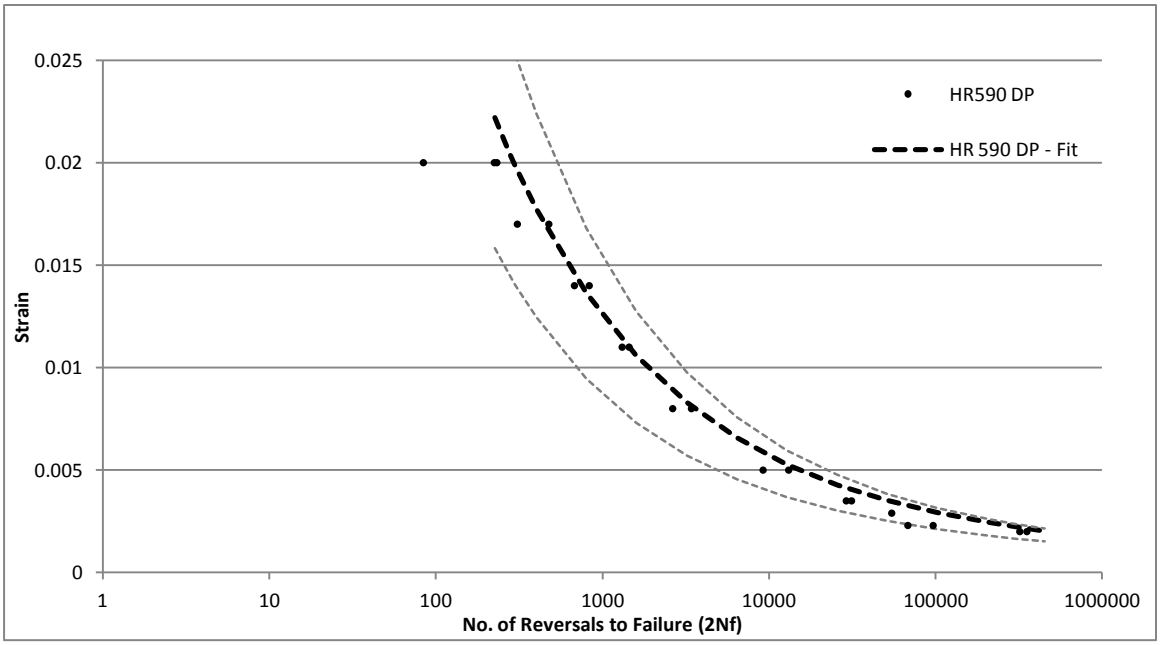

Figure 29: Strain-Life (ε-N) curve for HR590DP with associated 95% confidence intervals

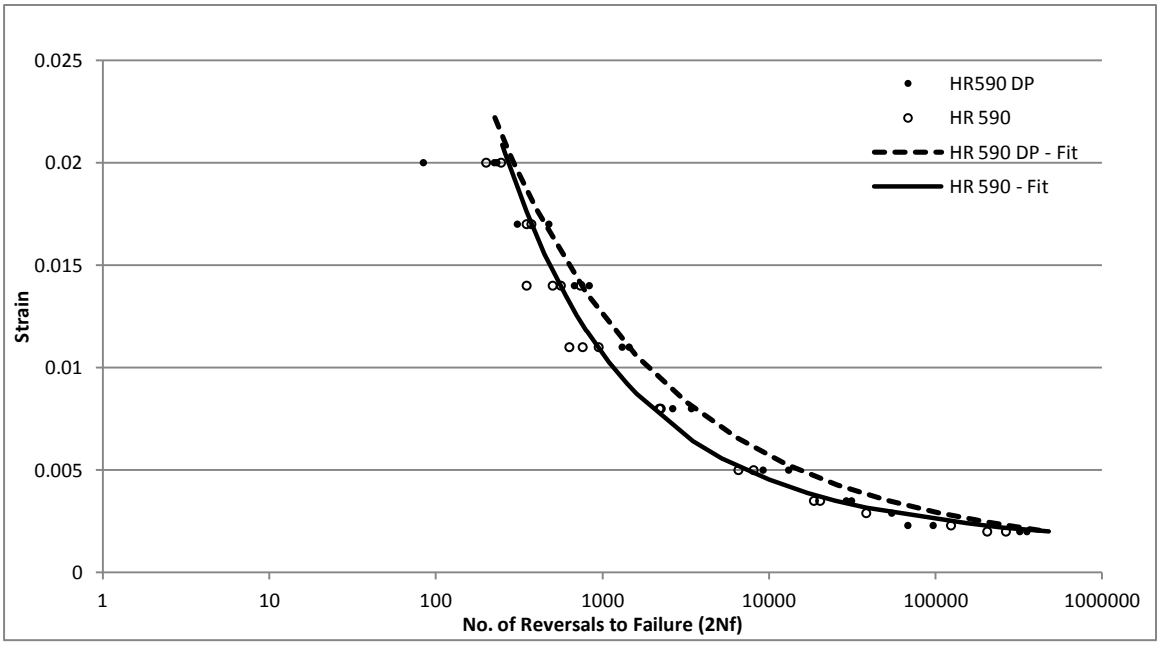

Figure 30: Strain-Life (ε-N) curve for HR590 and HR590DP with data points from fatigue tests

Table 5: Cyclic Mechanical Properties of HR 590 and HR 590 DP

	σ_f'	b	ε_f'	c	K´ (MPa)	n´
HR 590	1701	-0.113	0.5126	-0.622	1018	0.1087
HR 590DP	1914	-0.140	0.2126	-0.457	1273	0.1902

Table 6: Cyclic Stress for Strain Resistance (in MPa) for HR590 and HR590DP as calculated from the parameters in Table 5

Steel	**Life Level in Reversals**					
	500	**1000**	**5000**	**10000**	**50000**	**100000**
HR590	622	593	532	508	456	435
HR590DP	553	520	452	426	370	349

amplitude that can be sustained for a given life. This can be calculated by substituting the plastic strain-life equation into Eq.2 to yield the following,

$$\frac{\Delta\sigma}{2} = K'\left(\varepsilon_f'(2N_f)^c\right)^{n'} \qquad \textbf{Eq. 5}$$

The stress amplitude values for some life levels of interest are calculated from Eq. 5 and shown in Table 6. For the life levels calculated, the stress required for plastic deformation at the same life level is greater for HR590. Therefore, the differences in strain-life data are shown to be negligible in the steels investigated, but the stress-life data is more significant. Comparison between the two steels shows that HR590 required more force than HR590DP to achieve the same degree of strain. This can be attributed to the higher yield strength of HR590, which is resisting the onset of plastic deformation. Therefore, at the lower strain amplitudes a smaller component of plastic strain is contributing to the fatigue of HR590 and the accumulated damage needed for failure requires a larger number of cycles . As the expected life level increases from 500 to 100,000 reversals the difference in stress between the two steels increases from 69MPa to 86MPa. However, the influence of ductility on fatigue life should not be understated, as steels with low ductility are more sensitive to plastic deformation. This is shown by stress levels of HR590 becoming more comparable with HR590DP at lower life levels. Therefore, ductility in addition to yield strength is important for the fatigue performance of steel at all life levels and stress amplitudes. Service life could be significantly shortened by choosing steel that does not provide a good combination of ductility and strength. It should be emphasized that these results are for fatigue life within the low-cycle regime of smooth specimens and many practical applications require evaluation of the high-cycle regime, multi-directional loading, pre-straining (i.e forming) and notch effects.

4.4 Fractography of HR590 and HR590DP Steel

To locate the source of crack initiation the fracture surfaces were observed in the scanning electron microscope and optical stereomicroscope. Crack initiation is determined by tracing fan-like chevron marks back to a converging point(s) in the microstructure. This allows the analysis of the crack initiation area for any discontinuities causing failure. These observations are shown in the next sections along with a discussion.

4.4.1 Stereomicroscope Fractography

The stereomicroscope allows for qualitative analysis of the fracture surface at low magnifications. For specimens tested at various strain amplitudes, the fracture surfaces were characterized with regards to fracture profile and path. Figure 31 shows the fatigue fracture surfaces of HR590 at different strain amplitudes. Figure 32 shows the fatigue fracture surfaces of HR590DP at different strain amplitudes. The fracture surface is torturous at high strain amplitudes, showing that fast fracture dominated the failure mode. At lower strain amplitudes the profiles are less tortuous and the source of crack initiation can be more easily identified. Observation of HR590 and HR590DP fracture surfaces show the crack initiated at the hot-rolled surface and propagated. The low magnification images suggest that the rolled surface is an energetically favorable site for fatigue crack initiation; however a more detail analysis is required using the SEM for more information.

4.4.2 SEM Fractography

For a more detailed analysis of individual fracture surfaces, a SEM equipped with energy dispersive spectroscopy (EDS) was utilized. The SEM enables high magnification observations and the EDS yields local chemical analysis of the surface region of interest. Figure 33 shows different magnifications of the fatigue fracture surface from an HR590

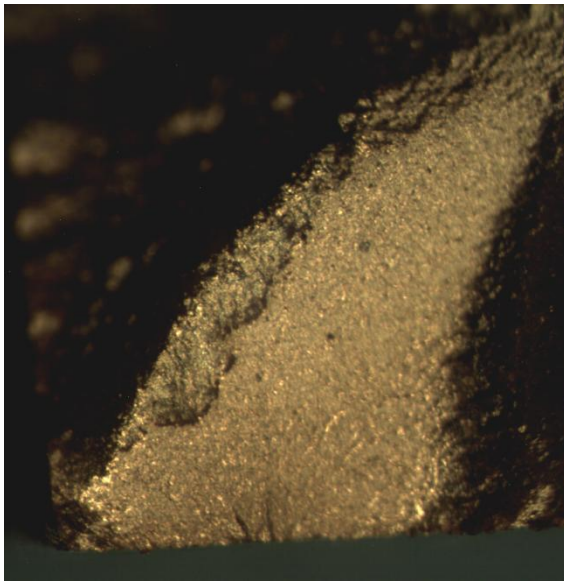

(a)

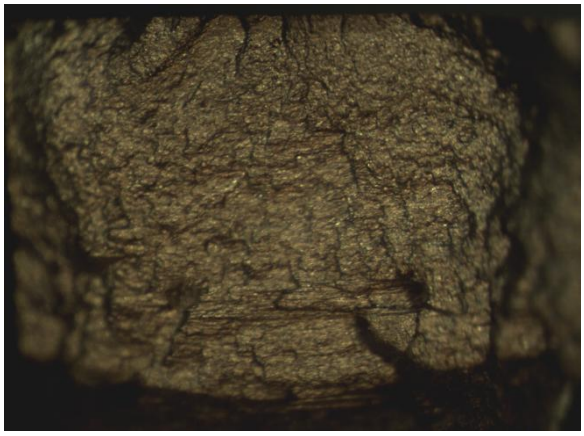

(b)

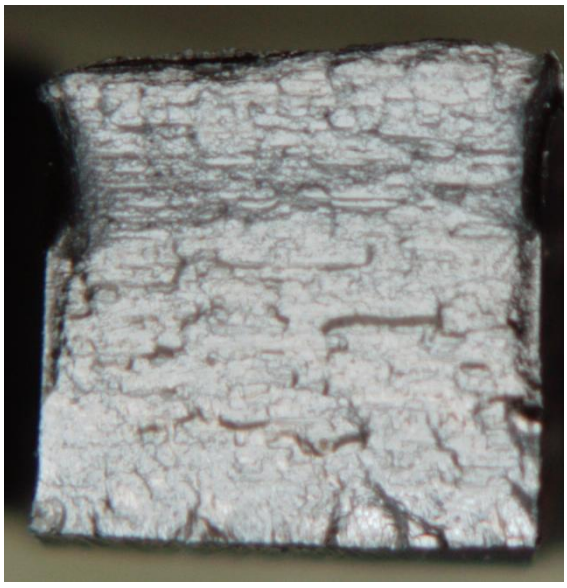

(c)

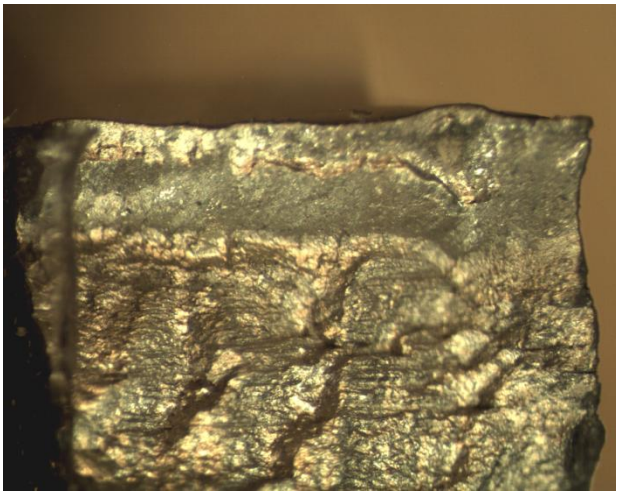

(d)

Figure 31: Fatigue fracture profiles of HR590 specimens taken at 40x magnification and tested at the following strain amplitudes a) 0.2% b) 0.5% c) 1.4% d) 1.7%

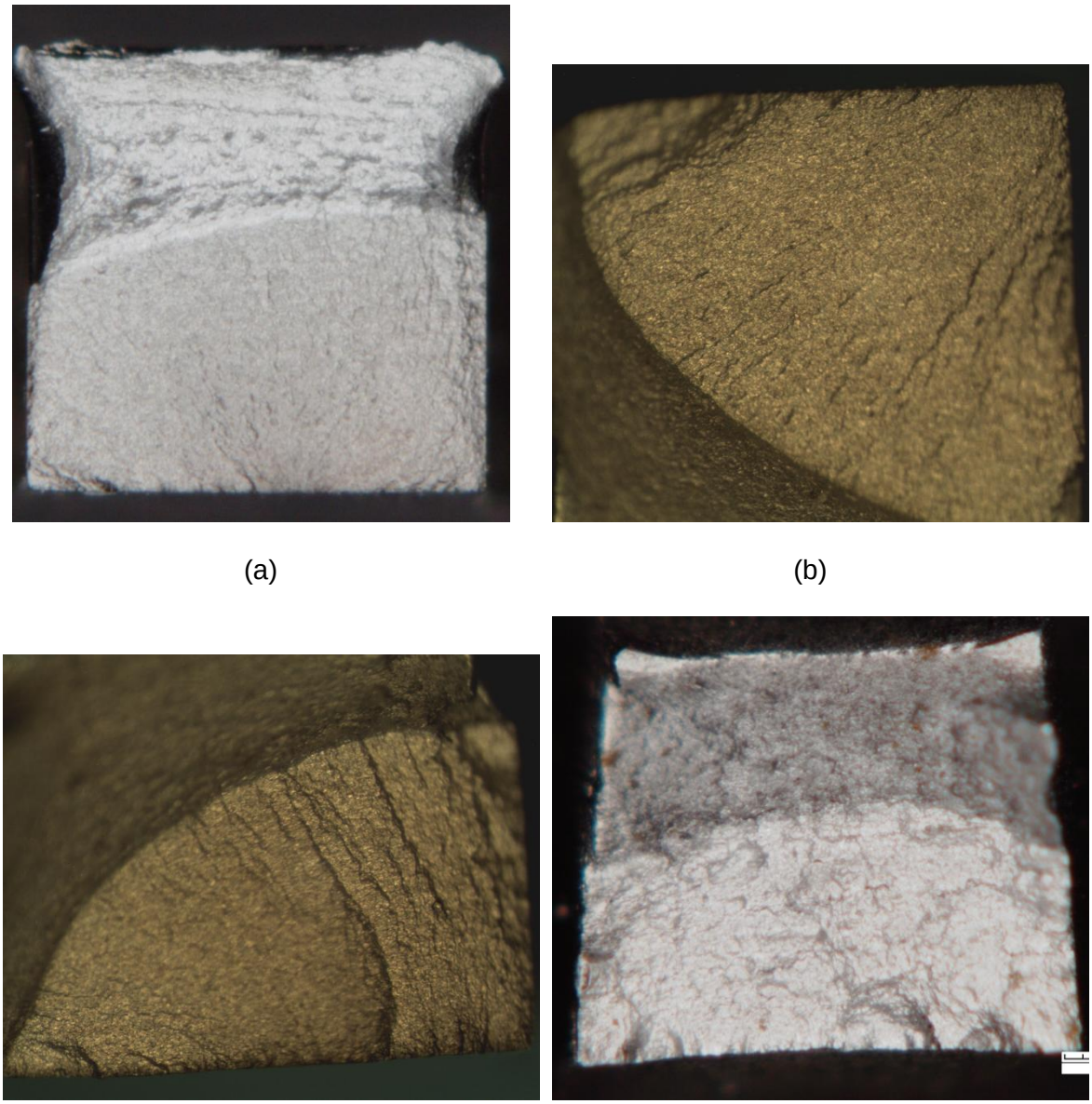

(a) (b)

(c) (d)

Figure 32: Fatigue fracture profiles of HR590DP specimens taken at 40x magnification and tested at the following strain amplitudes a) 0.2% b) 0.23% c) 0.35% d) 2.0%

specimen tested at 0.2% strain amplitude. Figure 34 shows different magnifications of the fatigue fracture surface from specimens of HR590DP tested at 0.2% strain amplitude. The SEM images give clear chevron lines back to the rolled surface where the crack initiated. At higher magnifications, HR590DP shows a more tortuous fracture surface at the point of crack initiation. This tortuous surface is defined by ridges that fan out from the initiation site. Comparatively, the HR590 steel shows no ridges going back to the initiation site, but instead depicts a smooth layered surface. This shows the microstructural features and mechanisms responsible for fatigue crack deflection operate at different length scales in the two steels. The smooth layered surface also shows spherical particles of which the exact composition is difficult to determine using EDS, but inclusions with high concentrations of Ca, Al, Si and O were found at various locations on the fracture surface of HR590. Similar compositions for inclusions were found in HR590DP.

A fatigue crack initiation site for HR590 is shown in Figure 35 from a specimen tested at 1.4% strain amplitude. From the SEM images it is shown that the rolled surface of the specimen adjacent to the crack initiation site is composed of striations in the oxide layer, which predominately run parallel to the loading direction. Perpendicular to the loading direction, micro-cracks are shown that separate the oxide layer. An inclusion near the surface on the order of ~50µm converges with a crack path, but is slightly removed from the crack initiation site. Observation of other crack initiation sites did not reveal the presence of inclusions with a similar length scale; therefore it is unlikely that the inclusion initiated the crack. It has been shown that crack initiation in high-strength low-alloy steels, such as HSLA occurs in persistent slip bands.[(39)(40)] However, persistent

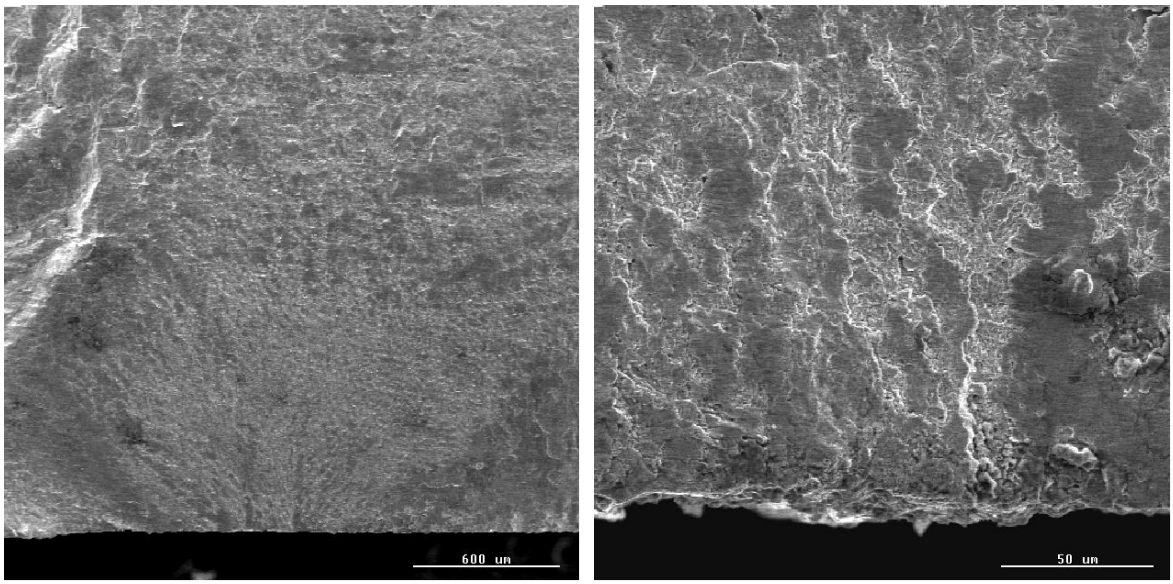

(a) (b)

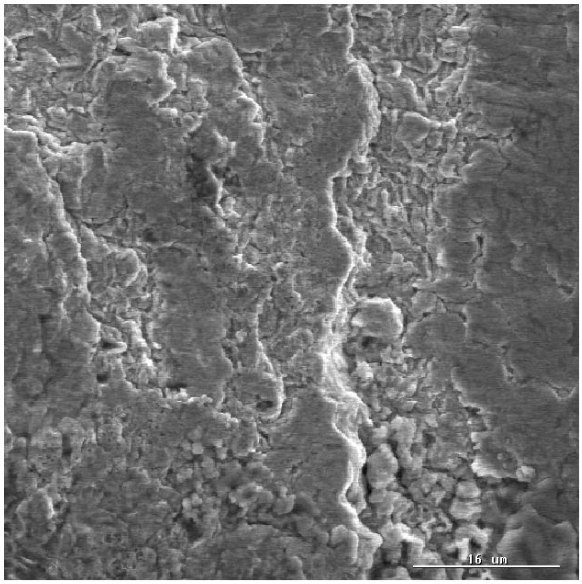

(c)

Figure 33: SEM Images of a HR590 fatigue specimen tested at 0.2% strain amplitude with failure at 102048 cycles a) fatigue fracture surface with lines fanning out from crack initiation site b) crack initiation site at 500x c) 1500x magnification image of fatigue fracture surface near crack initiation site

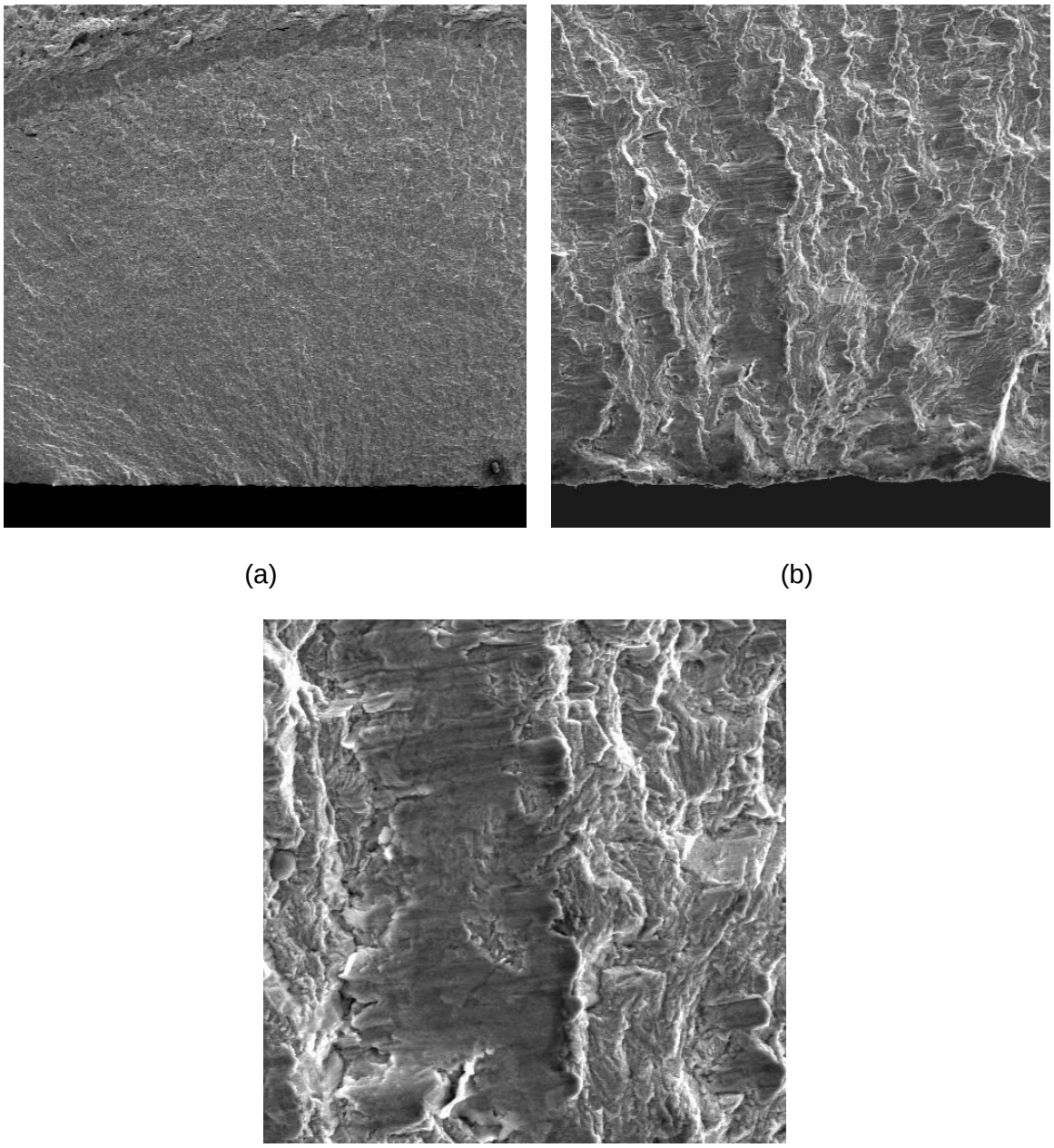

(a) (b)

(c)

Figure 34: SEM Images of a HR590DP fatigue specimen tested at 0.2% strain amplitude with failure at 160036 cycles a) fatigue fracture surface with lines fanning out from crack initiation site b) crack initiation site at 500x c) 1500x magnification image of fatigue fracture surface near crack initiation site.

slips can form at the machined surface, as well as the rolled surface. Observations made on several specimens did not show any indication of crack initiation at machined surface; therefore the rolled surface was favored.

A fatigue crack initiation site for HR590DP is shown in Figure 36 for a specimen tested at 2.0% strain amplitude. From the surface textures it is shown that there are two modes of fracture, ductile and brittle. Under applied loading, the dislocations in a dual phase microstructure pile up at the ferrite grain boundaries near the martensite interface. The accumulation of these dislocations leads to brittle cleavage type fractures in the ferrite grain, while the martensite grains exhibit a more ductile fracture.[36] Therefore, the work hardening mechanism exhibited by HR590DP contributed to crack initiation at the rolled surface. However, surface conditions due to hot roll processing favored the rolled surface of the specimen.

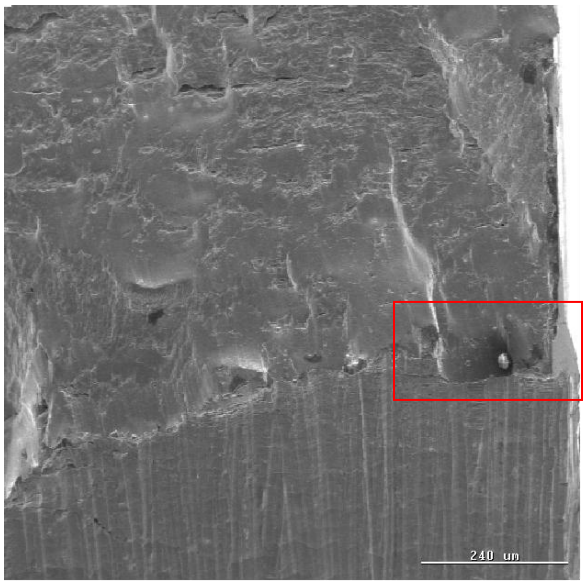

(a)

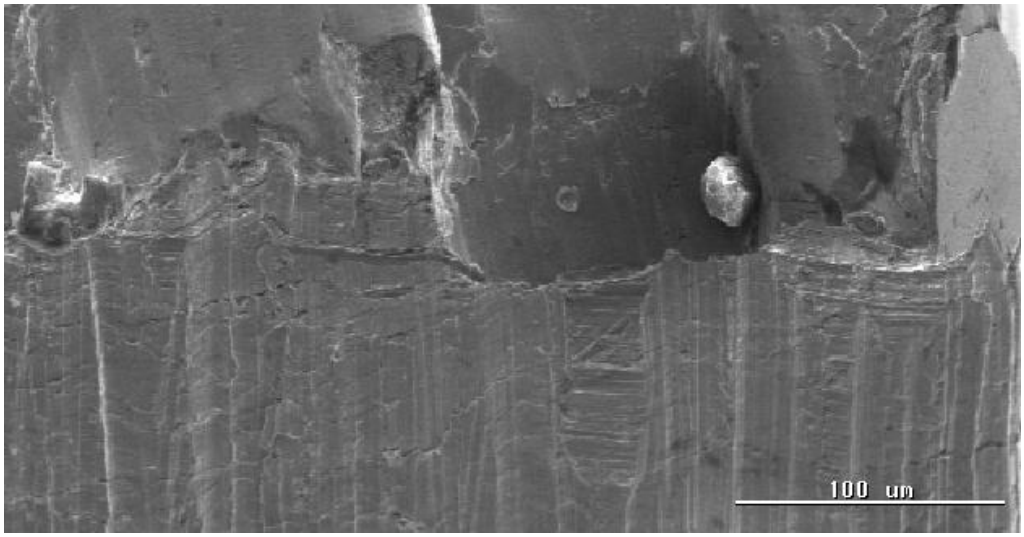

(b)

Figure 35: SEM images showing one crack initiation site in HR590 a) 100x b) 250x

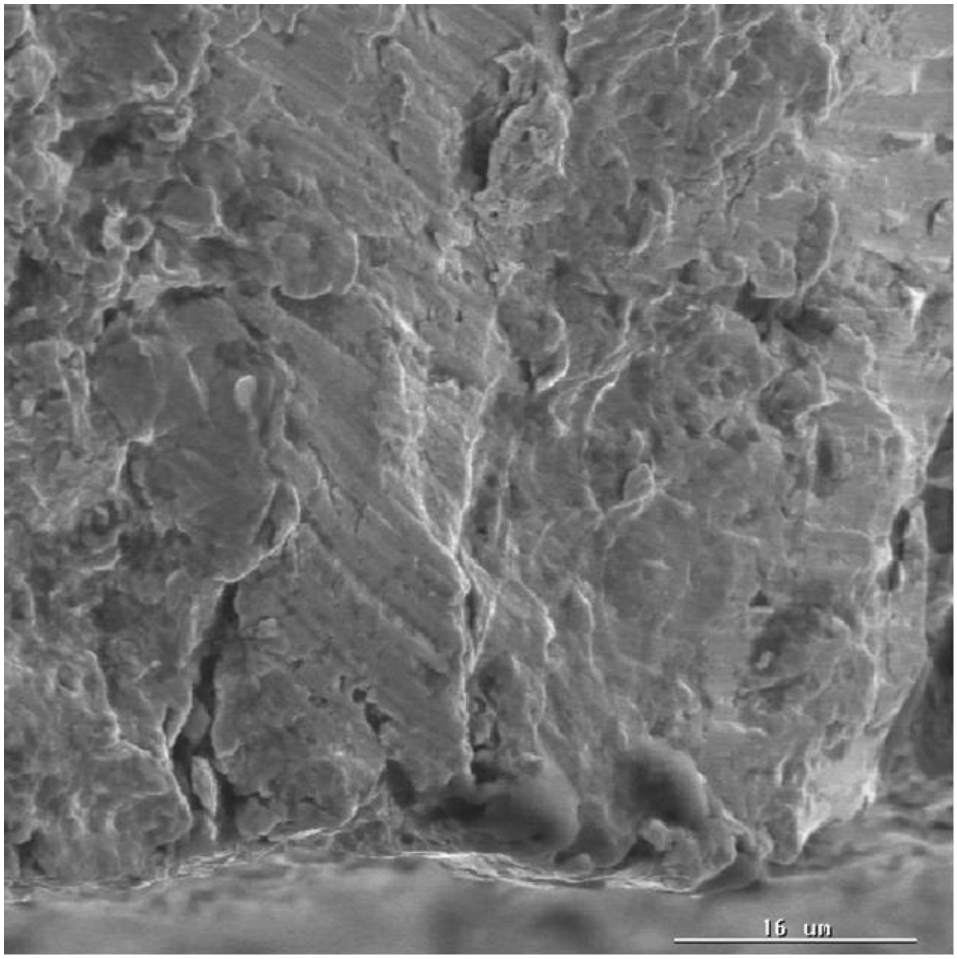

Figure 36: Crack initiation site in HR590DP showing an interface near the source of crack initiation. 1500x magnification.

Chapter 5: Summary and Conclusions

The steels of interest, HR590 and HR590DP, utilize different strengthening mechanisms to obtain the same tensile strength grade. The strengthening mechanisms are the result of specific processing parameters and chemical compositions. HR590 utilizes precipitation to harden the steel and refine the grain structure. HR590DP utilizes a martensitic transformation, which provides a hardened secondary phase and refines the grain structure. The microstructural observations, fracture observations, and fatigue relationships of HR590 and HR590DP are as follows:

- The microstructure of HR590 is entirely ferrite with some precipitates observed at the grain boundaries. The microstructure of HR590DP is mostly ferrite with some martensite and bainite dispersed in the matrix.
- Both steels have a Mn-rich region in the center of the specimen consistent with macrosegregation during casting. In HR590, the Mn-rich region is a pearlite band. In HR590DP, the Mn-rich region is a martensite band. In HR590DP the segregation led to hot cracking at the martensite-ferrite interface.
- HR590DP shows initial hardening followed by softening during fatigue testing at all strain amplitudes. In contrast, the fatigue response of HR590 does not change with the number of applied cycles, but with strain amplitude. HR590 generally hardens at low strain amplitudes, softens at intermediate strain amplitudes and is stable at high strain amplitudes.
- The cyclic stress-strain curves of HR590 and HR590DP show a mixed response at half life. At half life, the steels show softening at low levels of plastic strain and hardening at high levels of plastic strain.

- The strain-life data for the two steels is statistically similar within the low-cycle fatigue regime. However, a compilation of parameters from the half life fatigue data show that the HR590 has more resistance to applied strain than HR590DP.
- Observation of the fracture surface revealed that the rolled surface was the preferred crack initiation site for both steels.

The results of this research characterize and compare the fatigue behavior of two high strength steels. HR590 showed greater resistance to the onset of plastic deformation, especially at low strain amplitudes. At higher strain amplitudes the ductility of HR590DP became more important, but was still inadequate in providing resistance to strain.

Appendix A – Hysteresis Loops, Young's Moduli and Cyclic Stresses

Specimen No. 7-2a (HR590DP)
Specimen Gage Dimensions: 0.127"x0.127"
Failure @ 112 cycles @ 2.0% Strain

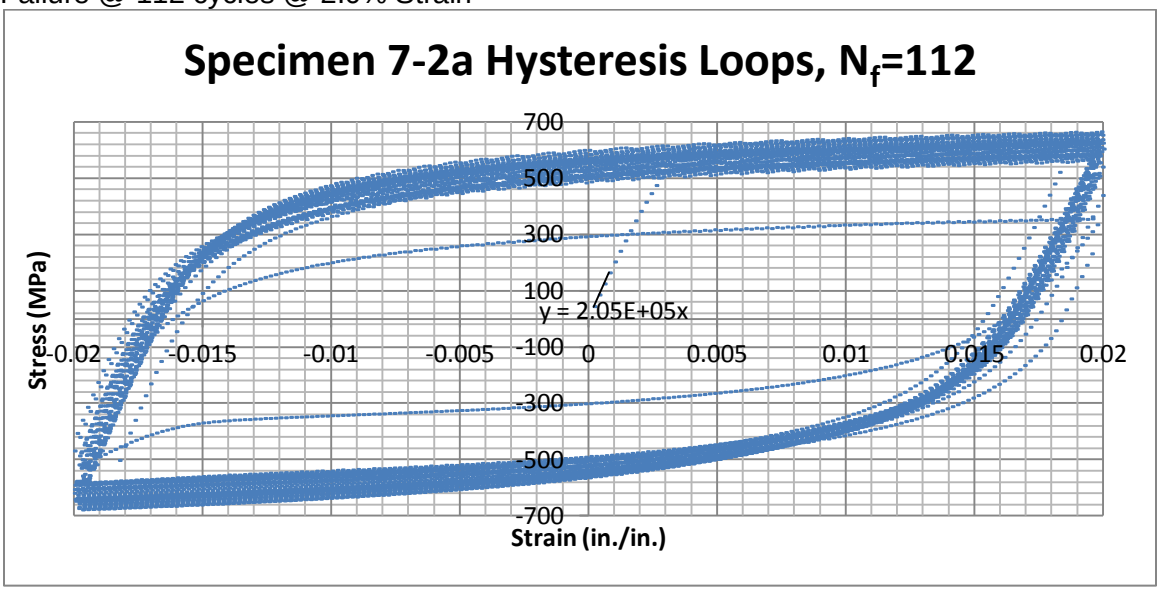

Young's Modulus per Cycle		
Cycle No.	**Compression Cycle (MPa)**	**Tension Cycle (MPa)**
1	1.80E+05	2.15E+05
2	1.79E+05	2.16E+05
3	1.82E+05	2.16E+05
4	1.82E+05	#DIV/0!
5	1.84E+05	2.20E+05
6	1.85E+05	2.22E+05
7	1.85E+05	2.21E+05
8	1.88E+05	2.21E+05
9	1.86E+05	2.23E+05
19	1.92E+05	2.23E+05
99	1.99E+05	2.41E+05

Max Stress per Cycle				
Cycle No.	**Max (MPa)**	**Min (MPa)**	**Mean Stress (MPa)**	**Alt. Stress (MPa)**
1	663	-679	671	-8
2	665	-678	671	-7
3	653	-674	664	-11
4	596	-670	633	-37
5	643	-666	654	-11
6	640	-663	652	-11
7	638	-659	649	-11
8	605	-658	632	-27
9	635	-654	644	-10
19	622	-639	631	-9
99	570	-585	578	-7

Specimen No. 7-3a (HR590DP)
Specimen Gage Dimensions: 0.127”x0.127”
Failure @ 116 cycles @ 2.0% Strain

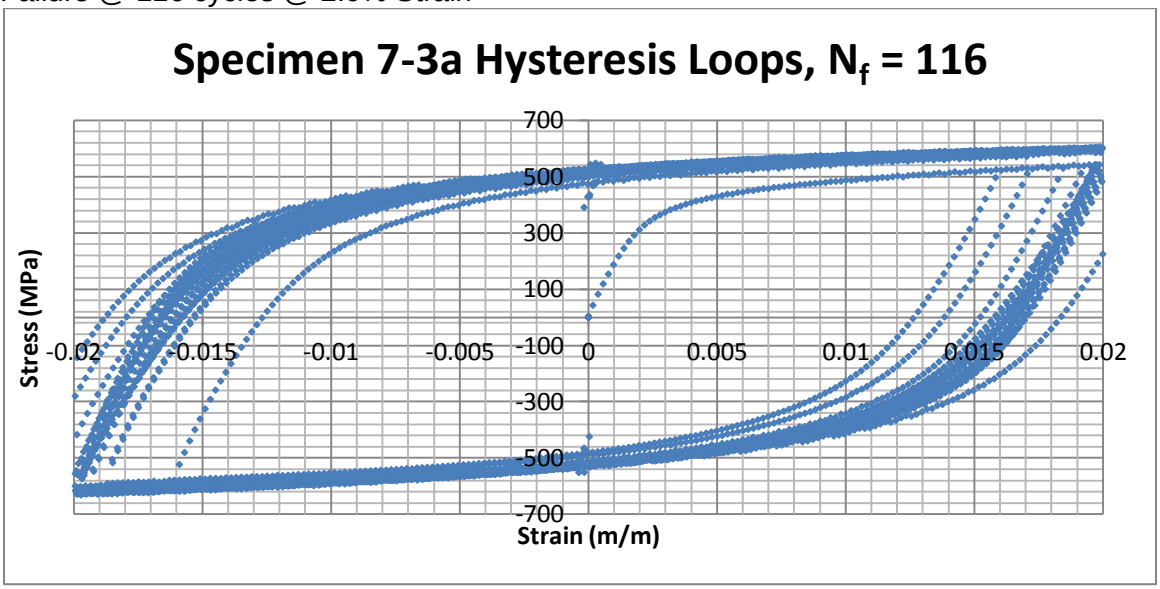

Young's Modulus per Cycle		
Cycle No.	**Compression Cycle (MPa)**	**Tension Cycle (MPa)**
1	1.67E+05	1.89E+05
2	1.82E+05	1.98E+05
3	1.89E+05	2.10E+05
4	1.95E+05	2.15E+05
5	1.90E+05	2.15E+05
6	1.92E+05	2.16E+05
7	1.99E+05	2.15E+05
8	1.96E+05	2.18E+05
9	1.97E+05	2.17E+05
19	1.95E+05	2.18E+05
29	2.02E+05	2.17E+05
39	1.97E+05	2.13E+05
49	1.94E+05	2.16E+05
59	1.91E+05	2.07E+05
69	1.96E+05	2.13E+05
79	1.96E+05	2.03E+05
89	1.94E+05	2.14E+05
99	1.97E+05	2.09E+05

Max Stress per Cycle				
Cycle No.	**Max (MPa)**	**Min (MPa)**	**Mean Stress (MPa)**	**Alt. Stress (MPa)**
1	602	-620	611	-9
2	605	-631	618	-13
3	603	-629	616	-13
4	603	-627	615	-12
5	603	-629	616	-13
6	602	-627	615	-13
7	599	-626	613	-14
8	601	-625	613	-12
9	600	-625	612	-12
19	599	-624	612	-13
29	602	-626	614	-12
39	602	-619	611	-9
49	598	-616	607	-9
59	599	-615	607	-8
69	603	-613	608	-5
79	595	-602	598	-4
89	592	-606	599	-7
99	605	-613	609	-4

Specimen No.6-1a (HR590DP)
Specimen Gage Dimensions: 0.130”x0.126”
Failure @ 238 Cycles @ 1.7% Strain

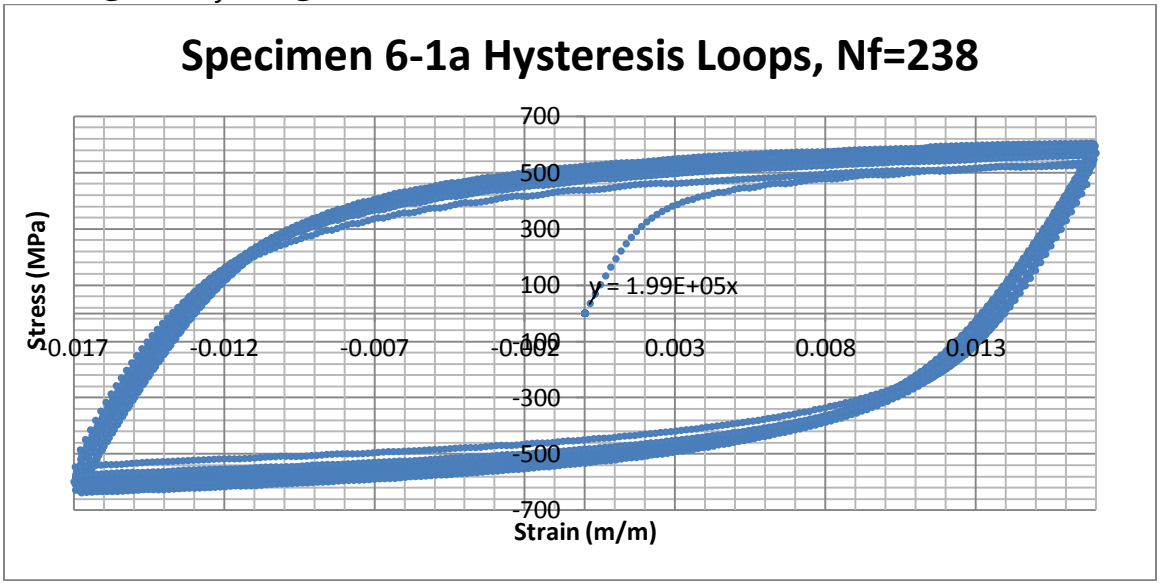

Young's Modulus per Cycle		
Cycle No.	**Compression Cycle (MPa)**	**Tension Cycle (MPa)**
1		1.99E+05
2	1.81E+05	1.85E+05
3	1.81E+05	1.87E+05
4	1.79E+05	1.84E+05
5	1.82E+05	1.87E+05
6	1.82E+05	1.88E+05
7	1.83E+05	1.91E+05
8	1.84E+05	1.88E+05
9	1.85E+05	1.91E+05
19	1.88E+05	1.97E+05
29	1.92E+05	2.05E+05
39	1.96E+05	2.05E+05
49	1.96E+05	2.06E+05
59	1.96E+05	2.04E+05
69	2.02E+05	2.04E+05
79	2.01E+05	2.10E+05
89	1.98E+05	2.12E+05
99	1.98E+05	2.09E+05
199	1.95E+05	2.14E+05

Max Stress per Cycle				
Cycle No.	**Max (MPa)**	**Min (MPa)**	**Mean Stress (MPa)**	**Alt. Stress (MPa)**
1	602	-624	613	-11
2	603	-638	620	-18
3	605	-633	619	-14
4	605	-630	618	-13
5	599	-630	614	-16
6	597	-626	611	-14
7	597	-624	611	-13
8	596	-619	608	-12
9	597	-618	607	-11
19	587	-608	597	-11
29	580	-599	589	-10
39	570	-595	583	-13
49	569	-588	579	-10
59	570	-586	578	-8
69	570	-580	575	-5
79	565	-581	573	-8
89	565	-577	571	-6
99	562	-574	568	-6
199	527	-546	537	-9

Specimen No.6-2a (HR590DP)
Specimen Gage Dimensions: 0.130”x0.127”
Failure @ 154 Cycles @ 1.7% Strain

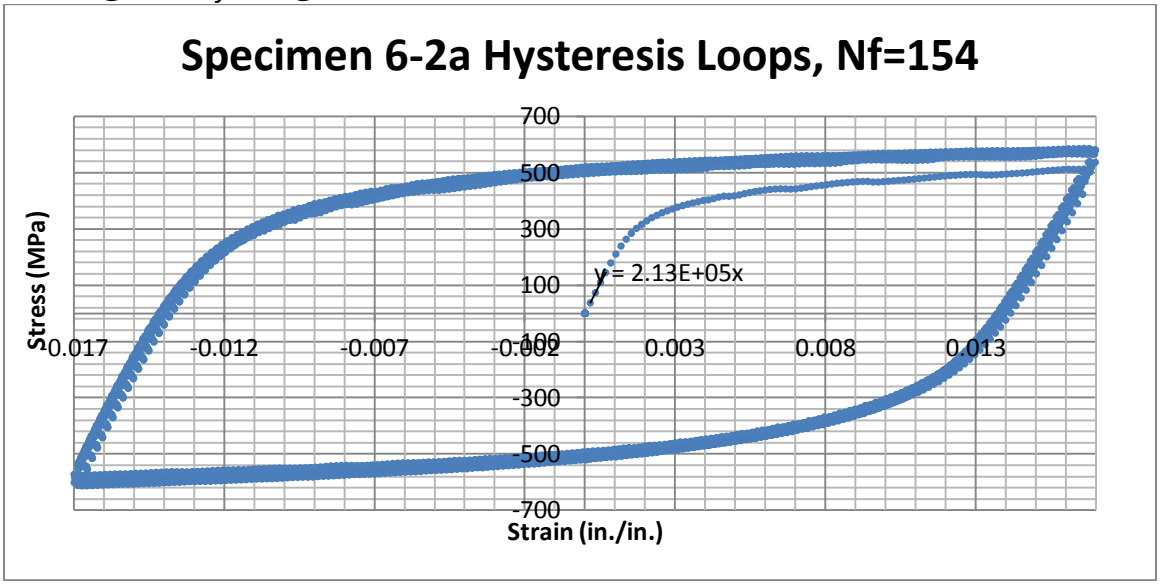

Cycle No.	Compression Cycle (MPa)	Tension Cycle (MPa)
1		2.14E+05
2	1.94E+05	2.15E+05
3	1.94E+05	2.15E+05
4	1.93E+05	2.16E+05
5	1.95E+05	2.16E+05
6	1.92E+05	2.17E+05
7	1.94E+05	2.18E+05
8	1.94E+05	2.16E+05
9	1.95E+05	2.17E+05
19	1.97E+05	2.24E+05
29	1.95E+05	2.24E+05
39	1.97E+05	2.22E+05
49	1.96E+05	2.23E+05
59	1.98E+05	2.21E+05
69	1.97E+05	2.20E+05
79	1.97E+05	2.23E+05
89	1.98E+05	2.23E+05
99	1.97E+05	2.25E+05

Cycle No.	Max (MPa)	Min (MPa)	Mean Stress (MPa)	Alt. Stress (MPa)
1	578	-600	589	-11
2	586	-613	600	-13
3	581	-611	596	-15
4	580	-612	596	-16
5	580	-610	595	-15
6	581	-611	596	-15
7	578	-609	594	-15
8	579	-607	593	-14
9	579	-606	593	-13
19	580	-602	591	-11
29	579	-598	589	-10
39	578	-593	586	-7
49	577	-591	584	-7
59	573	-587	580	-7
69	571	-584	578	-7
79	573	-581	577	-4
89	569	-578	574	-5
99	567	-576	571	-4

Specimen No.5-1a (HR590DP)
Specimen Gage Dimensions: 0.130”x0.126”
Failure @ 339 Cycles @ 1.4% Strain

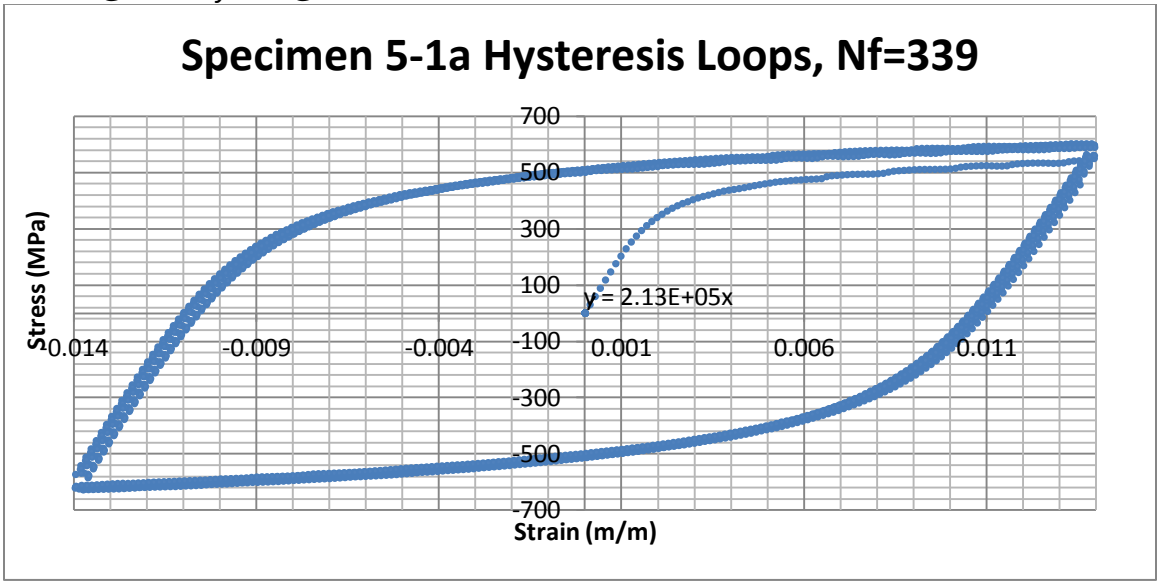

Young's Modulus per Cycle		
Cycle No.	**Compression Cycle (MPa)**	**Tension Cycle (MPa)**
1		2.15E+05
2	1.97E+05	2.10E+05
3	1.93E+05	2.10E+05
4	1.95E+05	2.09E+05
5	1.92E+05	2.11E+05
6	1.94E+05	2.11E+05
7	1.98E+05	2.12E+05
8	1.96E+05	2.13E+05
9	1.96E+05	2.12E+05
19	1.97E+05	2.16E+05
29	1.95E+05	2.14E+05
39	2.01E+05	2.20E+05
49	1.99E+05	2.18E+05
59	2.01E+05	2.19E+05
69	2.00E+05	2.22E+05
79	1.99E+05	2.23E+05
89	2.00E+05	2.22E+05
99	2.04E+05	2.20E+05
199	2.04E+05	2.29E+05

Max Stress per Cycle				
Cycle No.	**Max (MPa)**	**Min (MPa)**	**Mean Stress (MPa)**	**Alt. Stress (MPa)**
1	597	-617	607	-10
2	602	-628	615	-13
3	602	-628	615	-13
4	598	-625	612	-14
5	601	-622	611	-10
6	596	-621	608	-12
7	596	-617	607	-10
8	592	-616	604	-12
9	588	-612	600	-12
19	581	-603	592	-11
29	575	-597	586	-11
39	572	-590	581	-9
49	568	-587	577	-10
59	566	-583	575	-9
69	564	-582	573	-9
79	563	-581	572	-9
89	561	-578	570	-9
99	558	-575	567	-9
199	551	-562	556	-5

Specimen No.5-2a (HR590DP)
Specimen Gage Dimensions: 0.129”x0.126”
Failure @ 416 Cycles @ 1.4% Strain

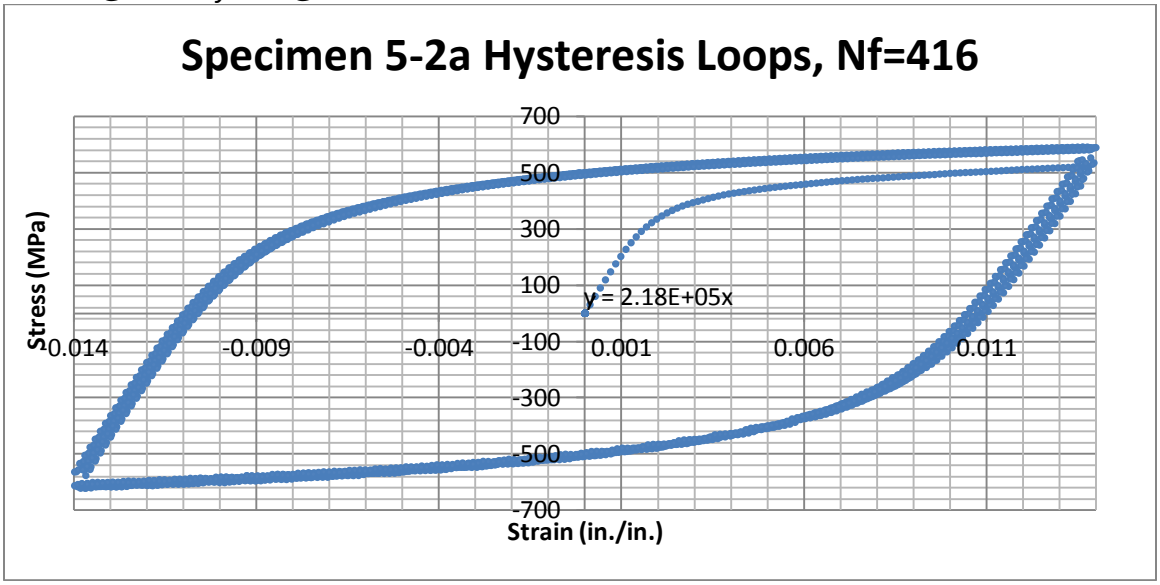

Young's Modulus per Cycle

Cycle No.	Compression Cycle (MPa)	Tension Cycle (MPa)
1		2.73E+05
2	1.99E+05	2.13E+05
3	1.95E+05	2.95E+05
4	1.94E+05	2.81E+05
5	1.97E+05	2.11E+05
6	1.96E+05	2.11E+05
7	1.93E+05	2.66E+05
8	1.93E+05	2.68E+05
9	1.95E+05	3.25E+05
19	1.94E+05	2.99E+05
29	1.94E+05	3.19E+05
39	1.98E+05	2.65E+05
49	2.18E+05	3.16E+05
59	1.93E+05	4.58E+05
69	2.48E+05	2.87E+05
79	1.99E+05	4.92E+05
89	1.99E+05	3.96E+05
99	2.43E+05	3.52E+05
199	2.02E+05	3.20E+05

Max Stress per Cycle

Cycle No.	Max (MPa)	Min (MPa)	Mean Stress (MPa)	Alt. Stress (MPa)
1	585	-607	596	-11
2	591	-622	606	-15
3	591	-621	606	-15
4	589	-617	603	-14
5	589	-619	604	-15
6	587	-616	602	-15
7	585	-612	598	-14
8	583	-610	596	-14
9	581	-607	594	-13
19	572	-597	585	-13
29	566	-590	578	-12
39	562	-586	574	-12
49	558	-583	571	-12
59	556	-578	567	-11
69	554	-577	565	-11
79	552	-575	563	-11
89	551	-573	562	-11
99	549	-568	558	-10
199	541	-557	549	-8

Specimen No. 4-2a (HR590DP)
Specimen Gage Dimensions: 0.130”x0.127”
Failure @ 722 Cycles @ 1.1% Strain

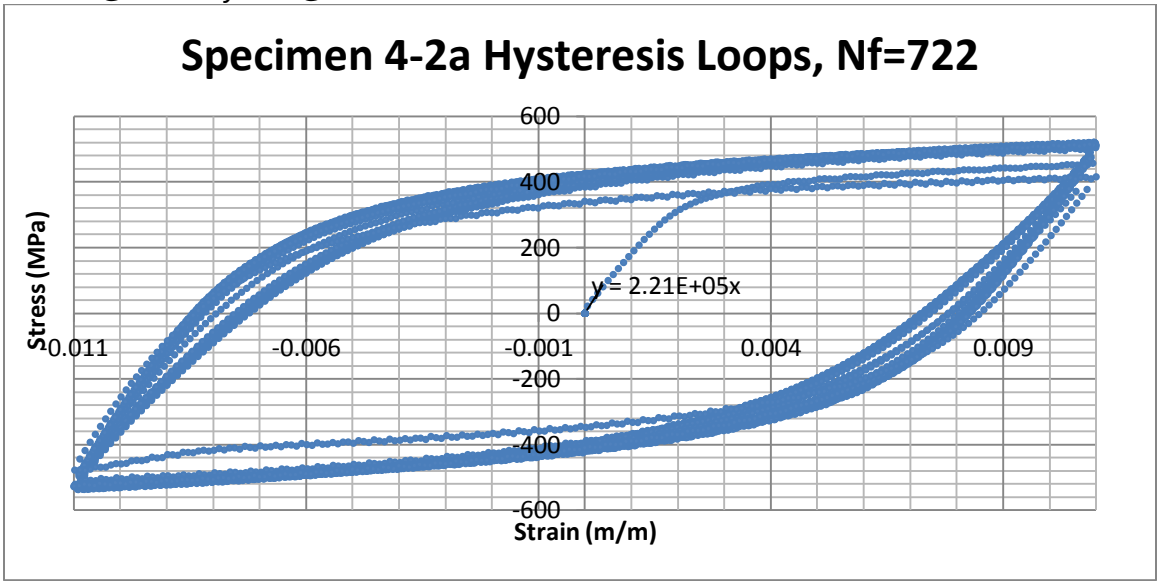

Young's Modulus per Cycle		
Cycle No.	**Compression Cycle (MPa)**	**Tension Cycle (MPa)**
1	#DIV/0!	1.77E+05
2	1.69E+05	1.70E+05
3	1.63E+05	1.70E+05
4	1.64E+05	1.71E+05
5	1.64E+05	1.72E+05
6	1.68E+05	1.78E+05
7	1.69E+05	1.80E+05
8	1.71E+05	1.81E+05
9	1.76E+05	1.84E+05
19	1.88E+05	2.00E+05
39	1.97E+05	2.09E+05
59	2.00E+05	2.12E+05
79	1.99E+05	2.10E+05
99	2.02E+05	2.17E+05
199	2.07E+05	2.20E+05
299	2.07E+05	2.24E+05
399	2.08E+05	2.28E+05
499	2.09E+05	2.31E+05
599	2.08E+05	2.27E+05
699	#DIV/0!	2.55E+05

Max Stress per Cycle				
Cycle No.	**Max (MPa)**	**Min (MPa)**	**Mean Stress (MPa)**	**Alt. Stress (MPa)**
1	505	-510	507	-2
2	514	-529	522	-7
3	518	-535	526	-9
4	520	-536	528	-8
5	521	-537	529	-8
6	521	-536	529	-8
7	520	-536	528	-8
8	520	-535	528	-8
9	520	-534	527	-7
19	518	-530	524	-6
39	515	-530	523	-7
59	515	-528	521	-7
79	514	-526	520	-6
99	512	-527	520	-7
199	511	-522	517	-6
299	511	-522	517	-6
399	513	-525	519	-6
499	515	-528	521	-6
599	515	-526	521	-6
699	416	-478	447	-31

Specimen No.4-3a (HR590DP)
Specimen Gage Dimensions: 0.129”x0.126”
Failure @ 656 Cycles @ 1.1% Strain

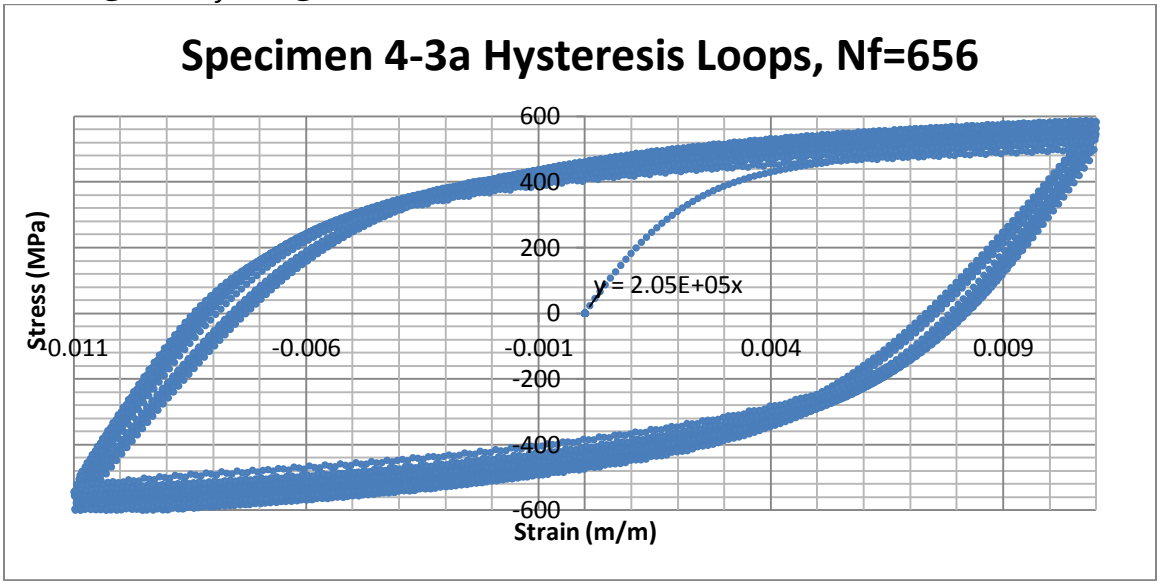

Young's Modulus per Cycle		
Cycle No.	**Compression Cycle (MPa)**	**Tension Cycle (MPa)**
1	1.94E+05	1.85E+05
2	2.48E+04	1.77E+05
3	2.45E+04	1.74E+05
4	2.46E+04	1.75E+05
5	2.34E+04	1.77E+05
6	2.39E+04	1.78E+05
7	2.22E+04	1.82E+05
8	2.23E+04	1.83E+05
9	2.15E+04	1.86E+05
19	1.92E+04	1.90E+05
39	1.84E+04	1.98E+05
59	1.62E+04	1.96E+05
79	1.45E+04	2.01E+05
99	1.44E+04	1.99E+05
199	1.37E+04	2.04E+05
299	1.36E+04	2.07E+05
399	1.34E+04	2.07E+05
499	1.32E+04	2.11E+05
599	1.23E+04	2.05E+05

Max Stress per Cycle				
Cycle No.	**Max (MPa)**	**Min (MPa)**	**Mean Stress (MPa)**	**Alt. Stress (MPa)**
1	579	-595	587	-8
2	587	-613	600	-13
3	588	-611	599	-12
4	586	-610	598	-12
5	585	-608	597	-12
6	584	-606	595	-11
7	582	-604	593	-11
8	579	-601	590	-11
9	579	-600	589	-10
19	568	-583	576	-7
39	555	-571	563	-8
59	550	-564	557	-7
79	543	-558	551	-7
99	541	-556	548	-8
199	530	-546	538	-8
299	528	-544	536	-8
399	527	-542	534	-7
499	527	-539	533	-6
599	503	-525	514	-11

Specimen No.3-1a (HR590DP)
Specimen Gage Dimensions: 0.129”x0.126”
Failure @ 1709 Cycles @ 0.8% Strain

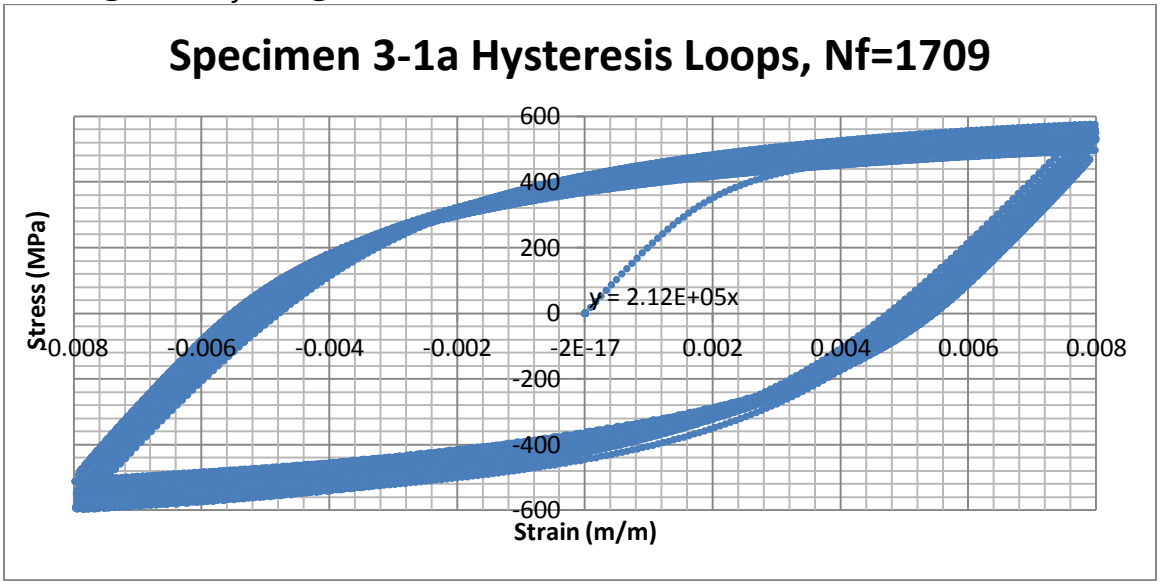

Young's Modulus per Cycle

Cycle No.	Compression Cycle (MPa)	Tension Cycle (MPa)
4	2.00E+05	2.08E+05
9	1.99E+05	2.10E+05
19	2.05E+05	2.12E+05
29	2.03E+05	2.15E+05
39	2.05E+05	2.14E+05
49	2.09E+05	2.18E+05
59	2.10E+05	2.21E+05
69	2.09E+05	2.20E+05
79	2.11E+05	2.19E+05
89	2.07E+05	2.21E+05
99	2.08E+05	2.22E+05
299	2.16E+05	2.54E+05
599	2.22E+05	2.88E+05
699	2.61E+05	2.30E+05
799	2.22E+05	2.37E+05
899	2.24E+05	2.35E+05
999	2.20E+05	2.35E+05

Max Stress per Cycle

Cycle No.	Max (MPa)	Min (MPa)	Mean Stress (MPa)	Alt. Stress (MPa)
4	575	-596	586	-10
9	570	-592	581	-11
19	561	-579	570	-9
29	551	-569	560	-9
39	544	-563	554	-9
49	539	-559	549	-10
59	534	-554	544	-10
69	532	-549	540	-8
79	529	-546	537	-8
89	525	-544	535	-9
99	524	-542	533	-9
299	502	-518	510	-8
599	497	-512	504	-7
699	498	-512	505	-7
799	497	-511	504	-7
899	498	-512	505	-7
999	499	-513	506	-7

Specimen No.3-2a (HR590DP)
Specimen Gage Dimensions: 0.127”x0.129”
Failure @ 1319 Cycles @ 0.8% Strain

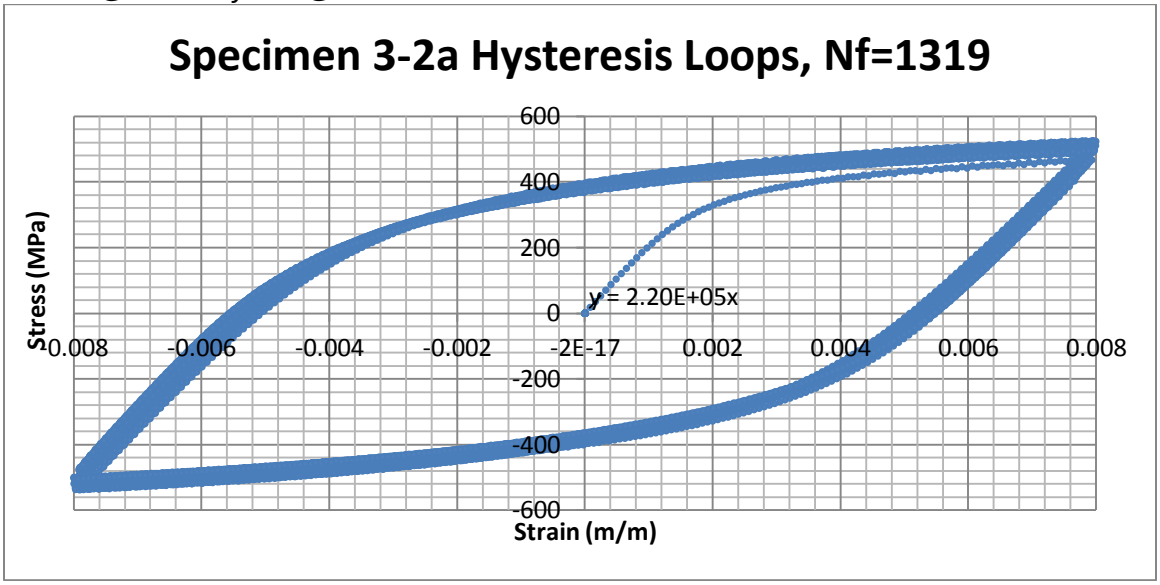

Young's Modulus per Cycle		
Cycle No.	**Compression Cycle (MPa)**	**Tension Cycle (MPa)**
4	1.91E+05	2.02E+05
9	1.91E+05	2.02E+05
19	1.92E+05	2.04E+05
29	1.93E+05	2.04E+05
39	1.94E+05	2.04E+05
49	1.93E+05	2.06E+05
59	1.95E+05	2.06E+05
69	1.96E+05	2.07E+05
79	1.96E+05	2.05E+05
89	1.98E+05	2.07E+05
99	1.97E+05	2.09E+05
299	2.03E+05	2.14E+05
599	2.07E+05	2.17E+05
699	2.06E+05	2.18E+05
799	2.08E+05	2.19E+05
899	2.09E+05	2.19E+05
999	2.10E+05	2.20E+05

Max Stress per Cycle				
Cycle No.	**Max (MPa)**	**Min (MPa)**	**Mean Stress (MPa)**	**Alt. Stress (MPa)**
4	526	-537	531	-5
9	523	-532	528	-4
19	513	-525	519	-6
29	509	-521	515	-6
39	509	-519	514	-5
49	505	-518	512	-6
59	505	-516	511	-5
69	502	-513	507	-6
79	502	-513	507	-6
89	499	-513	506	-7
99	500	-511	505	-5
299	493	-503	498	-5
599	493	-501	497	-4
699	492	-501	497	-5
799	494	-502	498	-4
899	494	-504	499	-5
999	495	-504	500	-4

Specimen No.2-1a (HR590DP)
Specimen Gage Dimensions: 0.129”x0.127”
Failure @ 4602 Cycles @ 0.5% Strain

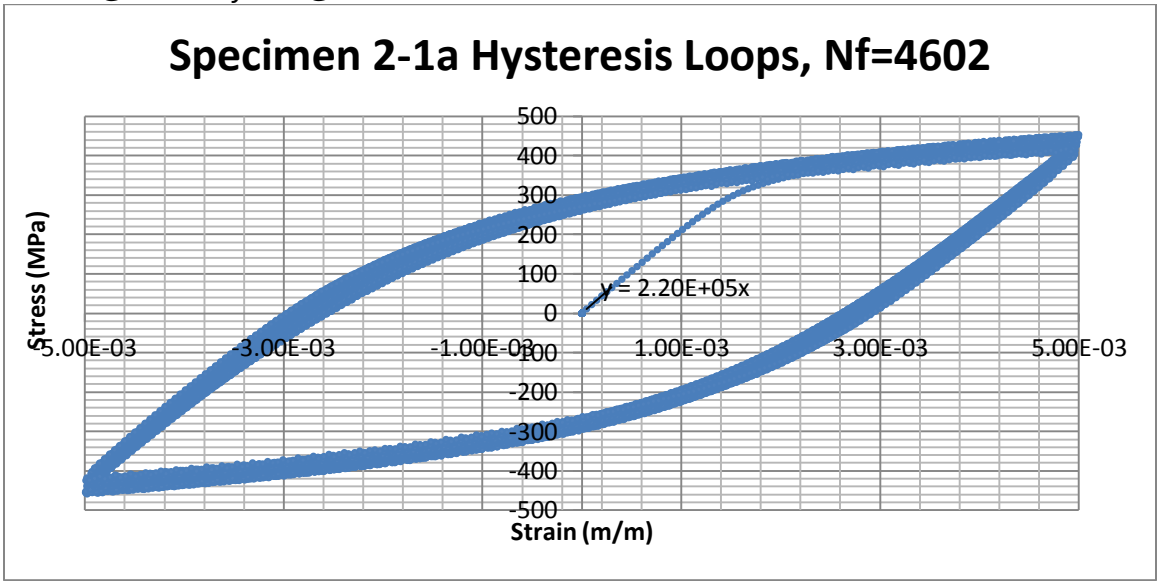

Young's Modulus per Cycle

Cycle No.	Compression Cycle (MPa)	Tension Cycle (MPa)
4	1.98E+05	2.05E+05
9	1.96E+05	2.03E+05
19	1.99E+05	2.05E+05
29	1.98E+05	2.06E+05
39	1.99E+05	2.05E+05
49	1.99E+05	2.05E+05
59	2.00E+05	2.07E+05
69	2.00E+05	2.06E+05
79	2.01E+05	2.07E+05
89	2.01E+05	2.07E+05
99	2.01E+05	2.07E+05
299	2.05E+05	2.12E+05
599	2.08E+05	2.13E+05
699	2.07E+05	2.16E+05
799	2.09E+05	2.15E+05
899	2.10E+05	2.16E+05
999	2.08E+05	2.16E+05
1999	2.14E+05	2.20E+05
2999	2.14E+05	2.22E+05
3999	2.13E+05	2.21E+05

Max Stress per Cycle

Cycle No.	Max (MPa)	Min (MPa)	Mean Stress (MPa)	Alt. Stress (MPa)
4	441	-446	443	-2
9	449	-454	451	-3
19	454	-455	455	-1
29	453	-456	455	-2
39	453	-458	456	-3
49	452	-455	454	-1
59	453	-457	455	-2
69	450	-455	452	-2
79	450	-453	451	-2
89	450	-454	452	-2
99	449	-452	451	-1
299	437	-441	439	-2
599	429	-433	431	-2
699	429	-432	430	-1
799	427	-430	429	-2
899	425	-429	427	-2
999	422	-427	425	-3
1999	420	-422	421	-1
2999	419	-423	421	-2
3999	417	-423	420	-3

Specimen No.2-3a (HR590DP)
Specimen Gage Dimensions: 0.127”x0.130”
Failure @ 6555 Cycles @ 0.5% Strain

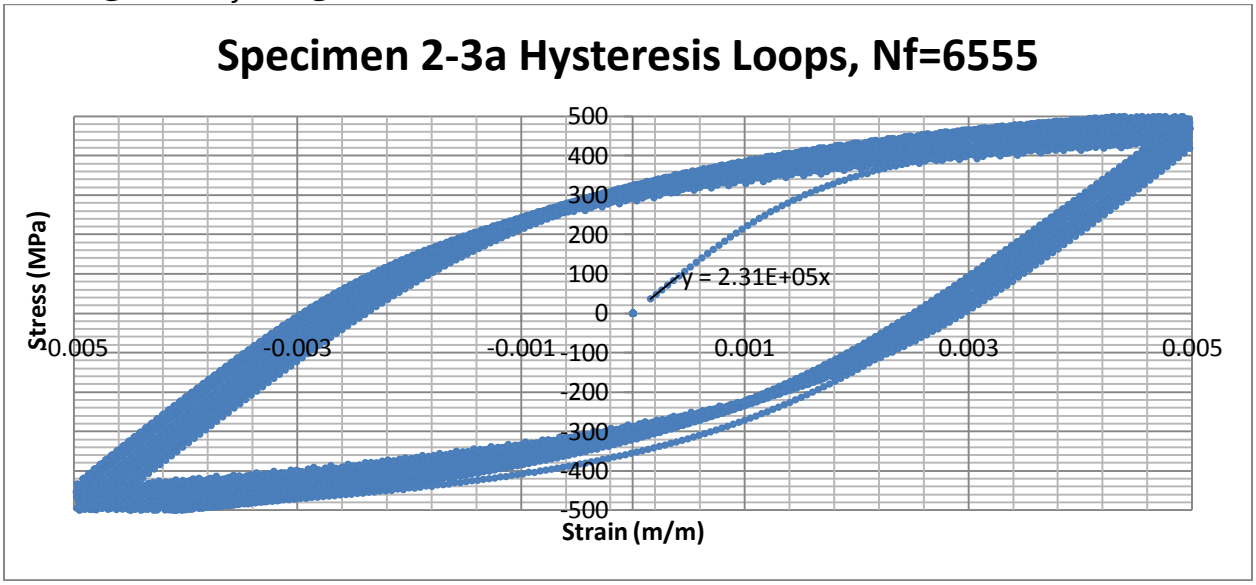

Young's Modulus per Cycle		
Cycle No.	**Compression Cycle (MPa)**	**Tension Cycle (MPa)**
4	2.08E+05	2.17E+05
9	2.08E+05	2.16E+05
19	2.08E+05	2.20E+05
39	2.09E+05	2.21E+05
59	2.09E+05	2.22E+05
79	2.11E+05	2.21E+05
99	2.12E+05	2.21E+05
299	2.15E+05	2.26E+05
599	2.17E+05	2.28E+05
699	2.18E+05	2.29E+05
799	2.21E+05	2.28E+05
899	1.96E+05	2.30E+05
999	2.23E+05	2.32E+05
1999	2.23E+05	2.31E+05

Max Stress per Cycle				
Cycle No.	**Max (MPa)**	**Min (MPa)**	**Mean Stress (MPa)**	**Alt. Stress (MPa)**
4	511	-518	514	-3
9	510	-517	514	-3
19	506	-511	509	-2
39	494	-506	500	-6
59	490	-501	496	-6
79	484	-494	489	-5
99	482	-491	487	-4
299	460	-472	466	-6
599	451	-458	455	-4
699	448	-457	453	-4
799	448	-454	451	-3
899	444	-452	448	-4
999	445	-453	449	-4
1999	444	-448	446	-2

Specimen 1_5-1a (HR590DP)
Specimen Gage Dimensions: 0.130”x0.126”
Failure @ 15634 Cycles @ 0.35% Strain

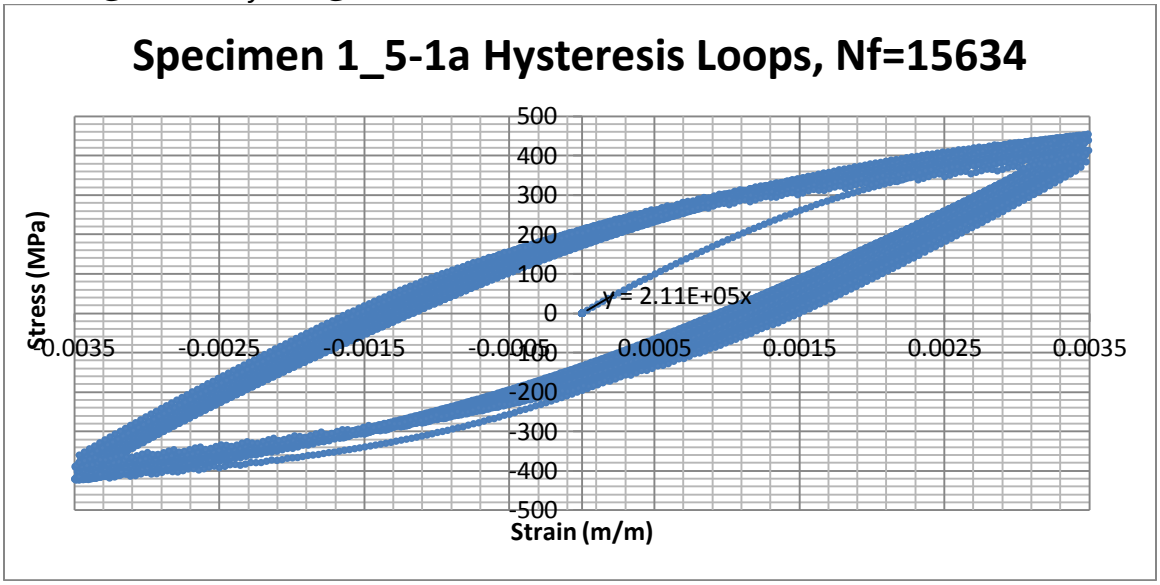

Young's Modulus per Cycle

Cycle No.	Compression Cycle (MPa)	Tension Cycle (MPa)
4	1.85E+05	1.96E+05
9	1.86E+05	1.96E+05
19	1.89E+05	1.97E+05
39	1.90E+05	1.99E+05
59	1.92E+05	2.00E+05
79	1.92E+05	2.00E+05
99	1.94E+05	1.99E+05
299	1.94E+05	2.04E+05
599	1.97E+05	2.03E+05
699	1.97E+05	2.06E+05
799	1.98E+05	2.07E+05
899	1.99E+05	2.07E+05
999	1.98E+05	2.08E+05
1999	2.03E+05	2.08E+05
3999	2.07E+05	2.13E+05
5999	2.08E+05	2.17E+05
7999	2.09E+05	2.15E+05
9999	2.08E+05	2.14E+05

Max Stress per Cycle

Cycle No.	Max (MPa)	Min (MPa)	Mean Stress (MPa)	Alt. Stress (MPa)
4	453	-419	436	17
9	450	-423	436	13
19	449	-421	435	14
39	452	-421	436	16
59	449	-417	433	16
79	449	-418	433	15
99	445	-414	429	15
299	435	-403	419	16
599	418	-395	407	11
699	412	-392	402	10
799	408	-391	399	8
899	408	-389	398	10
999	403	-386	394	8
1999	385	-378	382	4
3999	375	-367	371	4
5999	372	-365	368	4
7999	367	-363	365	2
9999	366	-363	365	1

Specimen 1_5-2a (HR590DP)
Specimen Gage Dimensions: 0.130”x0.126”
Failure @ 14533 Cycles @ 0.35% Strain

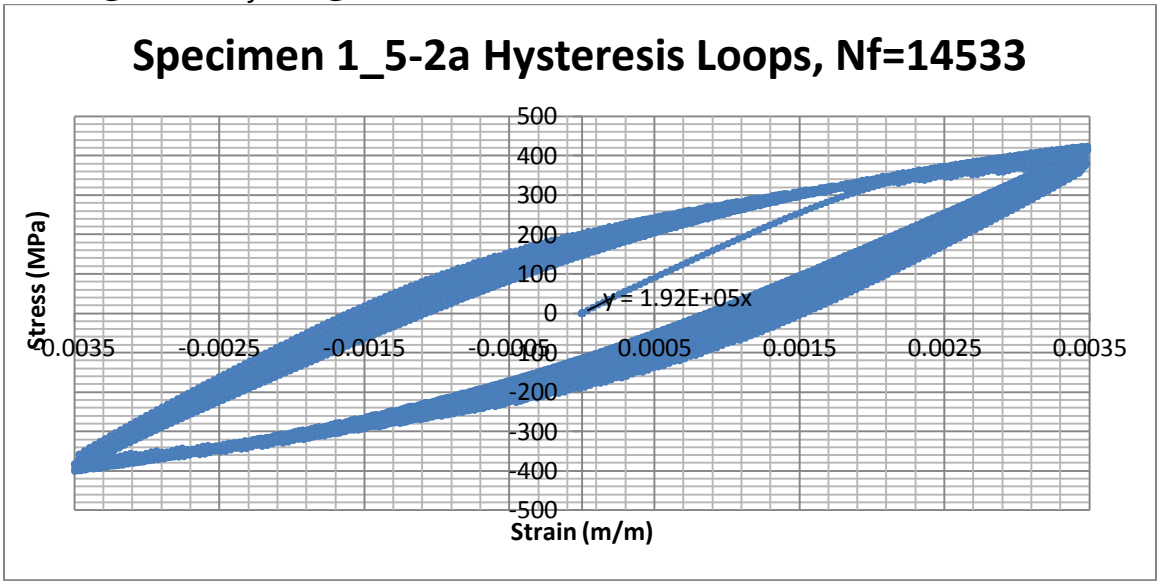

Young's Modulus per Cycle

Cycle No.	Compression Cycle (MPa)	Tension Cycle (MPa)
4	1.67E+05	1.74E+05
9	1.66E+05	1.73E+05
19	1.65E+05	1.74E+05
39	1.68E+05	1.78E+05
59	1.71E+05	1.80E+05
79	1.72E+05	1.83E+05
99	1.75E+05	1.85E+05
299	1.87E+05	1.96E+05
599	1.95E+05	2.01E+05
699	1.97E+05	2.05E+05
799	1.98E+05	2.06E+05
899	1.98E+05	2.07E+05
999	1.99E+05	2.06E+05
1999	2.02E+05	2.12E+05
3999	2.06E+05	2.16E+05
5999	2.07E+05	2.19E+05
7999	2.08E+05	2.15E+05
9999	2.09E+05	2.17E+05

Max Stress per Cycle

Cycle No.	Max (MPa)	Min (MPa)	Mean Stress (MPa)	Alt. Stress (MPa)
4	416	-387	401	14
9	422	-395	409	14
19	422	-398	410	12
39	421	-401	411	10
59	426	-399	412	14
79	422	-398	410	12
99	420	-396	408	12
299	411	-394	403	9
599	404	-388	396	8
699	401	-388	395	7
799	397	-386	392	6
899	397	-385	391	6
999	395	-384	390	6
1999	381	-371	376	5
3999	371	-359	365	6
5999	365	-356	360	4
7999	362	-355	359	3
9999	360	-353	356	3

Specimen 1_3-1a (HR590DP)
Specimen Gage Dimensions: 0.130”x0.126”
Failure @ 28000 Cycles @ 0.29% Strain

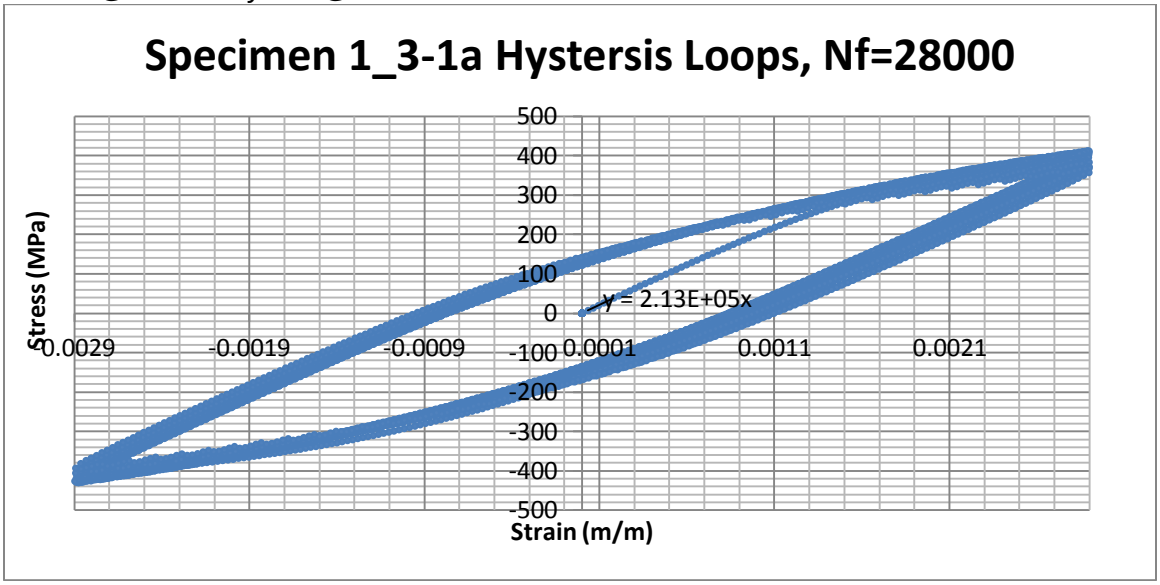

Young's Modulus per Cycle		
Cycle No.	**Compression Cycle (MPa)**	**Tension Cycle (MPa)**
4	2.06E+05	2.10E+05
9	2.05E+05	2.09E+05
19	2.03E+05	2.08E+05
39	2.03E+05	2.07E+05
59	2.04E+05	2.06E+05
79	2.02E+05	2.06E+05
99	2.02E+05	2.05E+05
299	2.04E+05	2.04E+05
599	2.05E+05	2.08E+05
699	2.06E+05	2.10E+05
799	2.06E+05	2.08E+05
899	2.05E+05	2.08E+05
999	2.08E+05	2.09E+05
1999	2.10E+05	2.14E+05
3999	2.15E+05	2.14E+05
5999	2.11E+05	2.17E+05
7999	2.13E+05	2.16E+05
9999	2.28E+05	2.17E+05

Max Stress per Cycle				
Cycle No.	**Max (MPa)**	**Min (MPa)**	**Mean Stress (MPa)**	**Alt. Stress (MPa)**
4	401	-415	408	-7
9	409	-421	415	-6
19	411	-425	418	-7
39	411	-429	420	-9
59	413	-428	421	-7
79	405	-429	417	-12
99	412	-430	421	-9
299	398	-424	411	-13
599	388	-414	401	-13
699	388	-407	398	-9
799	385	-411	398	-13
899	387	-410	398	-12
999	380	-406	393	-13
1999	368	-395	381	-13
3999	356	-384	370	-14
5999	349	-379	364	-15
7999	343	-378	361	-18
9999	341	-376	358	-18

Specimen 1_1-1a (HR590DP)
Specimen Gage Dimensions: 0.132”x0.129”
Failure @ 48318 Cycles @ 0.23% Strain

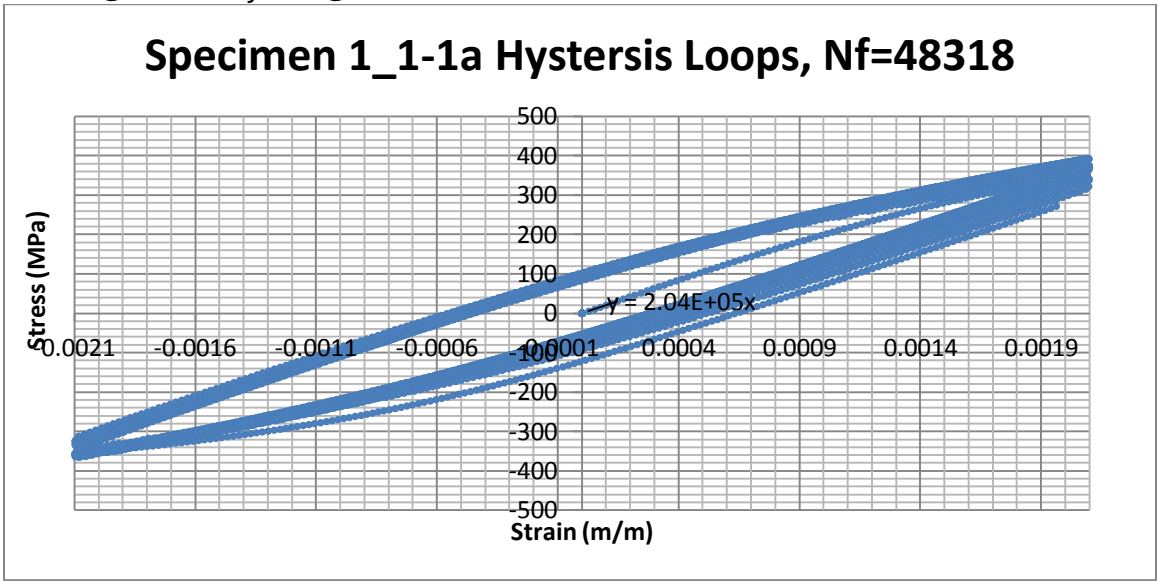

Young's Modulus per Cycle		
Cycle No.	**Compression Cycle (MPa)**	**Tension Cycle (MPa)**
4	2.14E+05	2.32E+05
9	2.10E+05	2.29E+05
19	2.10E+05	2.27E+05
39	2.10E+05	2.23E+05
59	2.08E+05	2.23E+05
79	2.11E+05	2.21E+05
99	2.07E+05	2.20E+05
299	2.11E+05	2.20E+05
599	2.11E+05	2.17E+05
699	2.13E+05	2.20E+05
799	2.14E+05	2.18E+05
899	2.13E+05	2.19E+05
999	2.10E+05	2.19E+05
1999	2.16E+05	2.20E+05
3999	2.17E+05	2.22E+05
5999	2.17E+05	2.38E+05
7999	2.16E+05	2.37E+05
9999	2.38E+05	2.35E+05

Max Stress per Cycle				
Cycle No.	**Max (MPa)**	**Min (MPa)**	**Mean Stress (MPa)**	**Alt. Stress (MPa)**
1	394	-357	375	19
2	397	-355	376	21
3	399	-355	377	22
4	401	-358	379	22
5	400	-361	381	20
6	402	-364	383	19
7	404	-365	385	19
8	404	-366	385	19
9	405	-367	386	19
19	413	-371	392	21
29	414	-373	394	20
39	413	-374	394	19
49	413	-375	394	19
59	411	-377	394	17
69	410	-378	394	16
79	411	-378	394	16
89	409	-378	393	15
99	410	-380	395	15

Specimen 1_1-2a (HR590DP)
Specimen Gage Dimensions: 0.132”x0.129”
Failure @ 41102 Cycles @ 0.23% Strain

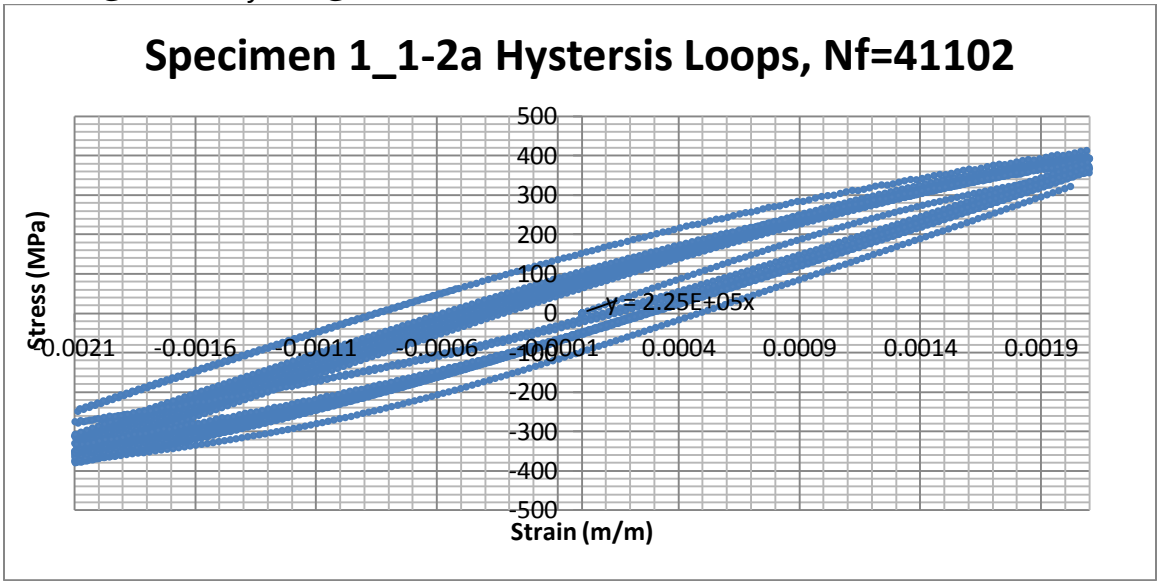

Young's Modulus per Cycle		
Cycle No.	**Compression Cycle (MPa)**	**Tension Cycle (MPa)**
4	2.07E+05	2.12E+05
9	2.04E+05	2.09E+05
19	2.04E+05	2.09E+05
39	2.04E+05	2.08E+05
59	2.03E+05	2.06E+05
79	2.03E+05	2.08E+05
99	2.03E+05	2.07E+05
299	2.01E+05	2.09E+05
599	2.02E+05	2.09E+05
699	2.02E+05	2.09E+05
799	2.02E+05	2.09E+05
899	2.03E+05	2.12E+05
999	2.02E+05	2.10E+05
1999	1.96E+05	2.26E+05
3999	1.97E+05	2.25E+05
5999	1.98E+05	2.06E+05
7999	2.01E+05	2.10E+05
9999	2.02E+05	2.07E+05

Max Stress per Cycle				
Cycle No.	**Max (MPa)**	**Min (MPa)**	**Mean Stress (MPa)**	**Alt. Stress (MPa)**
1	404	-382	393	11
2	407	-386	396	10
3	406	-389	397	8
4	408	-380	394	14
5	405	-382	393	12
6	406	-392	399	7
7	408	-395	401	6
8	408	-394	401	7
9	407	-396	401	5
19	413	-396	404	8
29	408	-398	403	5
39	411	-392	402	9
49	412	-396	404	8
59	416	-397	407	10
69	411	-389	400	11
79	417	-394	405	11
89	413	-390	402	11
99	412	-394	403	9

Specimen No.1-3a (HR590DP)
Specimen Gage Dimensions: 0.129”x0.126”
Failure @ 176620 Cycles @ 0.2% Strain
Offset@19900: -0.0005in/in
Offset@59900: -0.0006in/in

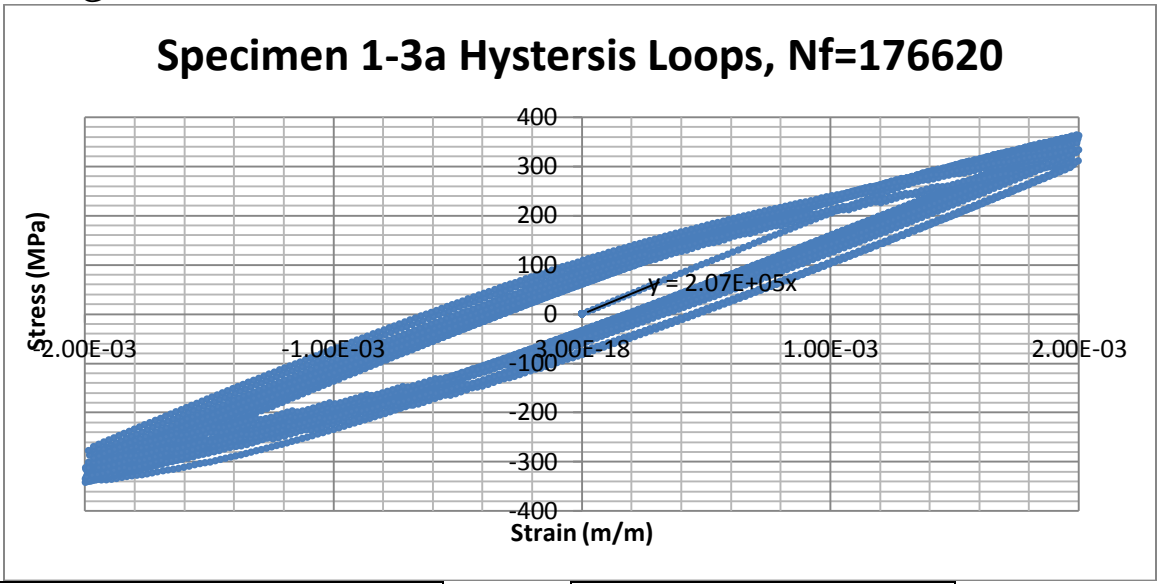

Young's Modulus per Cycle

Cycle No.	Compression Cycle (MPa)	Tension Cycle (MPa)
4	2.06E+05	2.09E+05
9	2.03E+05	2.08E+05
19	2.02E+05	2.08E+05
39	2.02E+05	2.07E+05
59	2.01E+05	2.06E+05
79	2.00E+05	2.05E+05
99	2.01E+05	2.06E+05
399	2.01E+05	2.05E+05
699	2.01E+05	2.06E+05
999	2.04E+05	2.06E+05
3999	2.02E+05	2.07E+05
6999	2.03E+05	2.10E+05
9999	2.02E+05	2.10E+05
39999	2.05E+05	2.12E+05
69999	2.08E+05	2.10E+05
79999	2.09E+05	2.10E+05
89999	2.07E+05	2.09E+05
99999	2.10E+05	2.09E+05

Max Stress per Cycle

Cycle No.	Max (MPa)	Min (MPa)	Mean Stress (MPa)	Alt. Stress (MPa)
4	341	-323	332	9
9	343	-324	333	10
19	349	-326	337	12
39	352	-330	341	11
59	354	-330	342	12
79	356	-333	344	11
99	357	-334	346	11
399	362	-342	352	10
699	359	-339	349	10
999	361	-336	348	13
3999	354	-322	338	16
6999	344	-315	330	14
9999	339	-306	322	17
39999	328	-287	307	20
69999	303	-301	302	1
79999	304	-302	303	1
89999	304	-299	302	2
99999	306	-301	303	3

Specimen No.1-5a (HR590DP)
Specimen Gage Dimensions: 0.126”x0.129”
Failure @ 160036 Cycles @ 0.2% Strain @0.005in/in/s

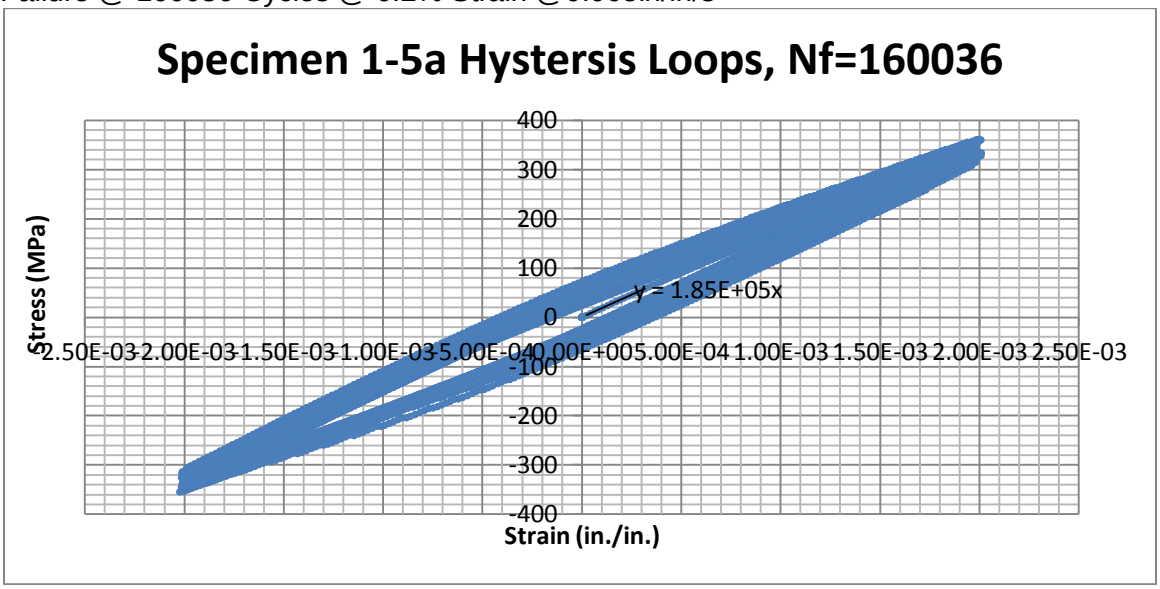

Young's Modulus per Cycle

Cycle No.	Compression Cycle (MPa)	Tension Cycle (MPa)
4	1.91E+05	1.92E+05
9	1.88E+05	1.91E+05
19	1.88E+05	1.90E+05
39	1.90E+05	1.92E+05
59	1.88E+05	1.91E+05
79	1.90E+05	1.92E+05
99	1.92E+05	1.93E+05
399	1.94E+05	1.96E+05
699	1.93E+05	1.98E+05
999	1.94E+05	2.00E+05
3999	1.96E+05	2.00E+05
6999	1.95E+05	2.01E+05
9999	1.95E+05	2.02E+05
39999	1.99E+05	2.03E+05
69999	1.97E+05	2.04E+05
79999	1.98E+05	2.05E+05
89999	1.99E+05	2.05E+05
99999	2.00E+05	2.06E+05

Max Stress per Cycle

Cycle No.	Max (MPa)	Min (MPa)	Mean Stress (MPa)	Alt. Stress (MPa)
4	313	-314	314	0
9	319	-320	320	-1
19	323	-324	323	-1
39	324	-330	327	-3
59	331	-330	331	0
79	328	-337	333	-5
99	332	-335	334	-2
399	345	-344	344	0
699	350	-347	348	1
999	357	-355	356	1
3999	358	-340	349	9
6999	360	-326	343	17
9999	350	-326	338	12
39999	326	-318	322	4
69999	326	-305	315	10
79999	327	-305	316	11
89999	327	-301	314	13
99999	327	-301	314	13

Specimen No.7-1b (HR590)
Specimen Gage Dimensions: 0.125”x0.130”
Failure @ 123 Cycles @ 2.0% Strain

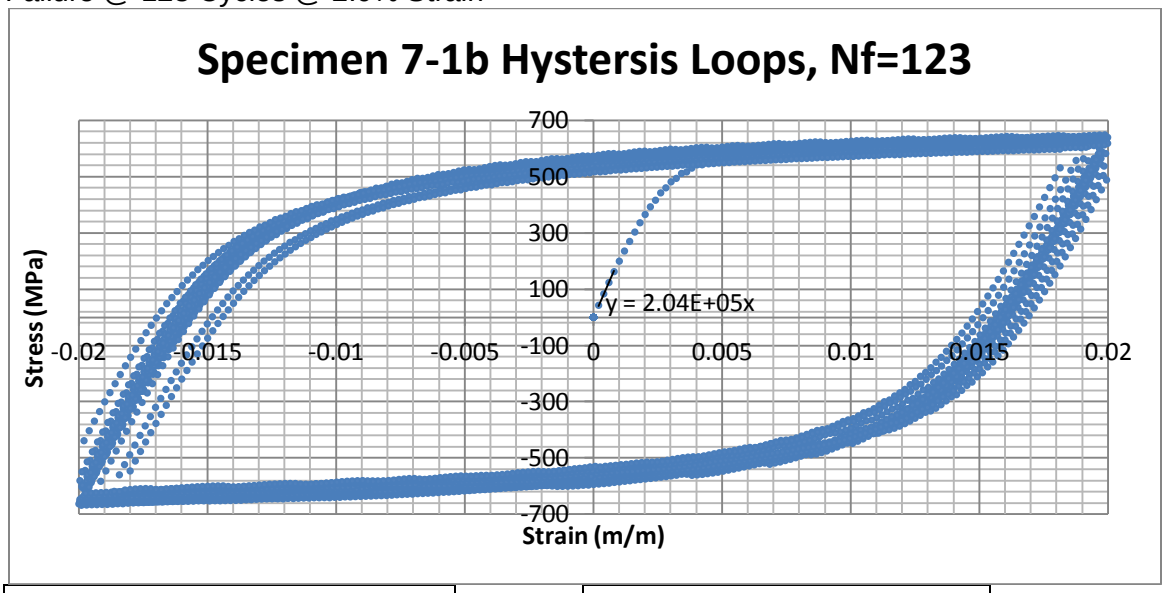

Young's Modulus per Cycle

Cycle No.	Compression Cycle (MPa)	Tension Cycle (MPa)
1	1.79E+05	1.65E+05
2	1.70E+05	1.69E+05
3	1.70E+05	1.70E+05
4	1.68E+05	1.69E+05
5	1.70E+05	1.70E+05
6	1.73E+05	1.70E+05
7	1.74E+05	1.70E+05
8	1.75E+05	1.72E+05
9	1.75E+05	1.73E+05
19	1.76E+05	1.75E+05
29	1.77E+05	1.79E+05
39	1.79E+05	1.78E+05
49	1.80E+05	1.78E+05
59	1.79E+05	1.77E+05
69	1.82E+05	1.78E+05
79	1.82E+05	1.77E+05
89	1.82E+05	1.77E+05
99	1.77E+05	1.78E+05

Max Stress per Cycle

Cycle No.	Max (MPa)	Min (MPa)	Mean Stress (MPa)	Alt. Stress (MPa)
1	648	-668	658	-10
2	648	-660	654	-6
3	643	-658	650	-7
4	641	-663	652	-11
5	640	-662	651	-11
6	639	-659	649	-10
7	637	-657	647	-10
8	638	-659	649	-11
9	638	-659	648	-10
19	635	-654	644	-10
29	635	-650	643	-8
39	632	-652	642	-10
49	631	-651	641	-10
59	631	-648	639	-8
69	628	-647	637	-9
79	623	-642	633	-10
89	620	-642	631	-11
99	620	-634	627	-7

Specimen No.7-2b (HR590)
Specimen Gage Dimensions: 0.126”x0.131”
Failure @ 100 Cycles @ 2.0% Strain

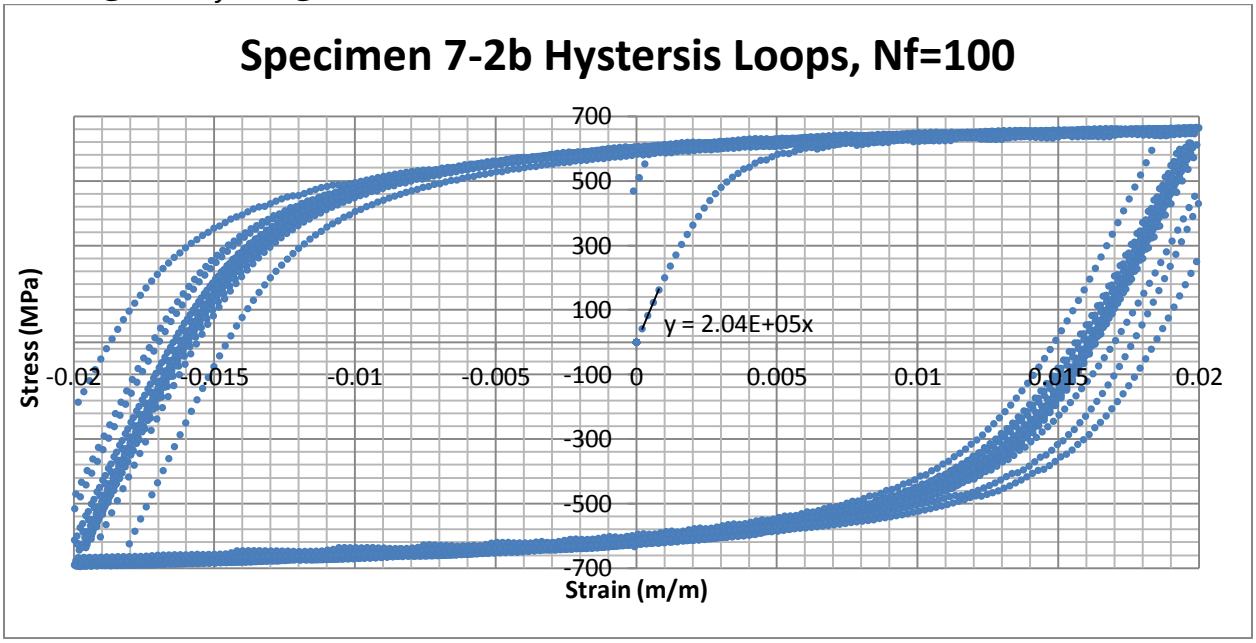

Young's Modulus per Cycle*		
Cycle No.	**Compression Cycle (MPa)**	**Tension Cycle (MPa)**
1	1.92E+05	1.73E+05
2	1.82E+05	1.78E+05
3	1.82E+05	1.82E+05
4	1.79E+05	1.85E+05
5	1.82E+05	1.84E+05
6	1.83E+05	1.86E+05
7	1.81E+05	1.87E+05
8	1.81E+05	1.88E+05
9	1.82E+05	1.87E+05
19	1.81E+05	1.86E+05
29	1.80E+05	1.83E+05
39	1.81E+05	1.86E+05
49	1.81E+05	1.84E+05
59	1.81E+05	1.87E+05
69	1.86E+05	1.87E+05
79	1.90E+05	1.89E+05
89	1.97E+05	1.86E+05
99	2.04E+05	1.84E+05

Max Stress per Cycle				
Cycle No.	**Max (MPa)**	**Min (MPa)**	**Mean Stress (MPa)**	**Alt. Stress (MPa)**
1	665	-690	678	-12
2	666	-693	679	-14
3	663	-695	679	-16
4	664	-692	678	-14
5	664	-695	680	-15
6	663	-692	678	-15
7	663	-693	678	-15
8	662	-694	678	-16
9	661	-693	677	-16
19	663	-693	678	-15
29	665	-693	679	-14
39	663	-688	676	-13
49	661	-686	674	-13
59	664	-690	677	-13
69	660	-681	671	-10
79	651	-673	662	-11
89	655	-678	667	-12
99	653	-681	667	-14

Specimen No.6-1b (HR590)
Specimen Gage Dimensions: 0.126”x0.131”
Failure @ 187 Cycles @ 1.7% Strain

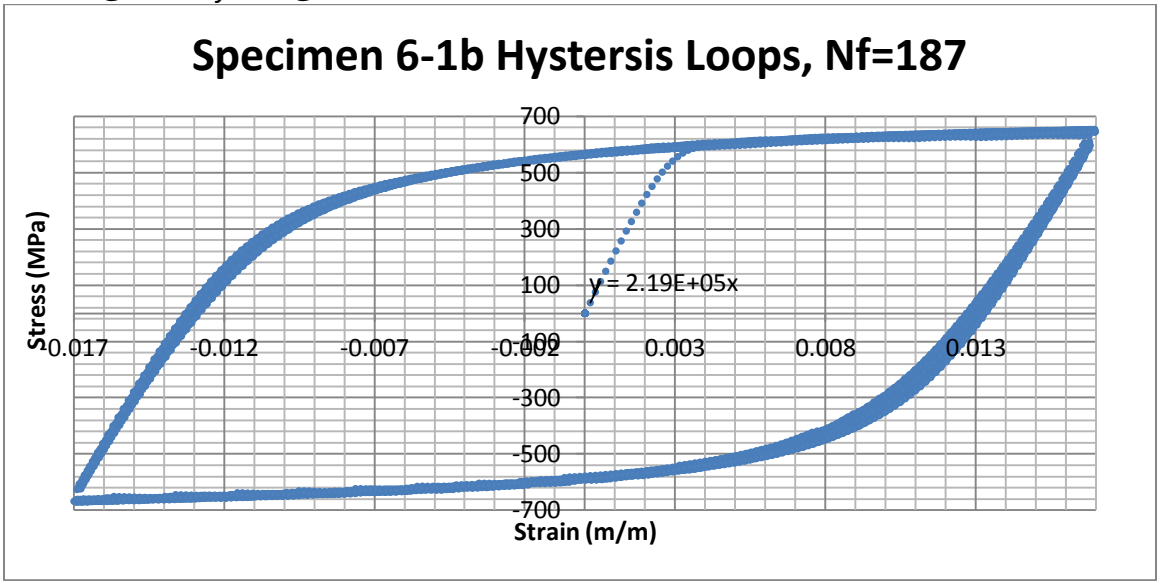

Young's Modulus per Cycle		
Cycle No.	**Compression Cycle (MPa)**	**Tension Cycle (MPa)**
1	1.83E+05	1.76E+05
2	1.74E+05	1.78E+05
3	1.78E+05	1.76E+05
4	1.77E+05	1.74E+05
5	1.77E+05	1.75E+05
6	1.81E+05	1.76E+05
7	1.84E+05	1.79E+05
8	1.84E+05	1.79E+05
9	1.83E+05	1.81E+05
19	1.90E+05	1.83E+05
29	1.90E+05	1.85E+05
39	1.89E+05	1.88E+05
49	1.90E+05	1.89E+05
59	1.92E+05	1.90E+05
69	1.91E+05	1.93E+05
79	1.92E+05	1.91E+05
89	1.90E+05	1.92E+05
99	1.91E+05	1.93E+05

Max Stress per Cycle				
Cycle No.	**Max (MPa)**	**Min (MPa)**	**Mean Stress (MPa)**	**Alt. Stress (MPa)**
1	649	-661	655	-6
2	652	-667	660	-8
3	653	-666	660	-6
4	654	-669	661	-7
5	652	-668	660	-8
6	652	-669	660	-8
7	652	-670	661	-9
8	652	-664	658	-6
9	651	-669	660	-9
19	651	-668	659	-9
29	651	-668	659	-9
39	650	-671	660	-11
49	649	-669	659	-10
59	648	-670	659	-11
69	648	-670	659	-11
79	646	-669	658	-11
89	645	-668	657	-12
99	645	-666	655	-10

Specimen No.6-2b (HR590)
Specimen Gage Dimensions: 0.126”x0.131”
Failure @ 175 Cycles @ 1.7% Strain

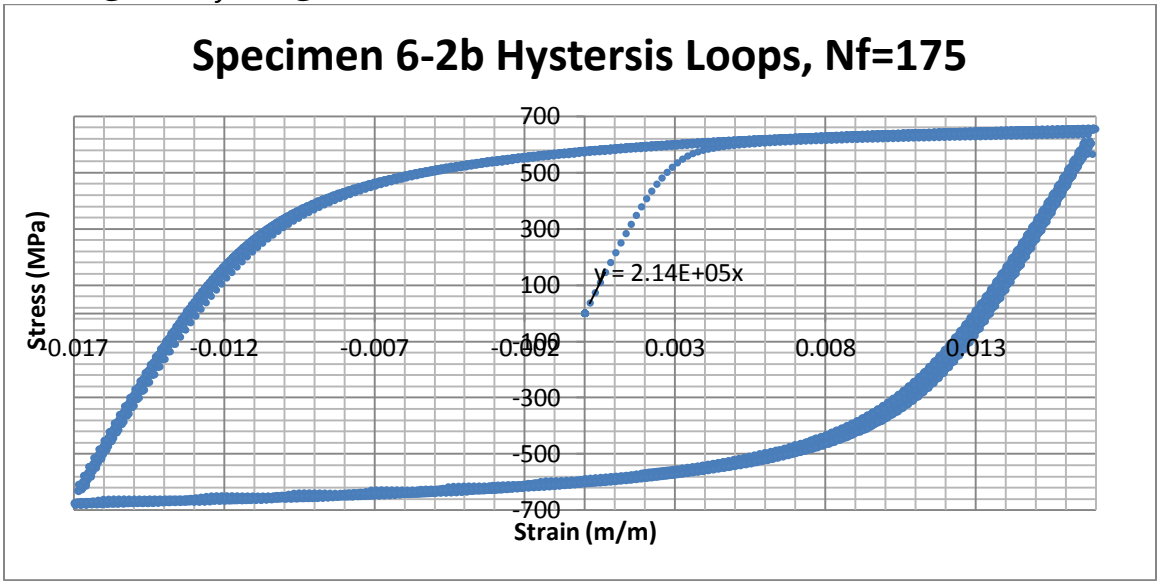

Young's Modulus per Cycle		
Cycle No.	**Compression Cycle (MPa)**	**Tension Cycle (MPa)**
1	1.91E+05	1.74E+05
2	1.81E+05	1.78E+05
3	1.78E+05	1.83E+05
4	1.80E+05	1.84E+05
5	1.78E+05	1.83E+05
6	1.78E+05	1.85E+05
7	1.79E+05	1.86E+05
8	1.81E+05	1.85E+05
9	1.82E+05	1.86E+05
19	1.85E+05	1.88E+05
29	1.88E+05	1.90E+05
39	1.90E+05	1.91E+05
49	1.94E+05	1.91E+05
59	1.93E+05	1.91E+05
69	1.92E+05	1.91E+05
79	1.94E+05	1.93E+05
89	1.93E+05	1.92E+05
99	1.94E+05	1.91E+05

Max Stress per Cycle				
Cycle No.	**Max (MPa)**	**Min (MPa)**	**Mean Stress (MPa)**	**Alt. Stress (MPa)**
1	652	-670	661	-9
2	655	-672	663	-9
3	655	-671	663	-8
4	655	-673	664	-9
5	656	-677	666	-11
6	656	-678	667	-11
7	656	-678	667	-11
8	656	-678	667	-11
9	655	-677	666	-11
19	656	-680	668	-12
29	657	-678	667	-11
39	658	-681	669	-11
49	658	-682	670	-12
59	656	-682	669	-13
69	656	-679	667	-11
79	655	-677	666	-11
89	653	-677	665	-12
99	650	-672	661	-11

Specimen No.5-1b (HR590)
Specimen Gage Dimensions: 0.126”x0.131”
Failure @ 281 Cycles @ 0.5% Strain

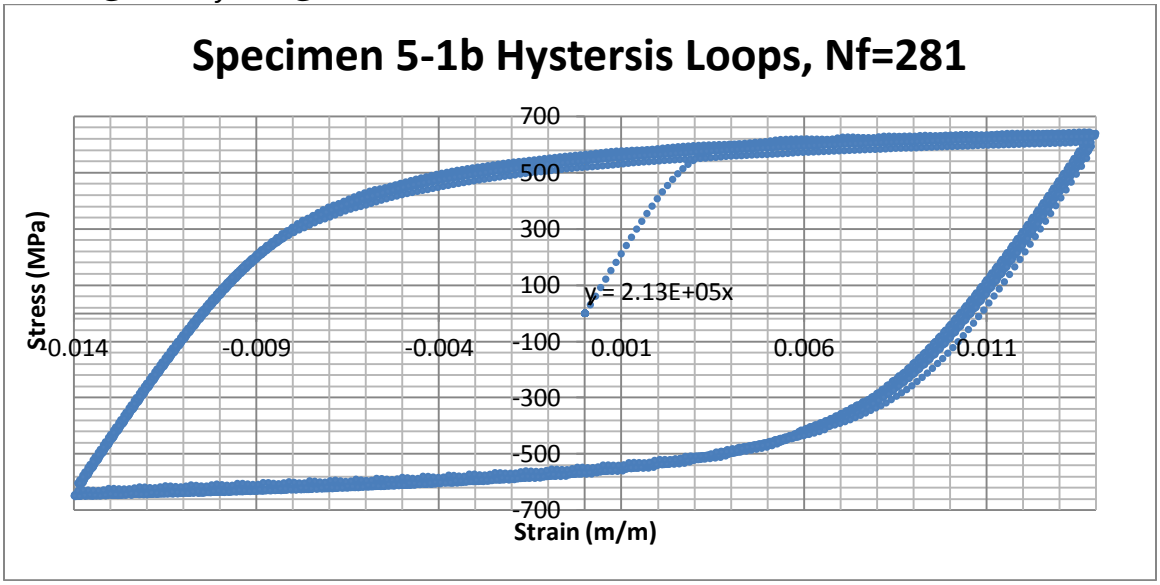

Young's Modulus per Cycle		
Cycle No.	**Compression Cycle (MPa)**	**Tension Cycle (MPa)**
1	1.92E+05	1.96E+05
2	1.88E+05	1.94E+05
3	1.89E+05	1.92E+05
4	1.88E+05	1.92E+05
5	1.87E+05	1.91E+05
6	1.88E+05	1.91E+05
7	1.88E+05	1.92E+05
8	1.88E+05	1.90E+05
9	1.87E+05	1.91E+05
19	1.89E+05	1.92E+05
29	1.88E+05	1.90E+05
39	1.89E+05	1.89E+05
49	1.89E+05	1.91E+05
59	1.89E+05	1.91E+05
69	1.90E+05	1.90E+05
79	1.90E+05	1.91E+05
89	1.89E+05	1.89E+05
99	1.92E+05	1.92E+05
199	2.00E+05	1.87E+05

Max Stress per Cycle				
Cycle No.	**Max (MPa)**	**Min (MPa)**	**Mean Stress (MPa)**	**Alt. Stress (MPa)**
1	644	-647	646	-1
2	644	-647	645	-1
3	639	-648	644	-4
4	640	-649	644	-5
5	637	-648	643	-5
6	638	-648	643	-5
7	635	-648	641	-7
8	636	-648	642	-6
9	633	-647	640	-7
19	633	-649	641	-8
29	632	-650	641	-9
39	631	-650	640	-10
49	631	-649	640	-9
59	632	-650	641	-9
69	631	-649	640	-9
79	631	-651	641	-10
89	630	-649	640	-9
99	630	-649	640	-10
199	607	-631	619	-12

Specimen No.5-2b (HR590)
Specimen Gage Dimensions: 0.126”x0.131”
Failure @ 369 Cycles @ 0.5% Strain

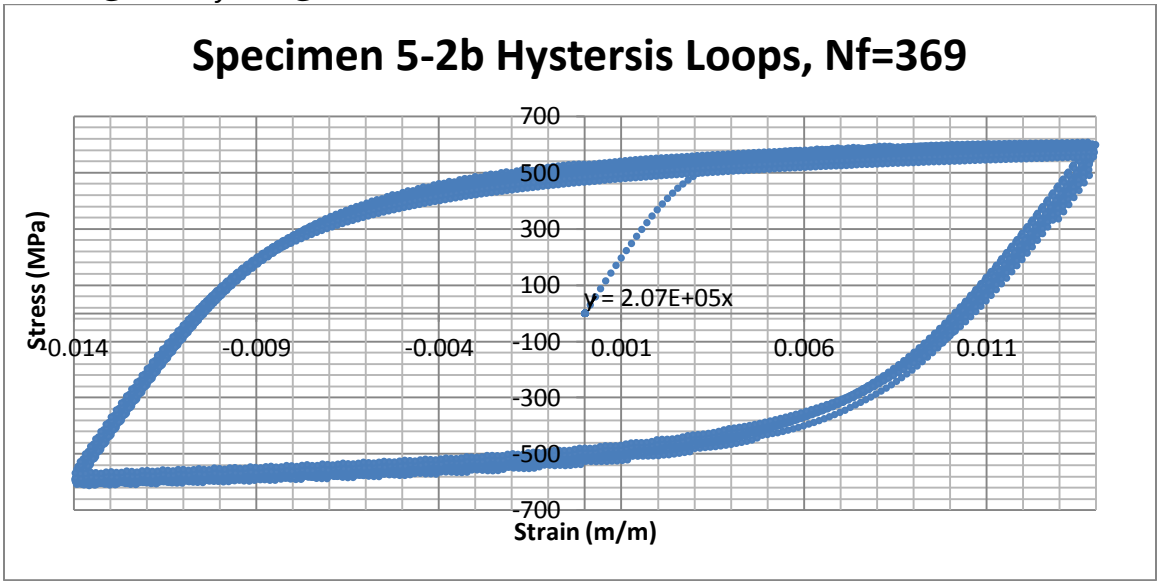

Young's Modulus per Cycle		
Cycle No.	**Compression Cycle (MPa)**	**Tension Cycle (MPa)**
1	1.84E+05	1.92E+05
2	1.79E+05	1.92E+05
3	1.80E+05	2.58E+05
4	1.79E+05	2.57E+05
5	1.79E+05	2.46E+05
6	1.78E+05	2.56E+05
7	1.80E+05	2.52E+05
8	1.81E+05	2.18E+05
9	1.81E+05	2.98E+05
19	1.82E+05	2.29E+05
29	1.83E+05	2.42E+05
39	1.87E+05	2.13E+05
49	1.86E+05	3.16E+05
59	1.84E+05	2.95E+05
69	1.87E+05	2.33E+05
79	1.85E+05	2.19E+05
89	1.88E+05	2.37E+05
99	1.88E+05	2.59E+05
199	1.92E+05	2.42E+05

Max Stress per Cycle				
Cycle No.	**Max (MPa)**	**Min (MPa)**	**Mean Stress (MPa)**	**Alt. Stress (MPa)**
1	608	-612	610	-2
2	608	-609	609	-1
3	601	-608	605	-4
4	601	-607	604	-3
5	599	-607	603	-4
6	596	-606	601	-5
7	594	-602	598	-4
8	591	-600	596	-4
9	591	-599	595	-4
19	585	-597	591	-6
29	582	-595	589	-7
39	580	-593	586	-6
49	579	-592	586	-7
59	577	-591	584	-7
69	576	-591	583	-7
79	575	-589	582	-7
89	573	-587	580	-7
99	572	-586	579	-7
199	556	-570	563	-7

Specimen No.5-3b
Specimen Gage Dimensions: 0.126”x0.130”
Failure @ 251 Cycles @ 1.4% Strain

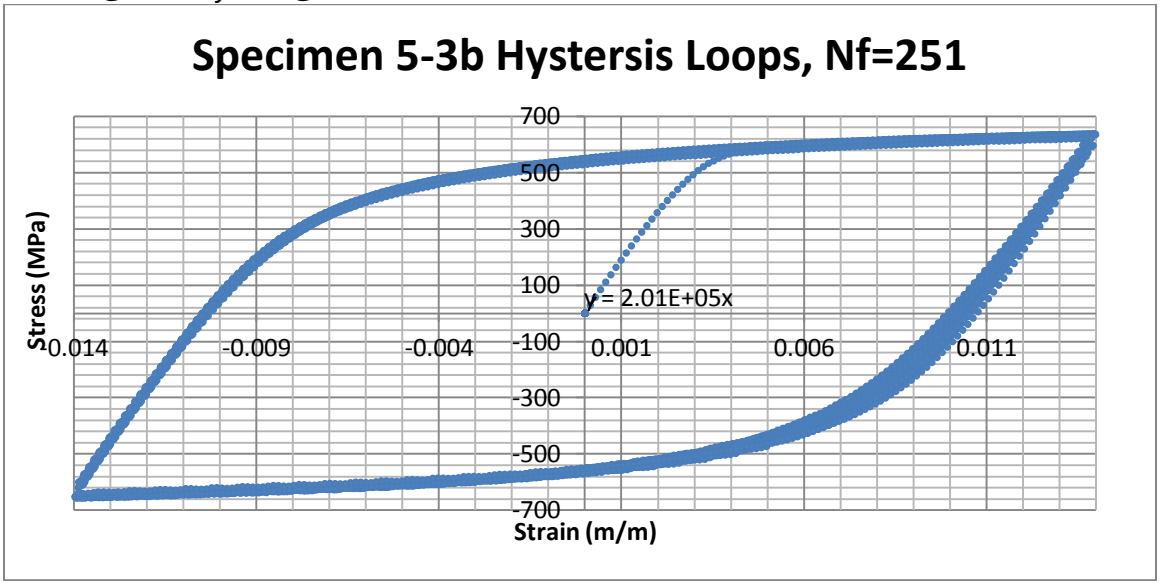

Young's Modulus per Cycle		
Cycle No.	**Compression Cycle (MPa)**	**Tension Cycle (MPa)**
1	1.96E+05	1.96E+05
2	1.78E+05	1.93E+05
3	1.75E+05	1.93E+05
4	1.76E+05	1.93E+05
5	1.72E+05	1.93E+05
6	1.72E+05	1.93E+05
7	1.72E+05	1.93E+05
8	1.73E+05	1.94E+05
9	1.71E+05	1.93E+05
19	1.75E+05	1.93E+05
29	1.86E+05	1.95E+05
39	1.89E+05	1.96E+05
49	1.91E+05	1.94E+05
59	1.91E+05	1.97E+05
69	1.90E+05	1.95E+05
79	1.92E+05	1.95E+05
89	1.93E+05	1.96E+05
99	1.93E+05	1.97E+05
199	2.00E+05	1.99E+05

Max Stress per Cycle				
Cycle No.	**Max (MPa)**	**Min (MPa)**	**Mean Stress (MPa)**	**Alt. Stress (MPa)**
1	636	-643	640	-4
2	637	-648	643	-5
3	636	-650	643	-7
4	637	-650	643	-7
5	636	-651	644	-7
6	636	-651	643	-8
7	635	-652	643	-8
8	635	-652	643	-8
9	634	-651	643	-9
19	635	-653	644	-9
29	635	-654	644	-9
39	637	-655	646	-9
49	637	-656	647	-9
59	637	-657	647	-10
69	637	-655	646	-9
79	637	-656	647	-10
89	637	-655	646	-9
99	636	-655	646	-10
199	622	-640	631	-9

Specimen No.5-4b (HR590)
Specimen Gage Dimensions: 0.125”x0.129”
Failure @ 175 Cycles @ 1.4% Strain

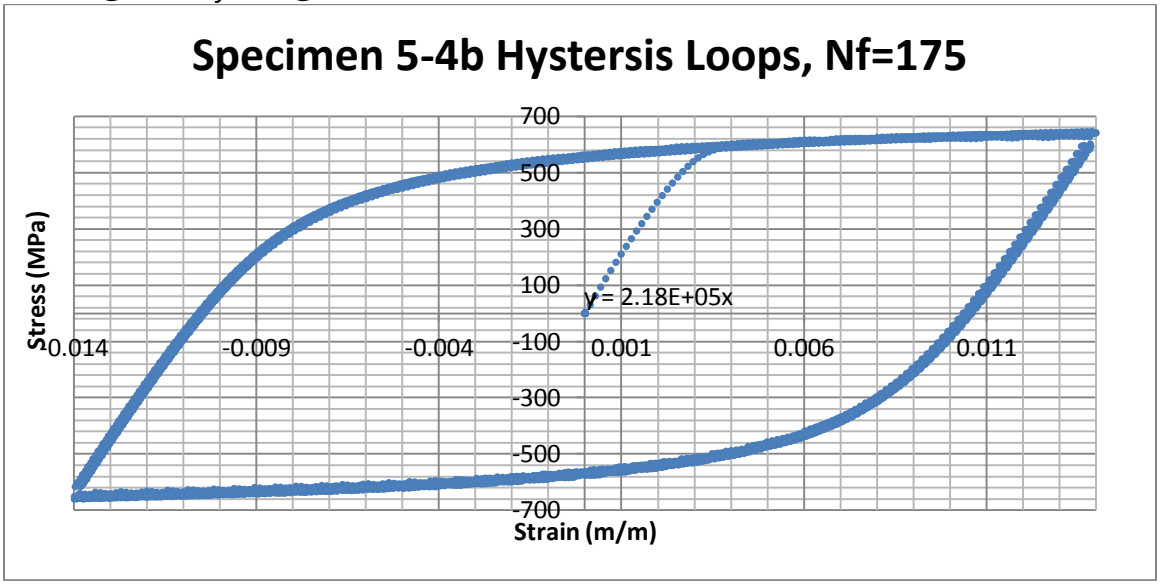

Young's Modulus per Cycle

Cycle No.	Compression Cycle (MPa)	Tension Cycle (MPa)
1	2.01E+05	2.02E+05
2	1.94E+05	2.01E+05
3	1.96E+05	2.00E+05
4	1.94E+05	1.99E+05
5	1.93E+05	2.00E+05
6	1.95E+05	1.98E+05
7	1.94E+05	1.99E+05
8	1.92E+05	1.99E+05
9	1.94E+05	1.99E+05
19	1.94E+05	1.96E+05
29	1.92E+05	1.97E+05
39	1.93E+05	1.98E+05
49	1.96E+05	1.96E+05
59	1.95E+05	1.98E+05
69	1.95E+05	1.97E+05
79	1.96E+05	1.97E+05
89	1.95E+05	1.97E+05
99	1.94E+05	1.97E+05

Max Stress per Cycle

Cycle No.	Max (MPa)	Min (MPa)	Mean Stress (MPa)	Alt. Stress (MPa)
1	640	-643	642	-2
2	644	-648	646	-2
3	644	-650	647	-3
4	643	-652	648	-4
5	642	-653	647	-6
6	642	-653	647	-6
7	641	-653	647	-6
8	642	-653	647	-5
9	642	-654	648	-6
19	641	-655	648	-7
29	639	-657	648	-9
39	641	-658	650	-9
49	641	-658	649	-8
59	641	-659	650	-9
69	641	-660	651	-10
79	640	-659	649	-10
89	638	-657	648	-9
99	646	-657	651	-5

Specimen No.4-1b (HR590)
Specimen Gage Dimensions: 0.126”x0.133”
Failure @ 316 Cycles @ 1.1 % Strain

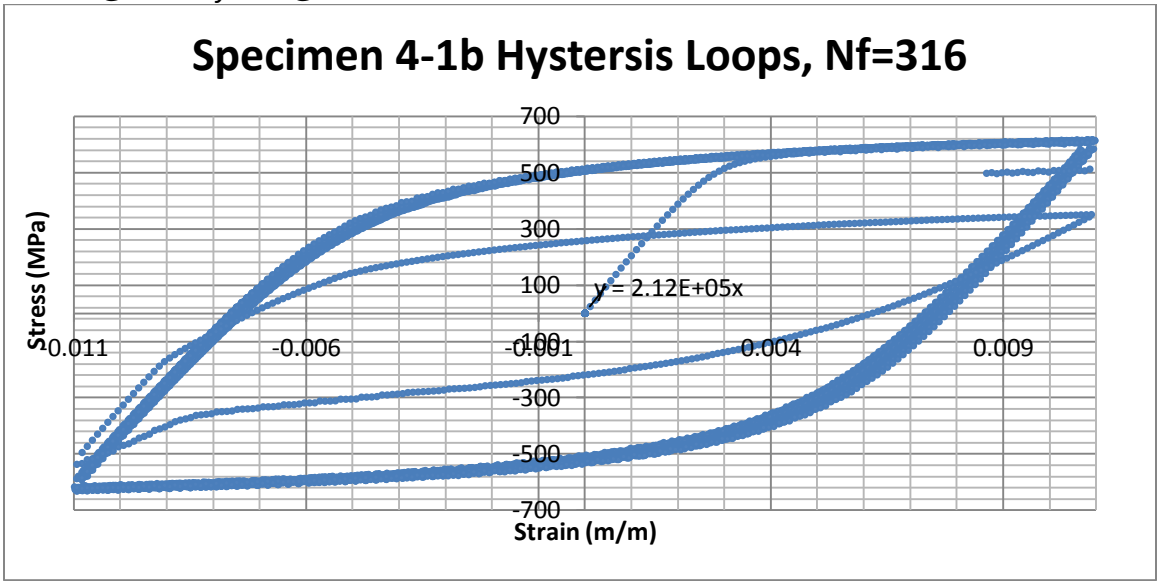

Young's Modulus per Cycle		
Cycle No.	**Compression Cycle (MPa)**	**Tension Cycle (MPa)**
1	2.00E+05	1.79E+05
2	1.92E+05	1.83E+05
3	1.87E+05	1.85E+05
4	1.87E+05	1.87E+05
5	1.85E+05	1.88E+05
6	1.85E+05	1.88E+05
7	1.85E+05	1.88E+05
8	1.87E+05	1.87E+05
9	1.84E+05	1.90E+05
19	1.90E+05	1.92E+05
29	1.90E+05	1.93E+05
39	1.92E+05	1.95E+05
49	1.93E+05	1.94E+05
59	1.93E+05	1.95E+05
69	1.95E+05	1.95E+05
79	1.94E+05	1.95E+05
89	1.96E+05	1.96E+05
99	1.96E+05	1.95E+05
199	2.00E+05	1.93E+05
299	#DIV/0!	1.98E+05

Max Stress per Cycle				
Cycle No.	**Max (MPa)**	**Min (MPa)**	**Mean Stress (MPa)**	**Alt. Stress (MPa)**
1	614	-621	617	-3
2	614	-622	618	-4
3	614	-621	617	-4
4	614	-623	619	-4
5	615	-624	619	-5
6	615	-625	620	-5
7	614	-624	619	-5
8	615	-623	619	-4
9	614	-622	618	-4
19	614	-625	620	-6
29	614	-627	621	-6
39	615	-628	621	-7
49	615	-629	622	-7
59	616	-630	623	-7
69	616	-629	622	-6
79	616	-631	624	-7
89	616	-631	624	-8
99	617	-628	622	-6
199	610	-623	616	-6
299	512	-537	525	-12

Specimen No.4-2b (HR590)
Specimen Gage Dimensions: 0.126”x0.131”
Failure @ 380 Cycles @ 1.1% Strain

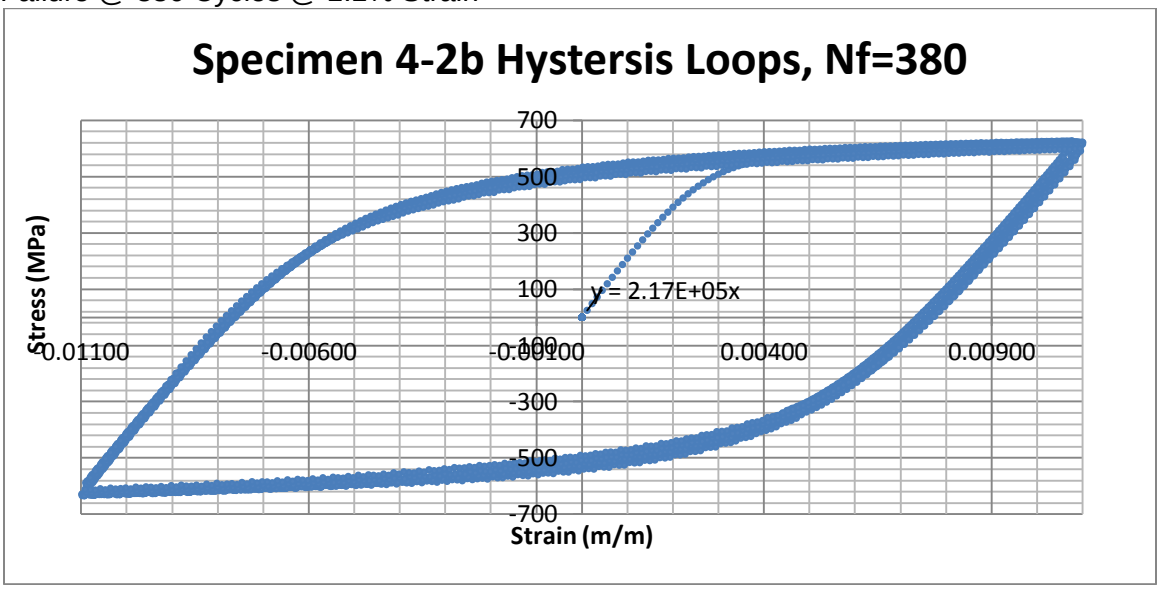

Young's Modulus per Cycle		
Cycle No.	**Compression Cycle (MPa)**	**Tension Cycle (MPa)**
1	1.99E+05	2.05E+05
2	1.92E+05	2.01E+05
3	1.91E+05	1.99E+05
4	1.92E+05	1.99E+05
5	1.92E+05	2.00E+05
6	1.91E+05	1.98E+05
7	1.91E+05	1.98E+05
8	1.90E+05	1.99E+05
9	1.91E+05	1.98E+05
19	1.91E+05	1.96E+05
29	1.94E+05	1.98E+05
39	1.92E+05	1.97E+05
49	1.94E+05	1.98E+05
59	1.95E+05	1.97E+05
69	1.95E+05	1.98E+05
79	1.94E+05	1.97E+05
89	1.95E+05	1.98E+05
99	1.97E+05	1.97E+05
199	1.99E+05	1.98E+05
299	1.98E+05	1.96E+05

Max Stress per Cycle				
Cycle No.	**Max (MPa)**	**Min (MPa)**	**Mean Stress (MPa)**	**Alt. Stress (MPa)**
1	628	-627	627	1
2	626	-627	627	0
3	625	-627	626	-1
4	624	-628	626	-2
5	623	-629	626	-3
6	623	-629	626	-3
7	622	-629	625	-3
8	623	-629	626	-3
9	621	-628	624	-4
19	618	-630	624	-6
29	617	-631	624	-7
39	617	-632	624	-8
49	617	-632	624	-8
59	617	-633	625	-8
69	617	-634	625	-8
79	616	-634	625	-9
89	617	-634	625	-8
99	616	-633	625	-8
199	611	-624	618	-7
299	600	-614	607	-7

Specimen No.4-3b (HR590)
Specimen Gage Dimensions: 0.126”x0.131”
Failure @ 474 Cycles @ 1.1% Strain

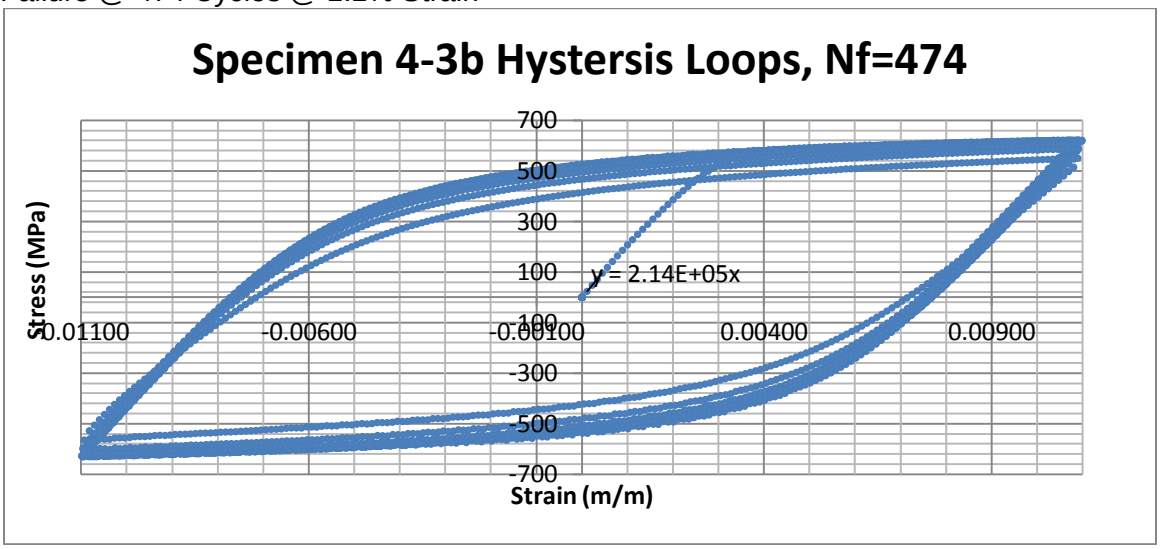

Young's Modulus per Cycle		
Cycle No.	**Compression Cycle (MPa)**	**Tension Cycle (MPa)**
1	1.99E+05	2.01E+05
2	1.93E+05	1.98E+05
3	1.92E+05	1.96E+05
4	1.91E+05	1.96E+05
5	1.92E+05	1.95E+05
6	1.90E+05	1.95E+05
7	1.90E+05	1.96E+05
8	1.91E+05	1.95E+05
9	1.92E+05	1.94E+05
19	1.92E+05	1.95E+05
29	1.90E+05	1.94E+05
39	1.91E+05	1.93E+05
49	1.92E+05	1.92E+05
59	1.90E+05	1.93E+05
69	1.93E+05	1.94E+05
79	1.93E+05	1.92E+05
89	1.92E+05	1.93E+05
99	1.93E+05	1.93E+05
199	1.88E+05	1.95E+05
299	1.80E+05	1.97E+05
399	1.56E+05	1.98E+05

Max Stress per Cycle				
Cycle No.	**Max (MPa)**	**Min (MPa)**	**Mean Stress (MPa)**	**Alt. Stress (MPa)**
1	621	-622	622	-1
2	621	-625	623	-2
3	622	-625	623	-2
4	622	-627	625	-2
5	622	-627	624	-2
6	622	-628	625	-3
7	621	-628	624	-4
8	620	-627	624	-4
9	620	-627	624	-3
19	619	-630	624	-5
29	618	-630	624	-6
39	618	-630	624	-6
49	619	-630	625	-5
59	619	-630	624	-6
69	619	-630	624	-6
79	618	-630	624	-6
89	617	-630	624	-7
99	618	-630	624	-6
199	606	-620	613	-7
299	588	-603	595	-8
399	550	-566	558	-8

Specimen No.3-1b (HR590)
Specimen Gage Dimensions: 0.126”x0.132”
Failure @ 1118 Cycles @ 0.8% Strain

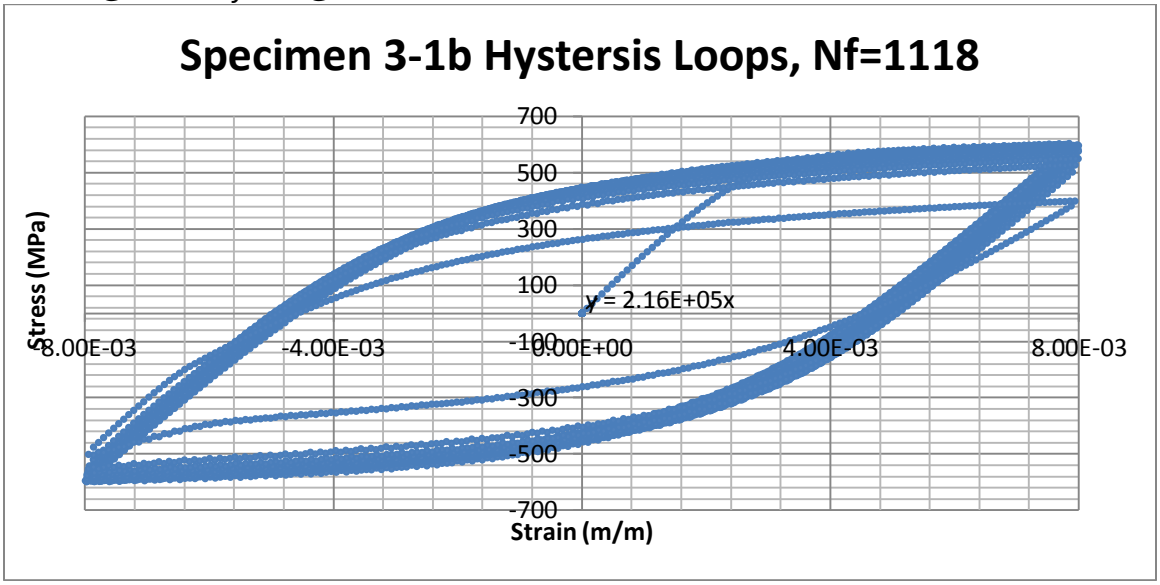

Young's Modulus per Cycle		
Cycle No.	**Compression Cycle (MPa)**	**Tension Cycle (MPa)**
4	1.89E+05	1.89E+05
9	1.88E+05	1.89E+05
19	1.91E+05	1.92E+05
29	1.91E+05	1.92E+05
39	1.91E+05	1.92E+05
49	1.91E+05	1.94E+05
59	1.92E+05	1.95E+05
69	1.93E+05	1.95E+05
79	1.94E+05	1.95E+05
89	1.94E+05	1.95E+05
99	1.91E+05	1.94E+05
299	1.95E+05	1.96E+05
599	2.00E+05	1.98E+05
699	2.01E+05	1.99E+05
799	2.02E+05	2.03E+05
899	1.93E+05	2.04E+05
999	#DIV/0!	2.03E+05

Max Stress per Cycle				
Cycle No.	**Max (MPa)**	**Min (MPa)**	**Mean Stress (MPa)**	**Alt. Stress (MPa)**
4	598	-593	595	2
9	595	-593	594	1
19	590	-593	591	-1
29	589	-593	591	-2
39	587	-595	591	-4
49	588	-595	591	-3
59	587	-596	591	-4
69	587	-596	591	-4
79	587	-598	593	-5
89	589	-598	593	-5
99	587	-598	592	-5
299	582	-594	588	-6
599	565	-581	573	-8
699	558	-576	567	-9
799	550	-567	558	-8
899	528	-553	540	-12
999	399	-504	451	-52

Specimen No.3-2b (HR590)
Specimen Gage Dimensions: 0.126”x0.131”
Failure @ 1097 Cycles @ 0.8% Strain

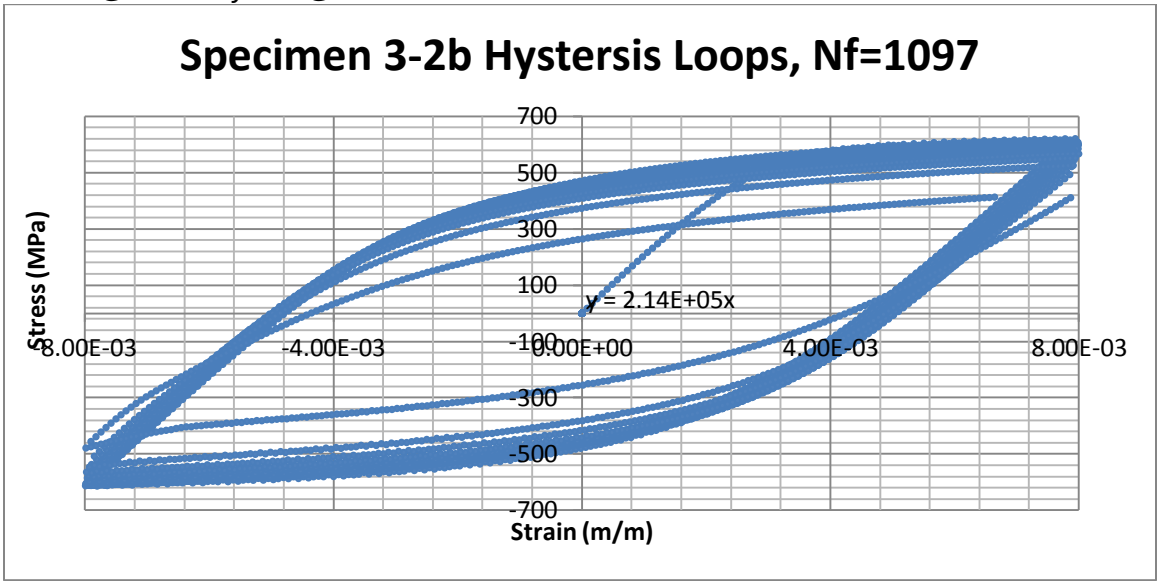

Young's Modulus per Cycle		
Cycle No.	**Compression Cycle (MPa)**	**Tension Cycle (MPa)**
4	1.98E+05	2.09E+05
9	1.96E+05	2.07E+05
19	1.98E+05	2.06E+05
29	2.00E+05	2.05E+05
39	1.99E+05	2.06E+05
49	2.01E+05	2.07E+05
59	2.01E+05	2.04E+05
69	2.01E+05	2.06E+05
79	2.01E+05	2.04E+05
89	2.02E+05	2.07E+05
99	2.02E+05	2.04E+05
299	2.04E+05	2.06E+05
599	2.04E+05	2.10E+05
699	2.05E+05	2.08E+05
799	2.03E+05	2.12E+05
899	1.79E+05	2.10E+05
999	#DIV/0!	#DIV/0!

Max Stress per Cycle				
Cycle No.	**Max (MPa)**	**Min (MPa)**	**Mean Stress (MPa)**	**Alt. Stress (MPa)**
4	611	-610	611	1
9	605	-611	608	-3
19	603	-611	607	-4
29	601	-611	606	-5
39	600	-611	606	-5
49	600	-610	605	-5
59	600	-610	605	-5
69	599	-611	605	-6
79	599	-612	605	-7
89	598	-613	606	-7
99	599	-611	605	-6
299	591	-607	599	-8
599	574	-590	582	-8
699	567	-581	574	-7
799	552	-567	559	-8
899	526	-547	536	-10
999	430	-479	454	-24

Specimen No.2-1b (HR590)
Specimen Gage Dimensions: 0.125”x0.132”
Failure @ 4037 Cycles @ 0.5% Strain @0.005in/in/s

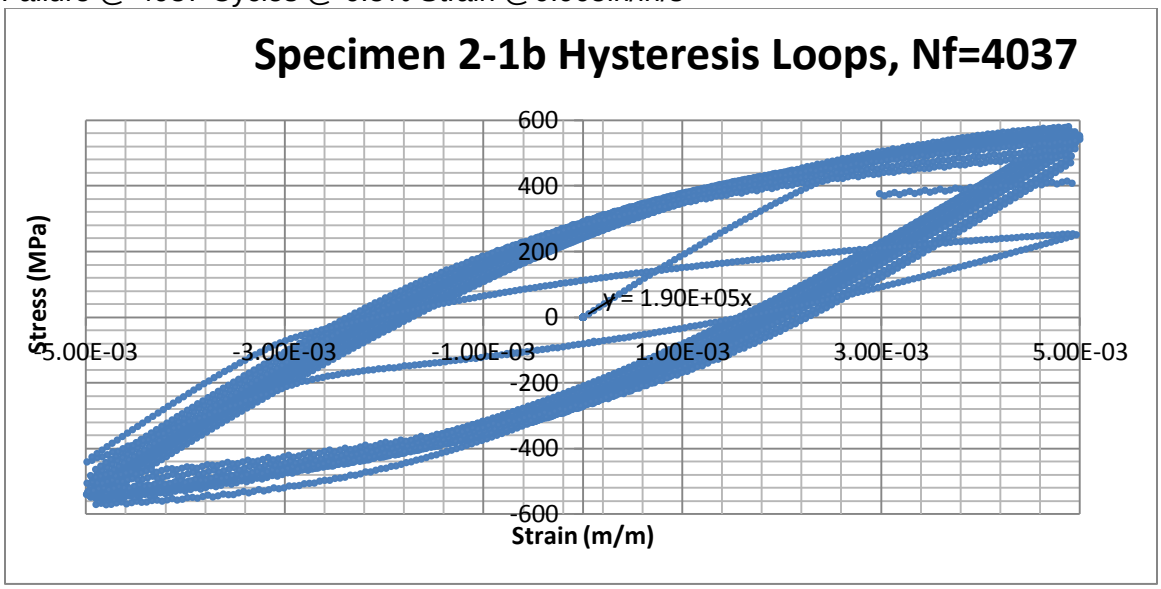

Young's Modulus per Cycle		
Cycle No.	**Compression Cycle (MPa)**	**Tension Cycle (MPa)**
4	1.84E+05	1.86E+05
9	1.81E+05	1.87E+05
19	1.81E+05	1.89E+05
29	1.81E+05	1.87E+05
39	1.81E+05	1.88E+05
49	1.84E+05	1.89E+05
59	1.83E+05	1.89E+05
69	1.83E+05	1.89E+05
79	1.84E+05	1.89E+05
89	1.83E+05	1.91E+05
99	1.82E+05	1.91E+05
299	1.86E+05	1.92E+05
599	1.88E+05	1.94E+05
699	1.88E+05	1.94E+05
799	1.87E+05	1.95E+05
899	1.89E+05	1.95E+05
999	1.89E+05	1.96E+05
1999	1.92E+05	2.00E+05
2999	1.92E+05	2.01E+05
3999	#DIV/0!	2.06E+05

Max Stress per Cycle				
Cycle No.	**Max (MPa)**	**Min (MPa)**	**Mean Stress (MPa)**	**Alt. Stress (MPa)**
4	567	-552	560	8
9	560	-548	554	6
19	554	-539	547	7
29	553	-539	546	7
39	550	-540	545	5
49	551	-539	545	6
59	548	-540	544	4
69	549	-540	545	4
79	551	-538	545	7
89	548	-539	543	4
99	549	-540	544	5
299	549	-541	545	4
599	545	-538	541	4
699	543	-537	540	3
799	541	-533	537	4
899	538	-533	536	3
999	537	-531	534	3
1999	514	-506	510	4
2999	495	-488	491	4
3999	414	-441	428	-14

Specimen No.2-2b (HR590)
Specimen Gage Dimensions: 0.127”x0.129”
Failure @ 3272 Cycles @ 0.5% Strain

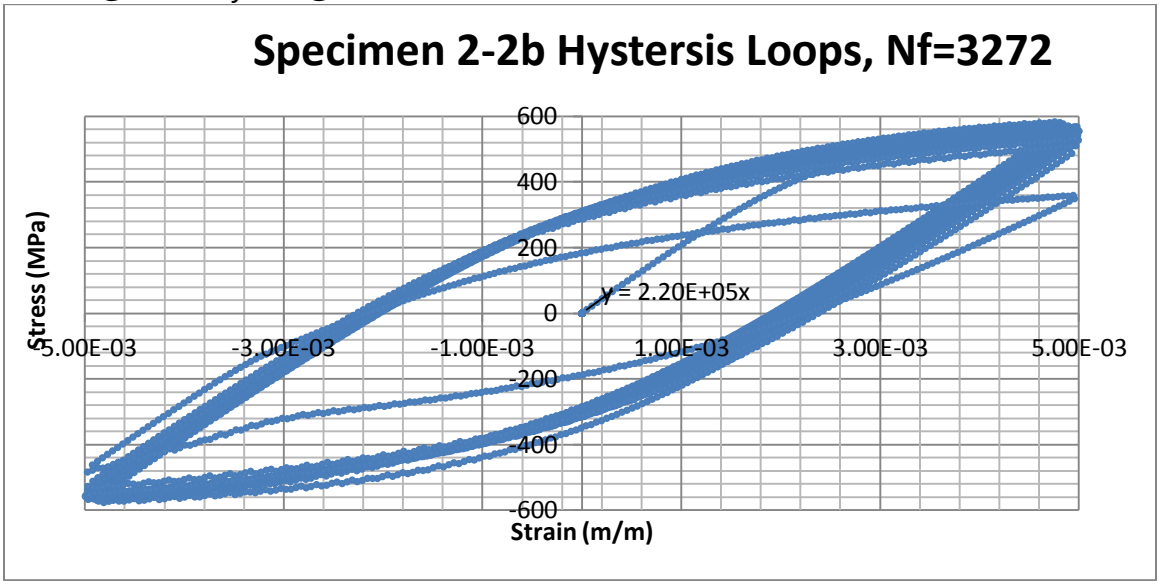

Young's Modulus per Cycle

Cycle No.	Compression Cycle (MPa)	Tension Cycle (MPa)
4	2.00E+05	2.03E+05
9	1.98E+05	2.02E+05
19	1.97E+05	2.01E+05
29	1.97E+05	2.01E+05
39	1.97E+05	2.03E+05
49	1.97E+05	2.02E+05
59	1.97E+05	2.02E+05
69	1.97E+05	2.02E+05
79	1.97E+05	2.04E+05
89	1.97E+05	2.03E+05
99	1.98E+05	2.02E+05
299	1.98E+05	2.02E+05
599	1.98E+05	2.02E+05
699	1.99E+05	2.03E+05
799	2.00E+05	2.03E+05
899	2.02E+05	2.03E+05
999	1.99E+05	2.03E+05
1999	2.04E+05	2.06E+05
2999	#DIV/0!	2.10E+05

Max Stress per Cycle

Cycle No.	Max (MPa)	Min (MPa)	Mean Stress (MPa)	Alt. Stress (MPa)
4	572	-568	570	2
9	568	-563	565	2
19	560	-559	560	0
29	556	-558	557	-1
39	555	-560	557	-2
49	556	-559	557	-2
59	556	-558	557	-1
69	553	-558	555	-2
79	555	-560	558	-3
89	552	-560	556	-4
99	551	-556	554	-3
299	547	-561	554	-7
599	542	-559	550	-8
699	538	-556	547	-9
799	535	-557	546	-11
899	533	-555	544	-11
999	532	-553	542	-10
1999	510	-532	521	-11
2999	362	-483	423	-61

Specimen 1_5-2b (HR590)
Specimen Gage Dimensions: 0.130”x0.126”
Failure @ 10130 Cycles @ 0.35% Strain

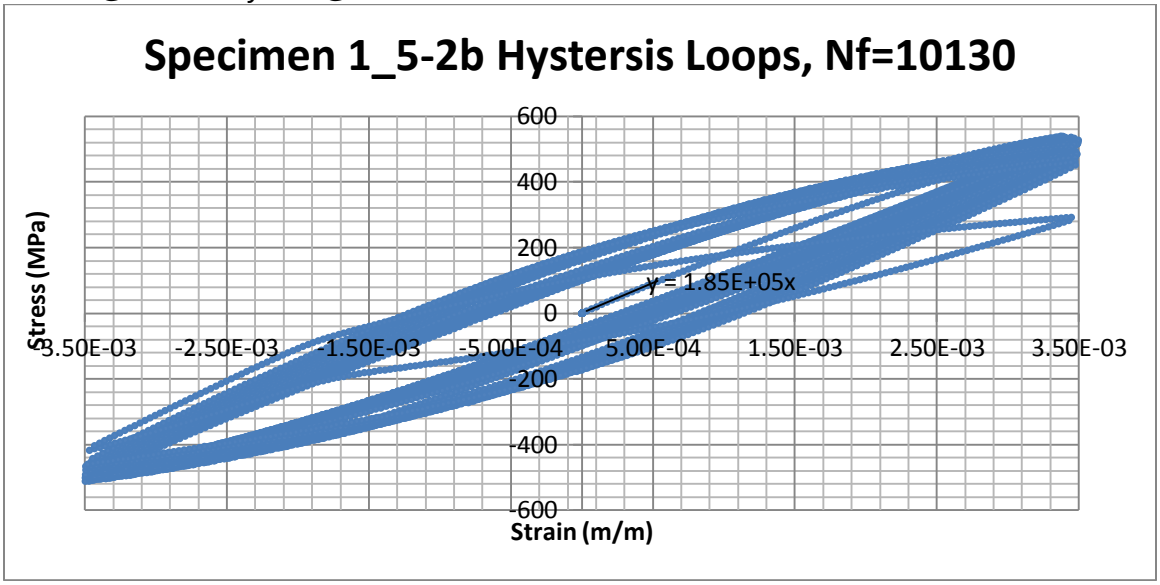

Young's Modulus per Cycle

Cycle No.	Compression Cycle (MPa)	Tension Cycle (MPa)
4	1.74E+05	1.87E+05
9	1.73E+05	1.87E+05
19	1.76E+05	1.90E+05
39	1.82E+05	1.95E+05
59	1.87E+05	1.97E+05
79	1.92E+05	2.03E+05
99	1.96E+05	2.04E+05
399	2.01E+05	2.07E+05
699	2.00E+05	2.08E+05
999	2.01E+05	2.07E+05
3999	2.05E+05	2.11E+05
6999	2.08E+05	2.16E+05

Max Stress per Cycle

Cycle No.	Max (MPa)	Min (MPa)	Mean Stress (MPa)	Alt. Stress (MPa)
4	537	-487	512	25
9	533	-487	510	23
19	528	-489	508	19
39	515	-485	500	15
59	517	-493	505	12
79	517	-490	504	14
99	520	-490	505	15
399	525	-509	517	8
699	522	-512	517	5
999	520	-504	512	8
3999	498	-491	495	3
6999	484	-471	478	7

Specimen 1_5-3b (HR590)
Specimen Gage Dimensions: 0.130”x0.125”
Failure @ 9292 Cycles @ 0.35% Strain

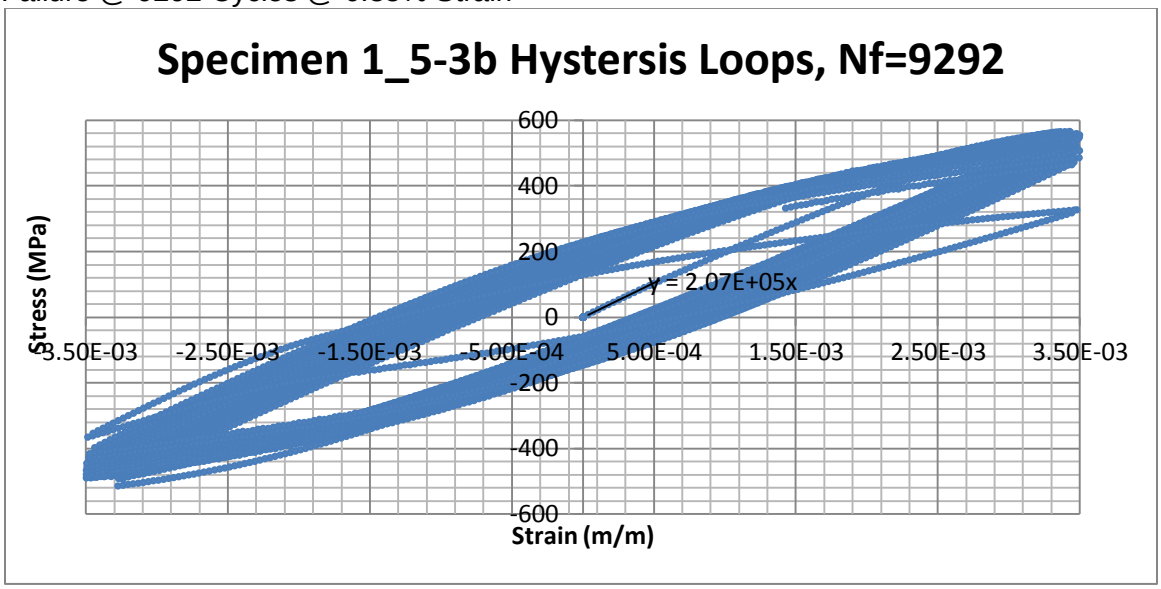

Young's Modulus per Cycle		
Cycle No.	**Compression Cycle (MPa)**	**Tension Cycle (MPa)**
4	1.92E+05	2.08E+05
9	1.92E+05	2.08E+05
19	1.94E+05	2.07E+05
39	1.96E+05	2.07E+05
59	1.94E+05	2.08E+05
79	1.97E+05	2.10E+05
99	1.97E+05	2.10E+05
399	2.05E+05	2.12E+05
699	2.04E+05	2.14E+05
999	2.07E+05	2.15E+05
3999	2.08E+05	2.20E+05
6999	2.09E+05	2.54E+05
7999	2.03E+05	2.80E+05

Max Stress per Cycle				
Cycle No.	**Max (MPa)**	**Min (MPa)**	**Mean Stress (MPa)**	**Alt. Stress (MPa)**
4	563	-486	525	39
9	564	-485	525	39
19	559	-481	520	39
39	551	-479	515	36
59	549	-479	514	35
79	548	-479	513	35
99	549	-481	515	34
399	551	-487	519	32
699	549	-489	519	30
999	554	-487	520	33
3999	524	-456	490	34
6999	514	-428	471	43
7999	485	-416	451	35

Specimen 1_3-1b (HR590)
Specimen Gage Dimensions: 0.129”x0.126”
Failure @ 19158 Cycles @ 0.29% Strain

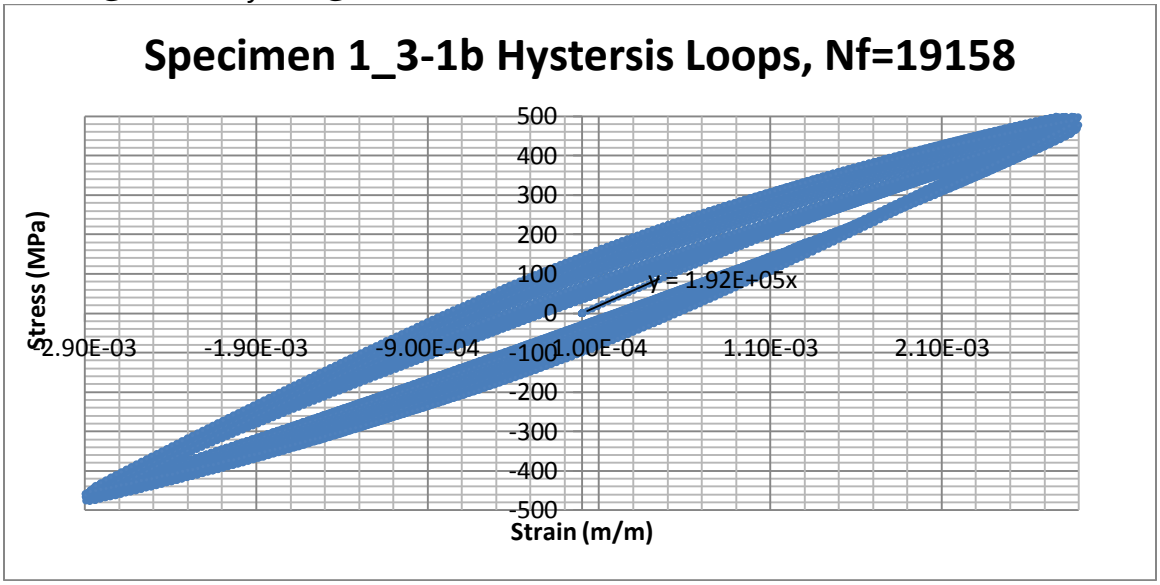

Young's Modulus per Cycle		
Cycle No.	**Compression Cycle (MPa)**	**Tension Cycle (MPa)**
4	2.00E+05	2.06E+05
9	1.98E+05	2.04E+05
19	1.97E+05	2.05E+05
39	1.99E+05	2.08E+05
59	2.01E+05	2.11E+05
79	2.05E+05	2.15E+05
99	2.05E+05	2.14E+05
399	2.10E+05	2.21E+05
699	2.12E+05	2.18E+05
999	2.13E+05	2.20E+05
3999	2.13E+05	2.25E+05
6999	2.16E+05	2.27E+05
9999	2.16E+05	2.28E+05

Max Stress per Cycle				
Cycle No.	**Max (MPa)**	**Min (MPa)**	**Mean Stress (MPa)**	**Alt. Stress (MPa)**
4	446	-449	448	-2
9	460	-454	457	3
19	465	-456	460	5
39	469	-454	462	8
59	471	-454	463	9
79	477	-455	466	11
99	474	-458	466	8
399	495	-460	477	17
699	502	-476	489	13
999	507	-473	490	17
3999	508	-476	492	16
6999	502	-458	480	22
9999	489	-452	471	18

Specimen 1_1-1b (HR590)
Specimen Gage Dimensions: 0.129”x0.126”
Failure @ 61849 Cycles @ 0.23% Strain

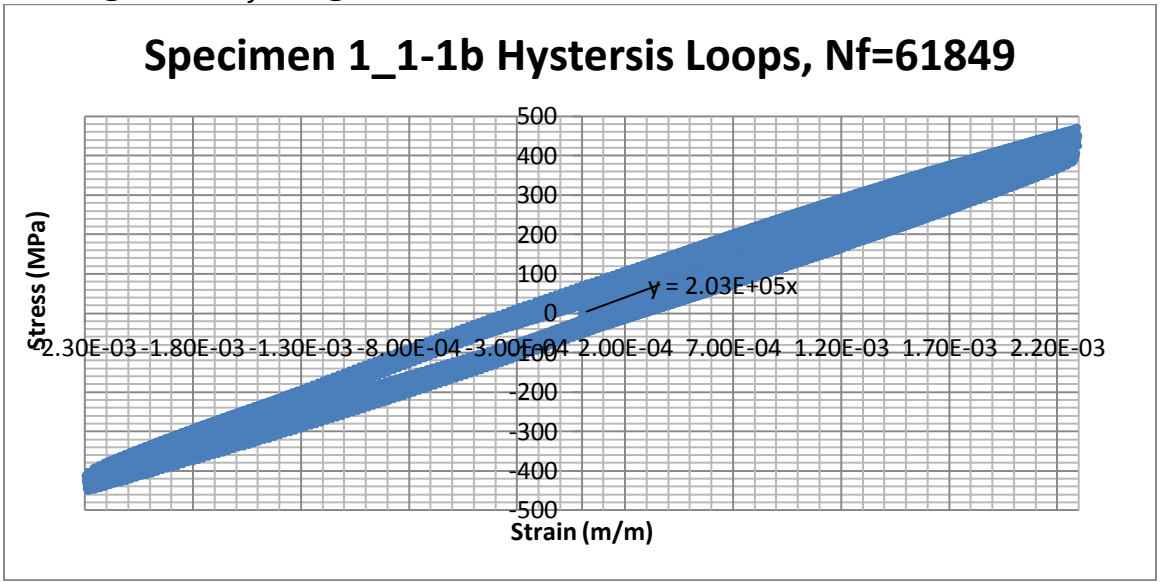

Young's Modulus per Cycle

Cycle No.	Compression Cycle (MPa)	Tension Cycle (MPa)
4	2.10E+05	2.10E+05
9	2.08E+05	2.10E+05
19	2.13E+05	2.14E+05
39	2.15E+05	2.17E+05
59	2.13E+05	2.17E+05
79	2.14E+05	2.16E+05
99	2.14E+05	2.18E+05
399	2.12E+05	2.18E+05
699	2.11E+05	2.17E+05
999	2.11E+05	2.17E+05
3999	2.12E+05	2.17E+05
6999	2.14E+05	2.17E+05
9999	2.12E+05	2.16E+05
19999	2.12E+05	2.17E+05
29999	2.12E+05	2.17E+05
39999	2.11E+05	2.17E+05
49999	2.12E+05	2.18E+05
59999	2.04E+05	2.19E+05

Max Stress per Cycle

Cycle No.	Max (MPa)	Min (MPa)	Mean Stress (MPa)	Alt. Stress (MPa)
4	372	-384	378	-6
9	377	-391	384	-7
19	383	-402	392	-9
39	390	-410	400	-10
59	395	-412	404	-8
79	400	-416	408	-8
99	406	-419	413	-6
399	458	-430	444	14
699	468	-424	446	22
999	472	-424	448	24
3999	447	-452	449	-2
6999	445	-446	446	0
9999	455	-436	445	9
19999	423	-450	437	-14
29999	430	-435	433	-3
39999	437	-420	429	8
49999	437	-411	424	13
59999	425	-389	407	18

Specimen No.1-1b (HR590)
Specimen Gage Dimensions: 0.126”x0.129”
Failure @ 132143 Cycles @ 0.2% Strain

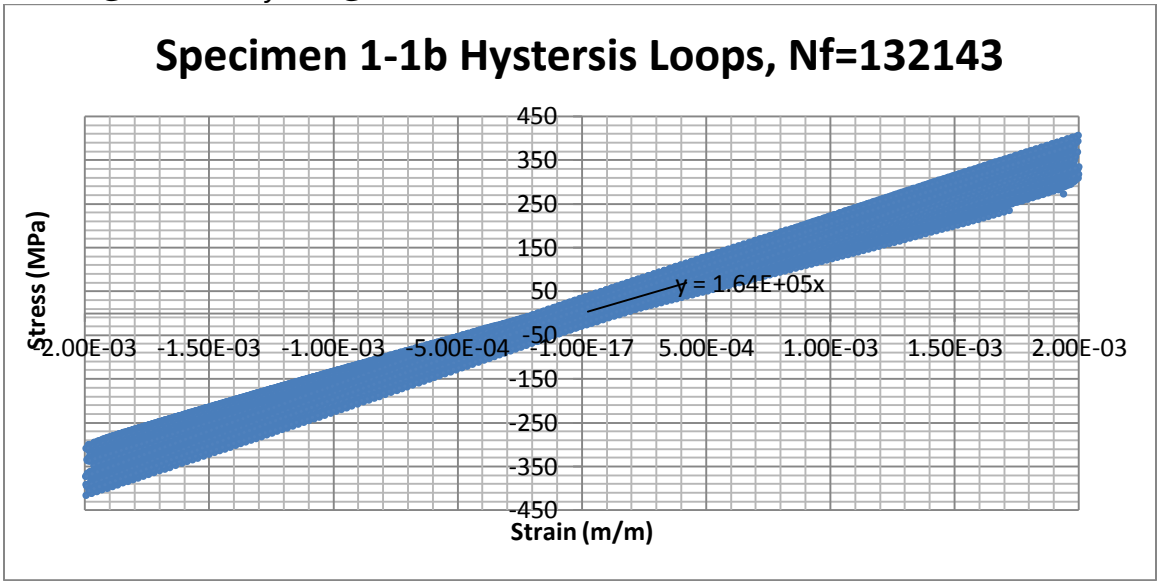

Young's Modulus per Cycle

Cycle No.	Compression Cycle (MPa)	Tension Cycle (MPa)
4	1.72E+05	1.76E+05
9	1.72E+05	1.75E+05
19	1.72E+05	1.72E+05
39	1.73E+05	1.73E+05
59	1.73E+05	1.73E+05
79	1.74E+05	1.74E+05
99	1.72E+05	1.73E+05
399	1.73E+05	1.73E+05
699	1.74E+05	1.74E+05
999	1.72E+05	1.75E+05
3999	1.95E+05	1.98E+05
6999	2.00E+05	2.03E+05
9999	2.03E+05	2.08E+05
19999	2.07E+05	2.09E+05
39999	2.06E+05	2.13E+05
59999	2.08E+05	2.10E+05
79999	2.07E+05	2.11E+05
99999	2.07E+05	2.11E+05

Max Stress per Cycle

Cycle No.	Max (MPa)	Min (MPa)	Mean Stress (MPa)	Alt. Stress (MPa)
4	286	-288	287	-1
9	296	-292	294	2
19	301	-300	300	1
39	309	-300	304	5
59	311	-304	307	3
79	309	-312	310	-1
99	318	-313	316	2
399	328	-328	328	0
699	333	-334	334	-1
999	330	-341	336	-6
3999	349	-372	361	-12
6999	373	-367	370	3
9999	393	-372	383	11
19999	396	-383	389	7
29999	404	-391	398	7
39999	390	-402	396	-6
49999	385	-416	400	-16
59999	399	-396	397	2

Specimen 1-4b
Specimen Gage Dimensions: 0.124”x0.131”
Failure @102048
Offset 20,000=-0.0008
Offset 60,000=-0.0006

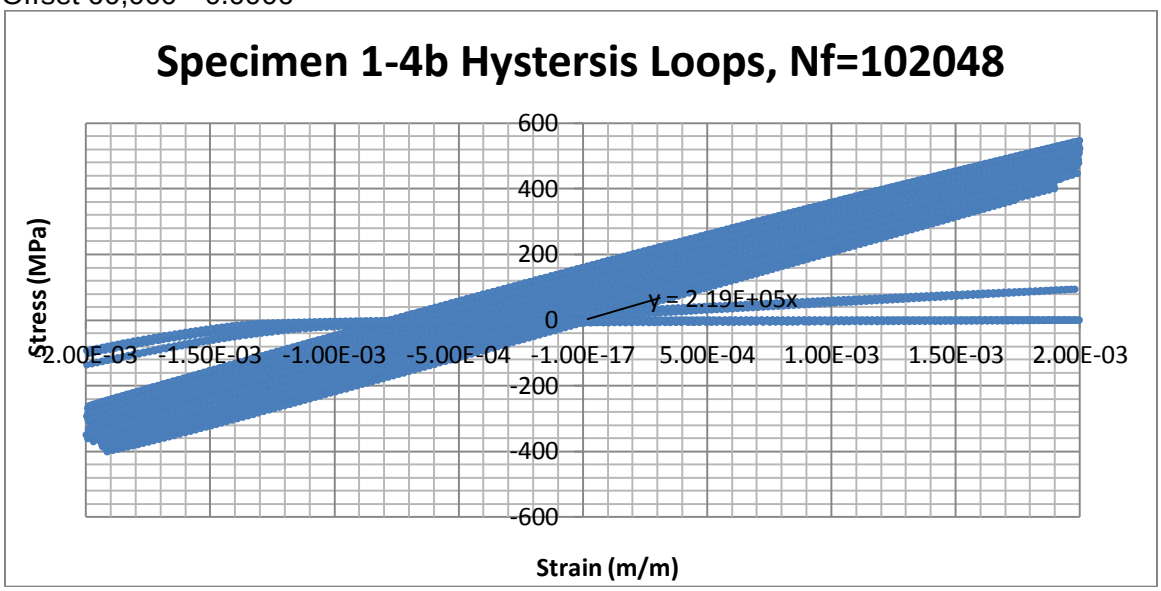

Young's Modulus per Cycle

Cycle No.	Compression Cycle (MPa)	Tension Cycle (MPa)
4	2.14E+05	2.18E+05
9	2.15E+05	2.20E+05
19	2.14E+05	2.20E+05
39	2.13E+05	2.19E+05
59	2.14E+05	2.18E+05
79	2.15E+05	2.19E+05
99	2.13E+05	2.19E+05
399	2.13E+05	2.17E+05
699	2.13E+05	2.18E+05
999	2.12E+05	2.18E+05
3999	2.10E+05	2.16E+05
6999	2.11E+05	2.17E+05
9999	2.09E+05	2.16E+05
19999	2.10E+05	2.13E+05
39999	2.07E+05	2.16E+05
59999	2.07E+05	2.17E+05

Max Stress per Cycle

Cycle No.	Max (MPa)	Min (MPa)	Mean Stress (MPa)	Alt. Stress (MPa)
1	403	-402	403	1
2	407	-395	401	6
3	409	-388	399	11
4	416	-388	402	14
5	424	-386	405	19
6	428	-381	404	23
7	433	-380	406	26
8	436	-378	407	29
9	440	-378	409	31
19	458	-371	415	43
29	467	-364	416	52
39	472	-362	417	55
49	478	-356	417	61
59	480	-354	417	63
69	482	-352	417	65
79	483	-351	417	66

Appendix B – Half Life Data

Half Life Data – HR590						
Specimen ID	**Half Life Cycle**	**E Modulus (MPa)**	**Strain**	**Stress (MPa)**	**Plastic Strain**	**Elastic Strain**
7-1b	59	137000	0.0200	631	0.0165	0.0046
7-2b	49	154000	0.0187	661	0.0150	0.0043
6-1b	89	148000	0.0168	645	0.0134	0.0044
6-2b	89	161000	0.0166	653	0.0132	0.0041
5-1b	99	164000	0.0139	630	0.0106	0.0038
5-2b	199	135000	0.0139	556	0.0110	0.0041
5-3b	99	159000	0.0139	636	0.0106	0.0040
5-4b	89	163000	0.0138	638	0.0105	0.0039
4-1b	199	170000	0.0109	610	0.0078	0.0036
4-2b	199	162000	0.0110	602	0.0080	0.0037
4-3b	199	158000	0.0109	597	0.0077	0.0038
3-1b	599	168000	0.0079	565	0.0051	0.0034
3-2b	499	174000	0.0079	579	0.0050	0.0033
2-1b	1999	162000	0.0050	513	0.0023	0.0032
2-2b	1999	178000	0.0050	510	0.0025	0.0029
1_5-2b	4999	179000	0.0035	507	0.0011	0.0028
1_5-3b	4999	185000	0.0034	515	0.0009	0.0028
1_3-1b	9999	193000	0.0029	489	0.0006	0.0025
1_1-1b	29999	202000	0.0023	424	0.0003	0.0021
1-1b	69999	204000	0.0020	369	0.0002	0.0018
1-4b	49999	196000	0.0020	520	0.0000	0.0027

Half Life Data – HR590DP						
Specimen ID	**Half Life Cycle**	**E Modulus (MPa)**	**Strain**	**Stress (MPa)**	**Plastic Strain**	**Elastic Strain**
7-2a	59	127000	0.0196	593	0.0166	0.0047
7-3a	59	127000	0.0198	591	0.0167	0.0047
6-1a	99	133000	0.0169	562	0.0140	0.0042
6-2a	79	151000	0.0169	572	0.0140	0.0038
5-1a	199	145000	0.0139	547	0.0112	0.0038
5-2a	199	143000	0.0139	533	0.0113	0.0037
4-2a	399	153000	0.0109	510	0.0084	0.0033
3-1a	899	163000	0.0079	497	0.0057	0.0030
3-2a	699	165000	0.0079	491	0.0055	0.0030
2-1a	1999	175000	0.0049	420	0.0029	0.0024
2-3a	2999	185000	0.0049	433	0.0030	0.0023
1_5-1a	7999	170000	0.0035	367	0.0017	0.0022
1_5-2a	6999	171000	0.0035	364	0.0018	0.0021
1_1-1a	19999	181000	0.0023	343	0.0014	0.0019
1_1-2a	19999	186000	0.0023	291	0.0007	0.0016
1-3a	89999	183000	0.0020	303	0.0010	0.0017
1-5a	79999	178000	0.0020	323	0.0005	0.0018

Appendix C - Definitions

Mean Stress Amplitude

$$\boldsymbol{\sigma_{mean} = \frac{\sigma_{max} - \sigma_{min}}{2}}$$

Alternating Stress

$$\boldsymbol{\sigma_{alt} = \frac{\sigma_{max} + \sigma_{min}}{2}}$$

Elastic Strain Component

$$\boldsymbol{\varepsilon_{elastic} = \frac{\sigma}{E}}$$

Plastic Strain Component

$$\boldsymbol{\varepsilon_{plastic} = \varepsilon_{total} - \varepsilon_{elastic}}$$

References

1. Senuma, T. Physical Metallurgy of Modern High-Strength Steels. *ISIJ International* **2001,** *41* (6), 520-532.

2. Landgraf, R. W.; Thangjitham, S.; Ridder, R. L. Automotive Wheel Assembly: A Case Study in Durability Design. In *ASTM STP1250: Case Studies for Fatigue Education;* Stephens, R. I., Ed.; American Society for Testing Materials: Philadelphia, 1994; pp 5-22.

3. Bhat, S. P. Influence of Composition Within A Grade On the Fatigue Properties of HSLA Steels. Philadelphia, 1983; pp 579-591.

4. Pickering, F. B. The Spectrum of Microalloyed High Strength Low Alloy Steels. *HSLA Steels: Technology and Applications*, Philadelphia, 1983; pp 1-31.

5. Sherman, A. M. Fatigue Properties of High Strength-Low Alloy Steels. *Metallurgical Transactions A* **1975,** *6A,* 1035-1040.

6. Gladman, T. *The Physical Metallurgy of Microalloyed Steels;* The Institute of Materials: London, 1997.

7. Jamwal, R. S. *Microstructural Origins of Variability in the Tensile Ductility of Dual Phase Steels;* Georgia Intitute of Technology: Atlanta, 2011.

8. Krauss, G. Solidification, Segregation, and Banding in Carbon and Alloy Steels. *Metallurgical and Materials Transactions* **2003,** *34B,* 781.

9. Khalid, F. A.; Farooque, M.; ul Haq, A.; Khan, A. Q. Role of ferrite/pearlite banded structure and segregation on mechanical properties of microalloyed hot rolled steel. *Materials Science and Technology* **1999,** *15,* 1209.

10. Davis, C. L.; Strangwood, M. Segregation behaviour in Nb microalloyed steels. *Materials Science and Technology* **2009,** *25* (9), 1126-1133.

11. Landgraf, R. W. Fatigue Resistance and Microstructure of Ferrous Alloys. In *ASM Handbook,* 10th ed.; American Society of Materials: Materials Park, 1996; Vol. 19, pp 605-613.

12. Porter, D. A.; Easterling, K. E.; Sherif, M. Y. Solidification of Ingots and Castings. In *Phase Transformations in Metals and Alloys,* 3rd ed.; CRC Press: Boca Raton, 2009; pp 230-239.

13. Salehi, A. R.; Serajzadeh, S.; Karmi Taheri, A. A Study on the Microstructural Changes in Hot Rolling of Dual Phase Steels. *Journal of Material Science* **2006,** *41,* 1917-1925.

14. Leis, B. Effect of Surface Condition and Processing on Fatigue Performance. In *ASM*

Handbook; Lampman, S., Ed.; ASM: Materials Park, 1996; Vol. 19, pp 314-320.

15. Sprock, A.; Peretic, M. J.; Speer, J. G. Compact Cooling as an Alternative to Alloying for Production of DP/TRIP Steel Grades. *Iron and Steel Technology,* August 2010, 170-177.

16. Sarwar, M.; Priestner, R.; Ahmad, E. Influence of Martensite Volume Fraction on Fatigue Limit of Dual Phase Steel. *Journal of Materials Engineering and Performance* **2002,** *11* (3), 274-277.

17. Capdevila, C.; Garcia-Mateo, C.; Chao, J.; Caballero, F. G. Advanced vandium alloyed steel for heavy product applications. *Materials Science and Technology* **2009,** *25* (11), 1383-1386.

18. Gupta, C.; Nagchaudhury, J.; Chakravartty, J. K.; Prasad, R. C. Cyclic stress-strain characteristics of two microalloyed steels. *Materials Science and Technology* **2009,** *25* (6), 760-769.

19. Zhongguang, W.; Guonan, W.; Wei, K.; Haicai, H. Influence of the Martensite Content on the Fatigue Behaviour of a Dual-phase Steel. *Materials Science and Engineering* **1987,** *91,* 39-44.

20. Tayanc, M.; Aytac, A.; Bayram, A. The Effect of Carbon Content on Fatigue Strength of Dual Phase Steels. **2007,** *28,* 1827-1835.

21. Sun, S.; Pugh, M. Properties of thermomechanically processes dual-phase steels containing fibrous martensite. *Materials Science and Engineering* **2002,** *A335,* 298-308.

22. American Society for Testing Materials. *Manual on Low Cycle Fatigue Testing, ASTM STP 465;* Philadelphia, PA, 1969.

23. Shigley, J. E.; Mischke, C. R.; Budynas, R. G. *Mechanical Engineering Design;* McGraw Hill: New York, 2004.

24. Mitchell, M. R. Fundamentals of Modern Fatigue Analysis for Design. In *ASM Handbook;* ASM International: Materials Park, OH, 1996; Vol. 19, pp 227-249.

25. Sherman, A. M.; Davies, R. G. Fatigue of Dual Phase Steel. *Metallurgical Transactions A* **1979,** *10A,* 929-933.

26. Radhakrishnan, V. M. On the bilinearity of the Coffin-Manson low cycle fatigue relationship. *International Journal of Fatigue* **1992,** *14* (5), 305-311.

27. Sinha, A. K. *Ferrous Physical Metallurgy;* Butterworth: Boston, 1989.

28. Standard Practice for Strain Controlled Fatigue Testing. *ASTM E 606-04* **2004**.

29. Standard Test Methods and Definitions for Mechanical Testing of Steel Products.

ASTM A370-10 **2010**.

30. Little, R. E.; Jebe, E. H. Manual of Statistical Planning and Analysis for Fatigue Experiments. *ASTM STP 588* **1975**.

31. Wilson, A. D. Fracture and Fatigue Properties of Structural Steels. In *ASM Handbook,* 10th ed.; ASM: Materials Park, 1996; Vol. 19, pp 591-604.

32. Ma, J.; Zhang, B.; Daokui, X.; Han, E.; Ke, W. Effects of inclusion and loading direction on the fatigue behavior of hot rolled low carbon steel. *International Jounal of Fatigue* **2010,** *32,* 1116-1125.

33. Meyers, M. A.; Chawla, K. K. Solid Solution, Preciptation, and Dispersion Hardening. In *Mechanical Behavior of Materials,* 2nd ed.; Cambridge University Press, 2009; pp 558-591.

34. Manual on Low Cycle Fatigue Testing. *ASTM STP 465* **1969**.

35. Bhat, S. P. Prediction of the Thickness Reductions from Fatigue Properties of High Strength Steels. *SAE International Congress and Exposition*, Detroit, 1984.

36. Mediratta, S. R.; Ramaswamy, V.; Rao, P. R. Influence of ferrite-martensite microstructural morphology on the low cycle fatigue of a dual phase steel. *International Journal of Fatigue* **1985,** *7* (2), 107-115.

37. Bayram, A.; Uguz, A.; Murat, U. Effects of Microstructure and Notches on the Mechanical Properties of Dual-Phase Steels. *Materials Characterization* **1999,** *43,* 259-269.

38. Standard Practice for Statistical Analysis of Linear or Linearized Stress-Life (S-N) and Strain-Life (ε-N) Fatigue Data. *ASTM E739-10* **2010**.

39. Joenoes, A. T. *Quantitative Analysis of Fatigue Behavior, Fatigue Damage and Fatigue Fracture Surfaces of Low Carbon Bainitic Steel (SAE 15B13);* Dissertation; Georgia Institute of Technology: Atlanta, 1996.

40. Bhat, S. P.; Cline, R. S.; Chung, Y. Fatigue Crack Initiation in Iron and a High-Strength Low-Alloy Steel. *Morris E. Fine Symposium*, Detroit, 1990; pp 49-61.

41. Korchynsky, M. HSLA Steels Technology & Applications. Philadelphia, 1984.

42. Snoek, J. L. Effect of Small Quantites of Carbon and Nitrogen on the Elastic and Plastic Properties of Iron. *Physica* **1941,** *8,* 711-733.

43. Dowling, N. E. *Mechanical Behavior of Materials;* Prentice Hall: Upper Saddle River, 1998.

44. Matlock, D. K.; Krauss, G.; Speer, J. G. New Microalloyed Steel Applications for the Automotive Sector. *Materials Science Forum* **2005,** *500-501,* 87-96.

45. Speer, J. G.; Matlock, D. K. Recent Developments in Low-Carbon Sheet Steels. *Journal of Materials* **2002,** 19-24.

46. Sarwar, M.; Ahmad, E.; Hussain, N.; Ahmad, B.; Manzoor, T. Crack Path Morphology in Dual Phase Steel. *Journal of Materials Engineering and Performance* **2006,** *15* (3), 352-354.

47. Sarwar, M.; Priestner, R. Fatigue Crack Propagation Behavior in Dual-Phase Steel. *Journal of Materials Engineering and Performance* **1999,** *8* (2), 245-251.

48. Sudhakar, K. V.; Dwarakadasa, E. S. A study on fatigue crack growth in dual phase martensitic steel in an air environment. *Bulletin of Material Science* **2000,** *23* (3), 193-199.

49. Hilditch, T. B.; Timokhina, I. L.; Robertson, L. T.; Pereloma, E. V.; Hodgson, P. D. Cyclic Deformation of Advanced High-Strength Steels: Mechanical Behavior and Microstructural Analysis. *Metallurgical and Materials Transactions* **2009,** *40A,* 342-353.

50. Bhadeshia, H. K. D. H.; Honeycombe, R. W. K. *Steel Microstructure and Properties,* 3rd ed.; Elsevier Ltd.: Oxford, 2006.

51. Marder, A. R. The Structure-Property Relationships in Chromium-Bearing Dual-Phase Steels. *Fundamentals of Dual-Phase Steels*, Chicago, 1981; pp 145-160.

52. Atkinson, H. V.; Shi, G. Characterization of inclusions in clean steels: a review including the statistics of extremes methods. *Progress in Materials Science* **2003,** *48,* 457-520.

53. Hu, Z. G.; Zhu, P.; Meng, J. Fatigue Properties of Transformation-Induced Plasticity and Dual-Phase Steels for Auto-Body Lightweight: Experiment, Modeling and Appliction. *Materials and Design* **2010,** *31,* 2884-2890.

54. Fredriksson, K.; Melander, A.; Hedman, M. Influence of prestraining and ageing on fatigue properties of high-strength sheets steels. *International Journal of Fatigue* **1988,** *10* (3), 139-151.

55. Gustavsson, A.; Melander, A. Fatigue of a Highly Prestrained Dual-Phase Sheet Steel. *Fatigue & Fracture of Engineering Materials & Structures* **1995,** *18* (2), 201-210.

56. Landgraf, R. W.; Thangjitham, S.; Ridder, R. L. Automotive Wheel Assembly: A Case Study in Durability Design. In *ASTM STP 1250: Case Studies for Fatigue Education;* Stephens, R. L., Ed.; American Society for Testing Materials: Philadelphia, 1994; pp 5-22.

57. Alzari, S.; Moriconi, J.; Brandaleze, E.; Chiapporoli, W.; Mansilla, G.; Herenu, S. Practical Fatigue Resistance Assesment of Microalloyed High Strength and Dual Phase Steels. *16th IAS Rolling Conference*, San Nicolas, 2006; pp 683-692.

58. Azari, Z.; Abbadi, M.; Moustabchir, H.; Lebienvenu, M. The influence of fatigue cycling on the oxidation kinetics and crack initiation of a Cr-Mo steel. *International Journal of Fatigue* **2008,** *30,* 517-527.